Barrier Properties of Polymer Nanocomposites with Graphene Oxide and Its Derivatives: Mechanism and Applications in Anticorrosive Coatings

Yidan Guan
University of Southern Mississippi

BARRIER PROPERTIES OF POLYMER NANOCOMPOSITES WITH GRAPHENE

OXIDE AND ITS DERIVATIVES: MECHANISM AND APPLICATIONS IN

ANTICORROSIVE COATINGS

by

Yidan Guan

A Dissertation
Submitted to the Graduate School,
the College of Science and Technology,
and the School of Polymers and High Performance Materials
at The University of Southern Mississippi
in Partial Fulfillment of the Requirements
for the Degree of Doctor of Philosophy

December 2017

BARRIER PROPERTIES OF POLYMER NANOCOMPOSITES WITH GRAPHENE

OXIDE AND ITS DERIVATIVES: MECHANISM AND APPLICATIONS IN

ANTICORROSIVE COATINGS

by Yidan Guan

December 2017

Approved by:

_____
Dr. Derek L. Patton, Committee Co-Chair
Associate Professor, Polymers and High Performance Materials

_____
Dr. James W. Rawlins, Committee Co-Chair
Associate Professor, Polymers and High Performance Materials

_____
Dr. Robert Y. Lochhead, Committee Member
Professor Emeritus, Polymers and High Performance Materials

_____
Dr. Robson F. Storey, Committee Member
Professor, Polymers and High Performance Materials

_____
Dr. Sarah E. Morgan, Committee Member
Professor, Polymers and High Performance Materials

_____
Dr. Jeffrey S. Wiggins
Director, School of Polymers and High Performance Materials

_____
Dr. Karen S. Coats
Dean of the Graduate School

Published by the Graduate School

ABSTRACT

BARRIER PROPERTIES OF POLYMER NANOCOMPOSITES WITH GRAPHENE

OXIDE AND ITS DERIVATIVES: MECHANISM AND APPLICATIONS IN

ANTICORROSIVE COATINGS

by Yidan Guan

December 2017

Metallic devices made from steel or aluminum are subjected to deterioration by

environmental contaminants over time. As one of the corrosion control methods, organic

coatings show many advantages due to their low cost, versatility, decoration aesthetics

and effective protections. Corrosion protection theories and failure modes of organic

coatings are still not fully understood due to complicated interactions in the coating-

metal-environment system, however, it is widely agreed that the barrier nature of

polymeric materials towards aggressive species, such as oxygen, water, electrolyte, plays

a key role. Improved barrier property of polymer nanocomposites (PNCs) with two-

dimensional (2D) carbon filler, graphene and graphene oxide (GO), has been extensively

studied in the areas of membrane science and packaging materials, however, a systematic

study on their applications as protective coatings is still rare.

In this work, we describe the fabrication and modification of PNCs containing

GO and GO derivatives in an effort to formulate organic coatings with improved barrier

properties and corrosion resistance. Impacts of GO and GO derivatives upon oxygen

permeability and water resistance of their PNCs were studied and correlated to their

corrosion protection properties. In the first study, functionalized GO containing reduced

hydrophilic moieties were synthesized by the reaction between hydroxyl group (–OH) on

GO and α-bromoisobutyrl bromide, with the intent of reducing water sensitivity while maintaining high oxygen barrier property of the resulting latex nanocomposites fabricated via aqueous blending with styrene-acrylic copolymer latex. The second study focused on the development of a facile efficient protocol for synthesizing GO derivatives by using a designed low-density aerogel precursor, which exhibits improved reactivity in many organic solvents with low polarity. Hydrophobically modified GO was prepared using small-molecule (hexanoyl chloride) and oligomeric (amino terminated) polyisobutylene (PIB) modifier(s), and thoroughly investigated for their surface properties. In the third study, a bilayer coating of waterborne epoxy-amine resin based composites was designed to provide improved water and oxygen barrier properties by incorporating GO lamellae in the bottom layer and hydrophobic polymer additive in the top layer. The resultant bilayer coating exhibits improved corrosion protection performance in simulated corrosive environments due to reduced surface wettability and decreased oxygen permeability.

ACKNOWLEDGMENTS

Ohio State University, the Air Force Academy, The University of Akron, The University of Southern Mississippi, the Air Force Institute of Technology, the Naval Postgraduate School, and the US Naval Academy.

DEDICATION

This dissertation is dedicated to my beloved parents Mr. Shuyuan Guan and Mrs.

Qilan Liang, and my husband Yongwu Lu, for their love, encouragement, and support.

TABLE OF CONTENTS

LIST OF TABLES

LIST OF FIGURES

xvi

xvii

LIST OF ABBREVIATIONS

α	Aspect Ratio
η	Overvoltage
ω	Frequency
ϕ	Volume Fraction
$aq.$	Aqueous
2D	Two-Dimensional
ΔG	Gibbs Free Energy
AFM	Atomic Force Microscopy
ATR	Attenuated Total Reflectance
C	Capacitor
CNT	Carbon Nanotube
CPE	Constant Phase Element
CPVC	Critical Pigment Volume Concentration
CRS	Cold Rolled Steel
CV	Cyclic Voltammetry
CVD	Chemical Vapor Deposition
D	Diffusivity
DI	Deionized
DL	Double Layer
DMA	Dynamic Mechanical Analysis
DSC	Differential Scanning Calorimetry
DVS	Dynamic Vapor Sorption

E	Potential
E'	Storage Modulus
E''	Loss Modulus
E_{eq}	Equilibrium Potential
E_{ox}	Oxidation Potential
$Eq.$	Equation
E_{red}	Reduction Potential
E_{rev}	Reversible Potential
EEW	Equivalent Epoxy Weight
EIS	Electrochemical Impedance Spectroscopy
eV	Electron Volts
F	Faraday Constant
f_b	Breakpoint Frequency
Fe^{2+}	Ferrous Cation
$FTIR$	Fourier Transform Infrared
G'	Shear Storage Modulus
G''	Shear Loss Modulus
GO	Graphene Oxide
Gr	Graphene
H_2O	Water
i	Current Density
I	Current
J_∞	Steady-State Transmission Rate

LDGOAero	Low Density Graphene Oxide Aerogel
LNCs	Latex Nanocomposites
MB	Methylene Blue
mGO	Modified Graphene Oxide
MFFT	Minimum Film Formation Temperature
MMT	Montmorillonite
NaCl	Sodium Chloride
O_2	Oxygen
OCP	Open Circuit Potential
OH^-	Hydroxide Anion
$-OH$	Hydroxyl Group
P	Permeability
PNCs	Polymer Nanocomposites
R	Resistance
r*GO*	Reduced Graphene Oxide
RH	Relative Humidity
RT	Room Temperature
S	Solubility
SEM	Scanning Electron Microscopy
SHE	Standard Hydrogen Electrode
SPU	Standard Permeability Unit
TEM	Transmission Electron Microscopy
T_g	Glass Transition Temperature

TGA	Thermogravmetry Analysis
PE	Polyethylene
PIB	Polyisobutylene
UV-vis	Ultraviolet-visible
VOC	Volatile Organic Compound
WBEP	Waterborne Epoxy
WCA	Water Contact Angle
|Z|	Total Impedance Magnitude
Z_{re}	Real Impedance
Z_{im}	Imaginary Impedance

CHAPTER I – BACKGROUND

1.1 Motivations

Modern societies have been heavily depending on the use of metallic devices and metal structure for bridges, buildings, aircrafts, ships, automobiles, and gas pipelines. Corrosion, the environmental degradation of metal by physicochemical interactions, can induce the failures of these facilities, leading to property damages and risk of lives.[1] Billions of dollars are spent each year on maintenances and replacements to prevent global corrosion-related damages.[2] Organic coating has been one of the most cost-effective and widely used methods for metal protection in the past decades.[3] Coating formulations can be very complicated, but in general they consist of organic binders, pigments, solvents or diluents, and various additives.[4-5] Two major functions provided by organic coatings are decoration and protection: the decoration aspect is achieved by using pigments and stains that can hide the original appearance of substrate, while the protection capability depends on mechanical, barrier and adhesion properties.[6]

For corrosion protection coatings, barrier property towards aggressive species from environment, such as oxygen, water, and electrolytes, is crucial.[3, 6] In addition, mechanical properties, such as film formation, adhesion, flexibility, and weatherability, also play important roles in the long-term protection applications.[3, 7] In order to develop coatings with desirable properties for metal protection in various environmental conditions, i.e. the humid coast areas and the cold Arctic[3, 6-7], a thorough understanding of the interactions among all coating components is of great importance.

Graphene oxide (GO), a two-dimensional (2D) carbon allotrope with an atomic thickness, has attracted much attention in the past decade due to outstanding mechanical

properties and functionalization capabilities.[8-10] Polymer nanocomposites (PNCs) with

GO and its derivatives exhibit significant improvement on their barrier properties,

indicating their potential applications as high-performance protective coatings.[11-13]

This chapter begins with a brief overview of corrosion mechanism and evaluation

methods, followed with discussions on the corrosion control mechanisms of anticorrosive

coatings and the barrier/permeation aspect of polymeric materials. Current research on

PNCs and anticorrosive coatings with novel materials will also be reviewed.

1.2 Mechanism of Metal Corrosion

1.2.1 Categories of Corrosive Environments

Corrosion is defined as the degrading process of a metal due to physiochemical

interactions with its environment; therefore, corrosion resistance of a material varies with

given metal-environment system.[14] The environments for corrosion to occur are classified

into categories so that aggressiveness can be compared, and accordingly the proper

corrosion control method or anticorrosive coating can be selected.[7] ISO 12944 suggested

three categories for outdoor environmental exposure, namely immersion, atmospheric,

and splash zone with subgroups (Figure 1.1).[15]

Immersion refers to the situation when metallic structures or anticorrosive

coatings are immersed in water or buried in soil. There are three subgroups in immersion,

including soil, fresh water, and sea water. However, the overall corrosivity is specific and

difficult to be determined due to the combined effects of temperature, salinity, bacteria,

pH, electrolytes, and dissolved gas, especially, O_2 in the systems.[7] In general, fresh water

is much less aggressive than sea water because of lower dissolved salts content,

especially sodium chloride which is very aggressive towards many metals and coatings.

2
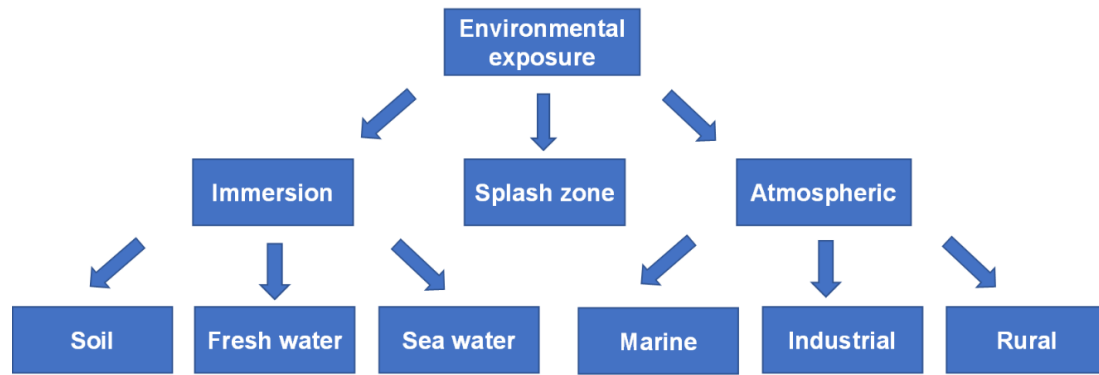
Figure 1.1 Classification of corrosion environment for anticorrosive coatings (Reference 15)

The atmospheric environment is subjected to alternating conditions caused by radiation, heat, relative humidity, as well as salt and gas concentrations.[7] Typical corrosive conditions can be evaluated by studying climate, level of pollution, and distance to sea. A rural area far from the sea exhibits much lower corrosivity in comparison to marine or industrial atmosphere with corrosion-aggressive polluting gases (i.e., HCl, SO_2, NH_3), and particulates such as dust, dirt, and soot.[6] The splash zone exposure refers to the structures that are situated near the waterline of sea, such as the parts of an offshore plants and the foundations of wind turbines. The combination of high O_2 content in air with continuous electrolytes splashing from sea makes it extremely aggressive; and therefore, both corrosion of metals and degradation of coatings in splash zone environment is significantly accelerated.[14, 16]

1.2.2 Thermodynamics of Corrosion

In most cases, corrosion stems from irreversible oxidation-reduction (redox) reaction between metal and oxidizing agent from environment.[14] For example, high-temperature corrosion of steel in air is due to redox reaction between iron and O_2, as shown in Eq. 1, that forms metal oxide. If corrosion occurs in acidic environment, proton

3

(hydrogen cation) is reducing agent and hydrogen gas will be generated by corrosion (Eq. 2).

$$4Fe(s) + 3O_2 \rightarrow 2Fe_2O_3 \qquad (1)$$

$$Fe(s) + 2H^+(aq) \rightarrow Fe^{2+}(aq) + H_2(g) \qquad (2)$$
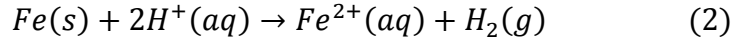
However, chemical reactions in real world corrosion are more complicated, because they are affected by other corrosive compounds such as water and electrolytes (ions), and microbial conditions.[7] For example, atmospheric corrosion of steel in humid air can be described by Eq. 3.

$$4Fe(s) + 3O_2(g) + 2H_2O(l) \rightarrow 4FeOOH(s) \qquad (3)$$
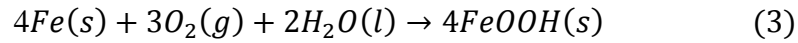
Corrosion proceeds slowly if one of these elements is eliminated or restricted to be at lower concentration, such as dry air in desert and deoxygenated water.
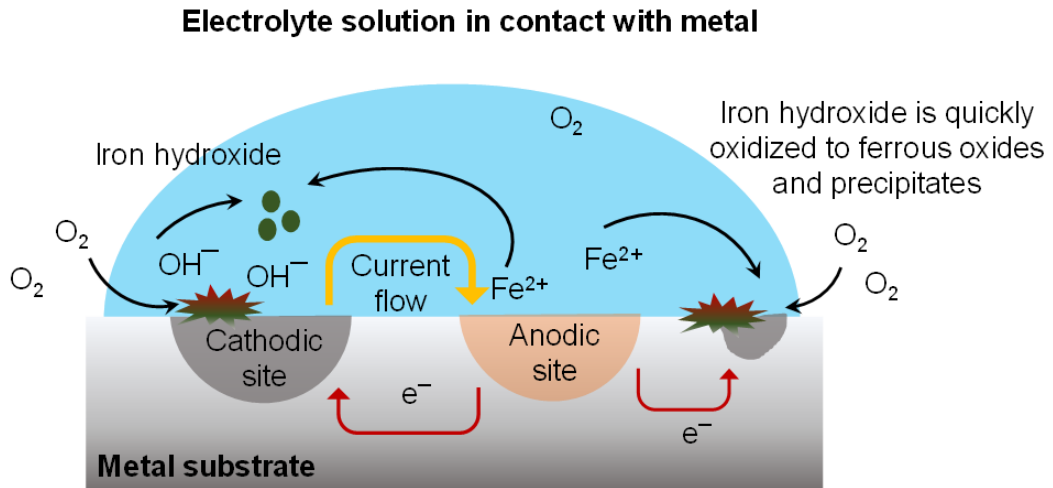
Figure 1.2 Corrosion cell process of steel in the presence of water, O_2 and electrolytes (Reference 7).

A chemical battery that converts energy from redox reaction to electrical work is known as electrochemical cell, where two pieces of metal are connected by a conductive

wire and submerged into electrolyte solution.[14] Aqueous corrosion (Figure 1.2) is

compared to a "dead-shorted" battery that turns energy from redox corrosion reaction into

heat irreversibly, and thus regarded as electrochemical corrosion cell. Two partial

reactions in redox reaction are also called half-cell reactions: partial oxidation reaction is

known as anodic reaction; and partial reduction reaction is considered as cathodic

reaction.[14] The current pathway in corrosion cell is fulfilled by a charge carrier, usually

ions from dissolved electrolytes.

$$2H_2O(l) + O_2(g) + 4e^- \rightarrow 4OH^-(aq) \tag{4}$$

$$Fe(s) \rightarrow Fe^{2+}(aq) + 2e^- \tag{5}$$

$$6Fe(OH)_2(s) + O_2(g) \rightarrow 4H_2O(l) + 2FeO \cdot Fe_2O_3 \cdot H_2O(s) \tag{6}$$

$$FeO \cdot Fe_2O_3 \cdot H_2O(s) \rightarrow FeO \cdot Fe_2O_3(s) + H_2O(l) \tag{7}$$

$$4FeO \cdot Fe_2O_3(s) + O_2(g) + 6H_2O(l) \rightarrow 6Fe_2O_3 \cdot H_2O(s) \tag{8}$$

$$12Fe(s) + 9O_2(g) + 6H_2O(l) \rightarrow 6Fe_2O_3 \cdot H_2O(s) \tag{9}$$
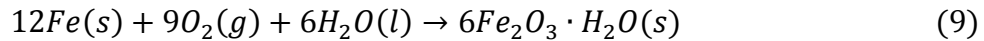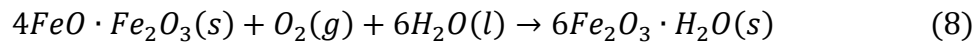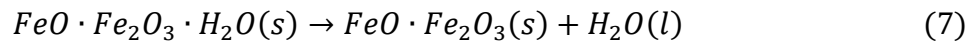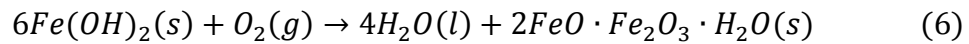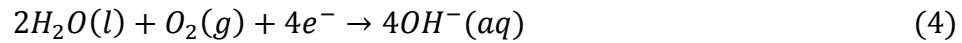
When steel is submerged in water with dissolved salts (i.e., NaCl), some areas on

surface become anodic sites while some others become cathodic sites.[14] On cathodic site,

dissolved O_2 is reduced to hydroxide anions (OH^-) as shown in Eq. 4, but intermediate

products such as peroxides, superoxides, and radicals can also be generated.[17-19] On

anodic site, electrons are given out (as shown in Eq. 5) to supply the reactions on

cathodic sites with the formation of ferrous cations (Fe^{2+}). Fe^{2+} will first react with OH^-

from cathodic reaction to form iron hydroxide, but the latter will quickly be oxidized into

ferrous oxides, a green hydrated magnetite with the following formulation:

FeO•Fe2O3•H2O (Eq. 6).[17] The unstable hydrated magnetite will then decompose into

relatively stable black magnetite FeO•Fe2O3 (Eq. 7).[7] However, with excess oxygen in the

system, black magnetite will subsequently be oxidized into dark-red hydrated hematite $Fe_2O_3 \bullet H_2O$ that is more stable, and known as rust.[17] The overall reaction for rust formation can be rewritten into Eq. (9).

$$\Delta G = \sum v_i \mu_i = -n \cdot F \cdot E_{rev} \tag{10}$$

$$E_{rev} = E_{ox} + E_{red} \tag{11}$$

A decrease of Gibbs free energy ($\triangle$G) is expected for a spontaneous reaction such as the reaction between active metal (i.e., iron) and oxygen.[14] $\triangle$G of this redox reaction can be represented by reversible potential of equilibrium potential (E_{rev} or E_{eq}) of electrochemical cell as shown in Eq. 10. F is Faraday constant, which is 96485 C/mol; and n is the number of charge transferred in the electrodes reaction.[14] The equilibrium potential is determined by the difference between half-cell reactions on each electrode in standard potentials, namely E_{ox} and E_{red}, respectively. For example, the equilibrium potential for iron corrosion in neutral water can be calculated by using half-cell potentials from Eq. 4 and 5, which are +0.401 V (vs standard hydrogen electrode (SHE)) and +0.447 V (vs SHE), respectively.[7] Gibbs free energy can be calculated subsequently to be negative, indicating that the reaction will occur spontaneously if reaction rate is sufficient. In some cases, thermodynamically favored corrosion may occur at a very low rate in given environment conditions, such as the corrosion of aluminum in neutral aqueous solution with a robust protection layer of Al_2O_3 on its surface.[7]

1.2.3 Electrochemical Corrosion and Kinetics

Corrosion rate can be determined by gravimetrical or electrochemical testing in various immersion conditions in the lab.[3, 14] Although the weight loss of metallic samples

can be directly measured, the presence of corrosion products and coatings on the substrates may render the measurement complicated. In an electrochemical test, corrosion current is generated by data fitting and related to mass loss via Faraday's Law (Eq. 12). Q is the charge from the reaction; n is the number of electrons transferred per molecule or atom; F is Faraday's constant, 96485 C/mol; and M is the number of moles of the reacting species.

$$Q = n \cdot F \cdot M \qquad (12)$$

To elucidate the control parameters of corrosion rate, a thorough understanding of the fundamentals of corrosion kinetics is required. There are three basic theories for corrosion kinetics: activation controlled kinetics, mixed potential theory, and mass transport effects.[20] The activation controlled kinetics is the most fundamental theory that is used when mass transport is sufficiently fast and the rate is controlled by charge transfer reaction.[20] When corrosion occurs in immersion, the resulting potential of metal electrode (E) is different from reversible potentials (E_{rev}) of each of half-cell reactions. If the concentration of reactants and products at the electrode surface is the same as in the bulk, this potential difference is called activation overvoltage (or charge transfer overvoltage), η. In this case, the relationship between the rate of reaction (expressed by current density, i) and the driving force (overvoltage, η) obeys the Butler-Volmer equation:

$$i = i_0 \cdot \exp\left[\frac{\alpha \cdot n \cdot F \cdot \eta}{RT}\right] - i_0 \cdot \exp\left[\frac{-(1 - \alpha) \cdot n \cdot F \cdot \eta}{RT}\right] \qquad (13)$$

$$i_{net} = i_0 \cdot \exp\left[\frac{\alpha \cdot n \cdot F \cdot \eta_a}{RT}\right] \qquad (14)$$

$$\eta_a = \beta_a \cdot \log \left(i / i_0 \right) \tag{15}$$

$$\eta_c = -\beta_c \cdot \log \left(|i| / i_0 \right) \tag{16}$$

where R is gas constant 8.314 J/(mol·K), and α is the unitless charge transfer coefficient, which is usually close to 0.5 and between 0~1. At a large overvoltage condition ($\eta_a > \sim 50$ mV), Eq. 13 can be approximated to Eq. 14. By rearranging Eq. 14, the Tafel equation (Eq. 15) can be obtained, where β_a is the anodic Tafel slope (Figure 1.3a). A similar equation (Eq. 16) can be obtained for cathodic activation polarization. In most cases (when mass transport is not important), the corrosion conditions are far from its equilibrium potentials, thereby Tafel plots can accurately describe the corrosion kinetics and be used to calculate the corrosion rate of coated and uncoated metal substrates.[14, 20]
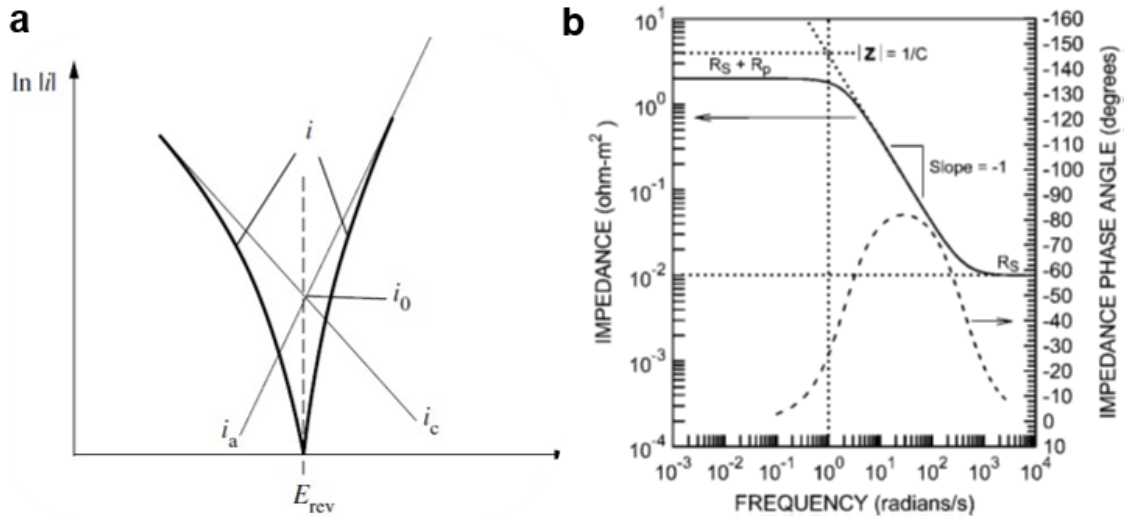
Figure 1.3 (a) Tafel plot and (b) Bode magnitude and phase plots (Reference 14).

1.2.4 Methods of Corrosion Resistance Evaluation

In addition to corrosion rate measurement, electrochemical impedance spectroscopy (EIS) is also an useful tool for analyzing coating resistance and evaluating barrier property towards water/electrolyte solution.[14, 21-22] EIS data is obtained by

8

measuring the impedance response on an electrode (coated or uncoated metal substrate) that is subjected to a small sinusoidal perturbation of voltage at changing frequencies.[14, 23-25] The modulus of impedance and phase angle is recorded as a function of sweep frequency, respectively, known as Bode modulus and Bode phase plots (Figure 1.3b). EIS data can also be plotted in x-y coordinates using real (x) and imaginary (y) part of total impedance, named as Nyquist plot. Furthermore, equivalent circuit model can be assigned to simulate experimental data by mimicking the system with electrical elements, which can represent resistance/capacitance behavior in organic coatings, and charge/mass transfer phenomenon at the metal/liquid interface.

Although the ultimate test is by coating's performance in normal service environment, natural exposure is time consuming and non-comparable. Therefore, simulated or accelerated corrosion environments are used to evaluate the results based on the determined coating failure data.[3] Anticorrosive coatings are preliminarily apprised by continuous spray of salt water according to (modified) ASTM B1 17 testing standard in humidity exposure chamber.[3-4, 7] Although it is not entirely satisfactory and quantitative, this method offers quick and visual estimation of coating performance.[3]

1.3 Barrier Aspect of Anticorrosive Coatings

1.3.1 Corrosion Control Mechanisms

In general, corrosion of metals can be controlled by three strategies: isolation of metal from environment (barrier effect), suppression of anodic metal dissolution by cathodic (galvanic) protection, and concealing of the corresponding cathodic reaction.[7, 14] The schematic diagram of organic coating system on metal substrate is shown in Figure 1.4. In metallic coatings, for example, active metals such as zinc are applied within a thin

film on steel substrate to perform as a sacrificial anode, which prevents iron from dissolution.[26] However, for zinc-rich organic primer coating, a major part of effectiveness is believed to be the formation of zinc oxide compounds in the initial stage of cathodic protection, which block the pores and passivate the surface.[3, 27]
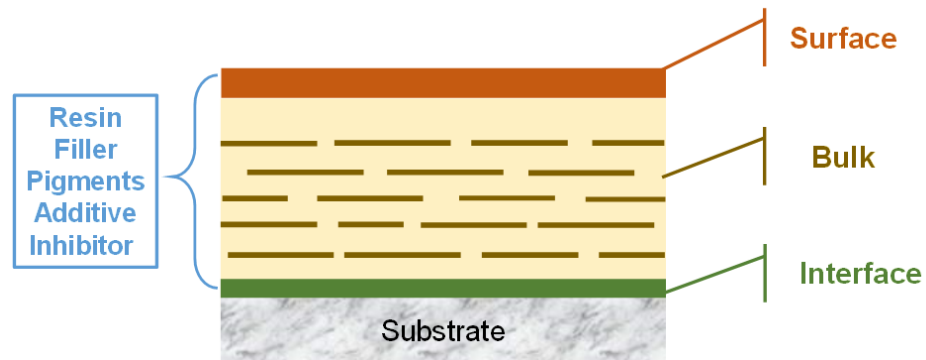
Figure 1.4 Schematic diagram of organic coating system on metal substrate.

A primer that contains inhibitor can also effectively protect metal surface by passivation due to chemical reactions.[28] The inhibitors need to be partially dissolved by moisture absorbed in coating during exposure and carried to metal surface, so that the active ionic species can react with metal to form a layer of noble compounds.[29] If the concentration of inhibitors is not high enough for sufficient leaching, problems such as blistering will occur.[7] Because some inhibitor packages contain toxic ingredients (i.e. chromates), this type of coating is mainly used for metallic devices subjected to atmospheric corrosion, especially industrial environments, and it is not recommended for immersion in water or burial in soil.[16, 29]

Barrier effects of organic coatings depend on hindered mass transport of corrosive species due to lower permeability of polymeric materials to liquids, gases, and ions.[6, 30] Many theories have been developed with regard to the role that barrier function plays in corrosion protection mechanism.[3, 6] A few of earlier studies suggested that elimination of

H_2O and O_2 was the main reason for corrosion decreasing.[3] However, some later studies indicated neither H_2O nor O_2 was the rate determining factor, and corrosion protection was attributed to electrical resistance and ion impermeability of organic coatings.[3] To varying extents, disagreement upon the later theory also existed, where O_2 permeation was believed to be the controlling factor of corrosion, and H_2O permeation was only the rate-determining step for adhesion loss.[3]

Barrier function presents in primers, intermediates and topcoats, which are commonly applied on immersed metallic structural and devices.[7] Permeability of organic coatings is influenced not only by polymer properties, but also the presence of pigments and fillers and their interactions with polymer matrix.[3] Inert pigments such as titanium dioxide (TiO_2), micaceous iron oxide (Fe_2O_3), lamellar clays, glass flakes, carbon black, and graphite are usually incorporated in organic coatings at a volume concentration that is below the critical pigment volume concentration (CPVC) for enhanced barrier properties.[28, 31] Under such a low concentration (below CPVC), coating matrices are densified by pigments so that the penetration of aggressive species can be reduced.[32]

Various failure modes were developed for analyzing barrier coatings, such as cathodic delamination, anodic undermining, mechanical disbondment by osmotic force and so on.[3, 23, 33-38] However, those theories are still under debate, and the actual mechanisms are not yet fully understood. The intrinsic coating properties, coating thickness, and the application protocols are all considered to have an impact on the overall protection capability.[7, 39-40] Besides, small defects such as micropores and microcracks that inevitably existed in coatings will serve as the penetration pathway of corrosive species and induce microscopic coating delamination in corrosive

11

environments.[7] To save cost from labor and materials, thinner and lighter coatings with sufficient barrier properties are desired in advanced coating formulations.

1.3.2 Barrier/Permeability of Polymeric Materials
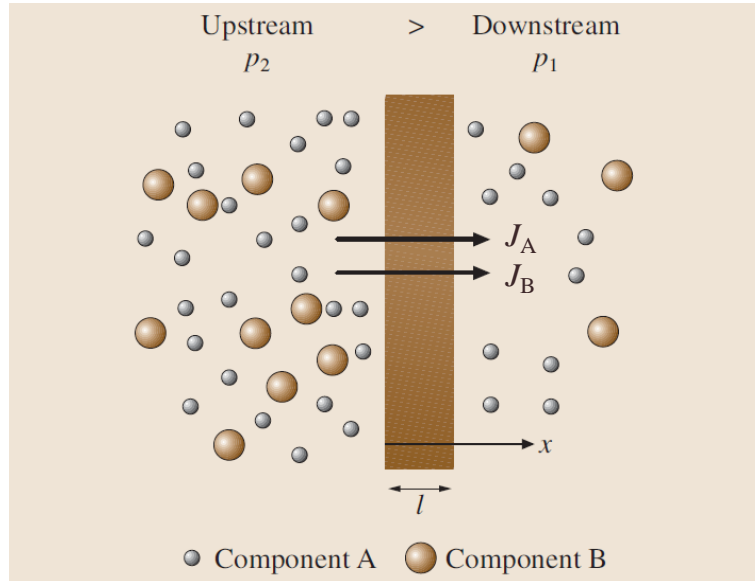
Figure 1.5 Transport of gases A and B across a membrane (Reference 41).

Many theories have been developed to explain the phenomenon of permeation of small molecules (e.g., O_2) through dense or non-porous polymeric membrane.[6, 41-42] The solution-diffusion mechanism is used to describe the process of gas transport through such a film.[41, 43] In this model (Figure 1.5) three steps are required: (1) sorption of the penetrant molecules in the upstream side of the film; (2) diffusion of molecules through the film due to a concentration gradient; and finally (3) desorption of molecules from the downstream side of the film. Fick's Law can be used to describe a one-dimensional flux of gas A through a film in the x-direction (i.e. JA):

$$J_A = -D\frac{dC_A}{dx} + w_A(J_A + J_P) \tag{17}$$

where D is diffusion coefficient, C_A is local concentration of dissolved gas, w_A is weight fraction of gas A in the film, and J_P is the flux of membrane (usually taken to be zero).[41] The permeability of gas A (P_A) through a film, mathematically defined as the product of solubility (S) and diffusivity (D) coefficients, can be calculated by using Eq. 19 from the steady-state transmission rate (J_∞) that is experimentally measured for gas A, with known film thickness (l) and partial pressure difference across the film.[41] The standard unit (SPU) for permeability is commonly expressed in terms of Barrers (1 Barrer = 10^{-10} (cm^3) cm cm^{-2} s^{-1} $cmHg^{-1}$).[41]

$$P = S \times D \tag{18}$$

$$P_A = \frac{J_\infty \times l}{p_2 - p_1} \tag{19}$$

Solubility is thermodynamically controlled while diffusivity is kinetically controlled in the process of permeation.[41, 43] Simple models that typically used for gas sorption in polymers are Henry's law, Flory-Huggins theory, and dual-mode sorption model.[41] The free volume theory for gas diffusion describes a cooperative movement of permeant molecule and polymer segments from one hole to another that is created by fluctuation of local density of segments.[41] Permeability depends on many factors, such as the size and shape of penetrant and its interactions with given polymer, intrinsic free volume, glass transition temperature and crosslink density of polymer, as well as the testing conditions.[6, 41]
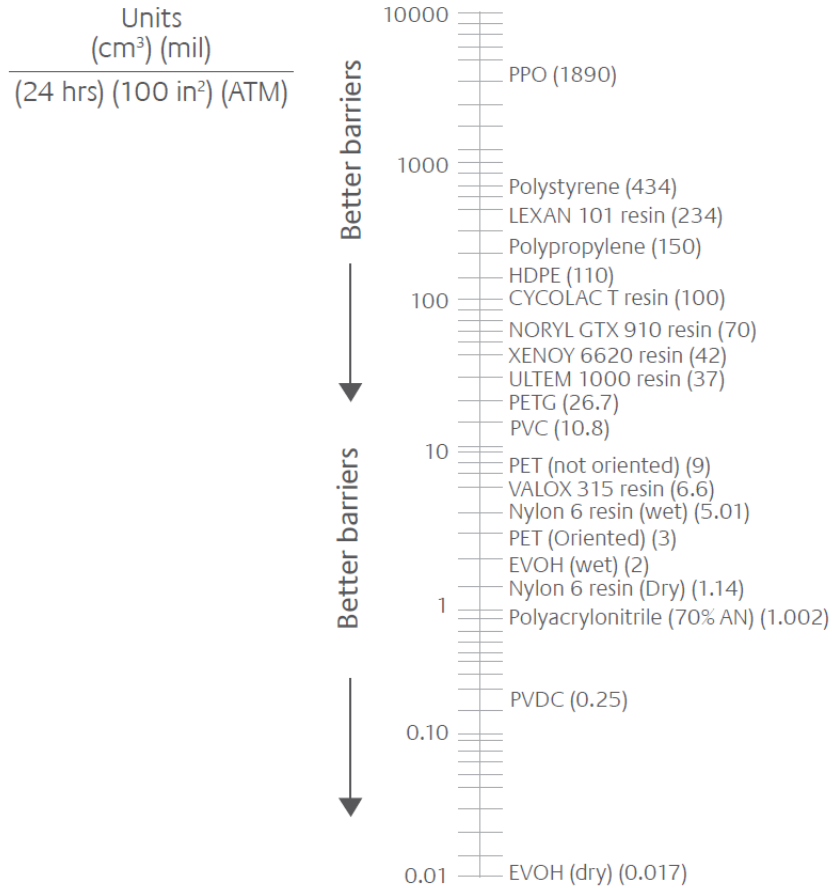
Figure 1.6 O_2 permeability measured on representative polymeric materials at 25°C. (Reference 44).

Oxygen, as an inert molecule to polymeric materials, exhibits minimal sorption that neither swelling strain nor chain rearrangement will be expected in the solid structure.[6] Therefore, oxygen partial pressure has no impact on its solubility, diffusivity, and permeation coefficient at any given temperature. Permeation of O_2 is governed only by intrinsic properties of polymer matrix, including polarity, unsaturation, symmetry, lateral chains, steric hindrance, crosslinking, hydrogen bonding, intermolecular forces, co-monomers present, crystallinity, glass transition temperature, and orientation.[6] Figure 1.6 shows a summary of O_2 permeability coefficient of common commercial polymers obtained at 25°C (by *SABIC*).[44] On the contrary, the permeation of active gases (i.e. CO_2)

14

largely depends on solubility, which is due to strong interactions between penetrants and matrix.[6]

Units
$$\frac{(g)\ (mil)}{(24\ hrs)\ (100\ in^2)}$$

Better Barriers

100
90
80
70
60
50 — Silicone Elastoner (53.1)

40
30 — NORYL GTX™ 910 (31.5) resin

20 — Nylon 6 resin (19)
— LEXAN™ 101 resin (14)
— General purpose CYCOLAC™ resin (12)
10 — Polystyrene resin (10)

9
8 — ULTEM™ 1000 resin (7.9)
7 — XENOY™ 6620 resin (7.2)
6
5

4 — Polyacrylonitrile (70% AN) (3.8)
3

2 — PVC (2)
— VALOX 315 resin (1.3)
1 — PET resin (1.2)
.9
.8
.7
.6
.5
.4 — HDPE (0.35)
.3 — Polypropylene (0.3)
.2
.1

Better Barriers

Figure 1.7 H_2O permeability measured on representative polymeric materials at 37.8⁰F with 90% relative humidity (Reference 44).

Permeability of H_2O in polymeric materials has been intensively studied for applications such as food packaging, drug delivering, membrane technology, protective coatings, and electronics.[45-50] The permeation process of H_2O is more complicated due to several reasons such as high polarity of molecule, strong interactions with certain polymers, hydrogen-bonding ability, induced swelling, and chain mobility.[6] Moreover, physical state of H_2O (vapor and liquid) shows impacts on permeability property due to different kinetic energy of molecules.[6] Water vapor molecules in constant motion exhibit

15

an average velocity of about 450 m/s, while liquid water only has very small kinetic energy.[6] Additionally, this varying property is also caused by capillaries effect, where permeation of liquid H_2O is restricted but H_2O vapor transmission is not affected.[6]

Solubility plays a dominating role in the transmission of H_2O (liquid and gas) in polymers. However, there is no direct relationship between the amount of permeated water and absorbed water. Coatings that absorb more water should not necessarily allow more water vapor to permeate through.[6] Sorption of water in polymers has been described by Henry's law, Flory-Huggins theory, and occasionally a multilayer mode depending on the circumstances.[6, 41] Permeation is a rate process, which is governed by temperature and concentration gradient across film due to diffusion of penetrant. Diffusivity of H_2O in hydrophilic polymers usually increases with increasing water concentration, and permeability shows dependency on the absolute vapor pressure due to a proportional increase of solubility.[6] However, water diffusivity in hydrophobic polymers may vary inversely with increasing concentration due to the clustering phenomenon of water molecules.[6] Consequently, water transmission in coatings is complicated, which can be affected by vapor pressure difference across the film, solubility of H_2O in the film, thickness, area and physical conditions of film.[6]

Not all polymers are considered suitable binders for the design of barrier coatings. According to the model developed by Funke[51] for ranking orders of different coating systems tested by salt spray, three factors that controlled corrosion under high humidity are water permeability, oxygen permeability, and adhesion. Crystallinity and chain mobility (glass transition temperature, crosslink density) of polymers shows impacts on permeability.[3] However, those same factors that contribute to low permeability may

negatively affect adhesion property.[3] Consequently, good adhesion achieved due to the presence of polar functional groups also appears to be essential to increased water sensitivity (Figure 1.7).[44] Therefore, the balance between adhesion and water permeability in the coating formulation can be essential to achieve high resistance for corrosion. The impact on ionic impermeability by hydrophilic moieties in polymer network is not as important with sufficient high crosslink density.[6]

1.4 Graphene, Graphene Oxide, and Derivatives

1.4.1 Permeation in Polymer Nanocomposites
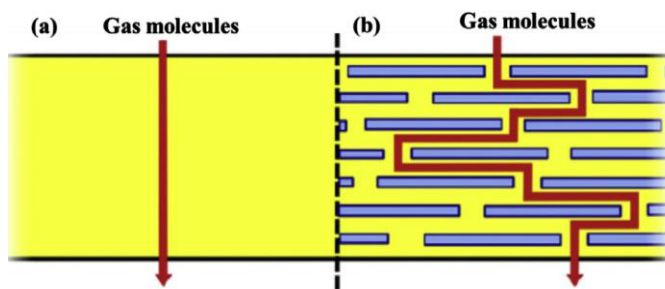
Figure 1.8 Schematic diagram of gas molecule diffuses (a) perpendicularly through compare with (b) a "tortuous pathway" created by nanoplatelets in a polymer matrix (Reference 52).

Nanomaterials such as carbon black, carbon nanotubes, clay, and graphene have been extensively studied as barrier fillers to decrease permeability of polymer matrix by tortuosity effect (Figure 1.8[52]).[11] Barrier property of polymer nanocomposites (PNCs) is governed by three factors: filler properties (resistance to penetrant diffusion, aspect ratio, and volume fraction), intrinsic barrier properties of polymer matrix, and the 'quality' of dispersion within polymer matrix (agglomeration/specific interface, free volume generated by mediocre interface management, and texture/orientation of filler sheets).[53] Therefore, the levels of exfoliation of layered nanofillers is crucial for successful fabrication of PNCs and their barrier properties. For example, organically modified

montmorillonite (MMT) exhibited increasing barrier enhancement within hydrophobic

polymers due to improved compatibility via intercalation of organic moieties, which

facilitate dispersion and exfoliation of clay platelets.[54]
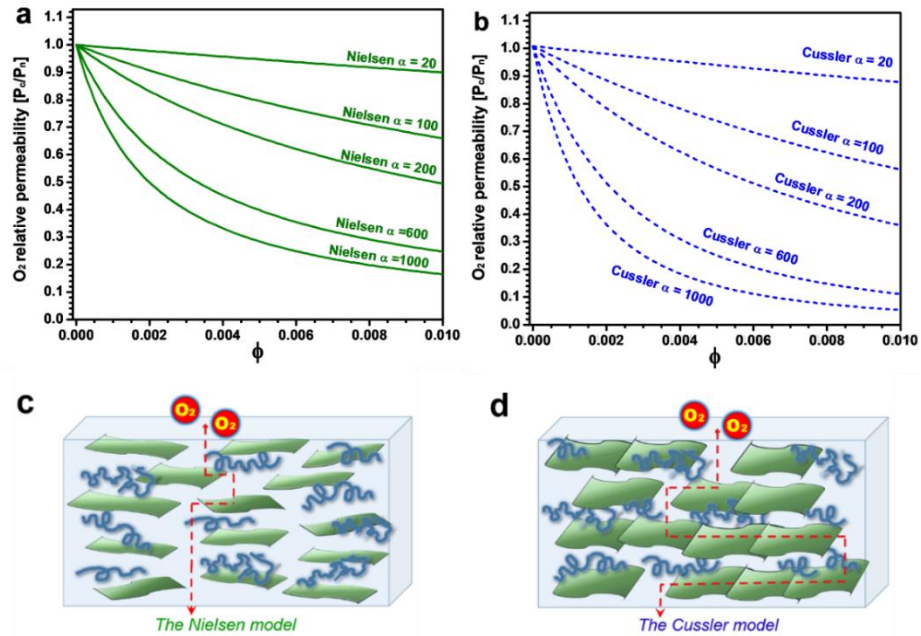
Figure 1.9 Predicted values and schematic representations of permeability of PNCs
according to the Nielsen (a, c) and Cussler (b, d) models.

Theoretical models have been developed for predicting gas permeability reduction

in PNCs containing lamellar fillers using two parameters: volume fraction (ϕ) and aspect

ratio (α).[11, 43] The theoretical relative permeability curves predicted by Nielsen and

Cussler models are plotted against volume fraction of filler at various aspect ratios,

respectively.[11] Despite these models assuming different diffusion and permeation

behaviors owing to a difference on the distance between lamellae, they both suggest that

relative permeability of PNCs decreases with increasing filler aspect ratio or volume

fraction. The Cussler model is more applicable in a system where lamellae are closely

arrayed throughout the matrix in a distance comparable to their latitudinal size, with

18

possible overlaps.[55] This is known as the semi-dilute conditions ($\phi \ll 1$, $\alpha\phi \gg 1$), where multiple scatterings of permeating molecules between close pairs of lamellar fillers lead to a significant decrease of the overall diffusivity of PNCs.[43]

1.4.2 Graphene, Graphene Oxide
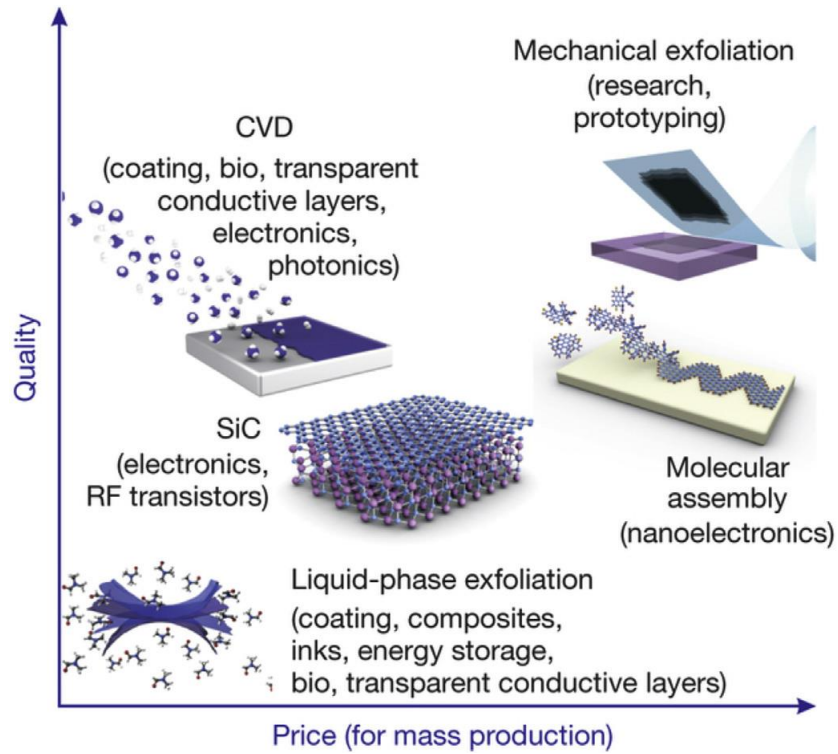
Figure 1.10 Schematic diagram for preparation and cost of graphene (Reference 56).

Graphene (Gr) attracted enormous attention due to its high electrical conductivity (6000 S cm^{-1}), thermal conductivity (~ 5000 W m^{-1} K^{-1}), and mechanical strength (Young's modulus ~ 1 TPa, and fracture strength 130 GPa) for PNC fabrications in the past decade.[56] As a monolayer platelet of sp^2–hybridized carbon atoms bonded in the hexagonal lattice, defect-free Gr sheet exhibited impermeability to helium molecules.[57] Crumpled Gr incorporated in PNCs displays high O_2 gas barrier enhancement similar to that of clay, but at ~ 25–130 times lower loadings.[43, 55] However, Gr platelets often suffer

from poor dispersing and weak interaction with polymer chains, thereby agglomerates and insufficient interfacial adhesion in PNCs significantly reduced its performance.[11]

Graphene oxide (GO) is a lamellar carbon allotrope and building block of Gr (reduced graphene oxide, rGO) with great potential for applications on gas separation, filtration membrane, thin-film electronics, and many others due to outstanding physiochemical properties.[10, 58-59] Owing to the enormous oxygenated functional groups on the basal and edge planes, GO exhibits sufficient processing compatibility in polar solvents and polymers.[11, 60-61] Moreover, these reactive moieties also serve as chemical groups for covalent (or noncovalent) modifications that allows for extended properties.[8]

1.4.3 Recent Study on Anticorrosive Coatings with GO (Derivatives)

Recently, numerous studies on the anticorrosive application of GO and GO derivatives have been reported on various metal substrates.[62-64] Prasai and coworkers[65] reported that a few nanometers of Gr layers obtained by chemical vapor deposition (CVD) on copper or nickel substrates could reduce corrosion rates by 7-20 times. Prabakar and coworkers[12] found that GO could effectively suppress the oxidation of aluminum current collector in lithium ion battery. Chang and coworkers[66] prepared composite coatings with polyaniline/graphene incorporated that exhibited improved anticorrosive performance. Sun and coworkers[67] synthesized a Gr derivative by encapsulating reduced GO with 3-aminopropyl triethoxysilane to depress the corrosion-promotion activity of conductive Gr that leads to galvanic corrosion. Ramezanzadeh and coworkers[68], Yu and coworkers[69] investigated the anticorrosive performance of GO and GO derivatives incorporated in epoxy coatings, respectively. Qi and coworkers[70] also reported polymer-grafted GO nanocomposite coating's anticorrosive performance on

steel substrate. Those studies showed that, with sufficient amount of GO (derivatives) incorporated in polymeric coatings, improved barrier property can be achieved, which leads to improved and long-term corrosion protection.
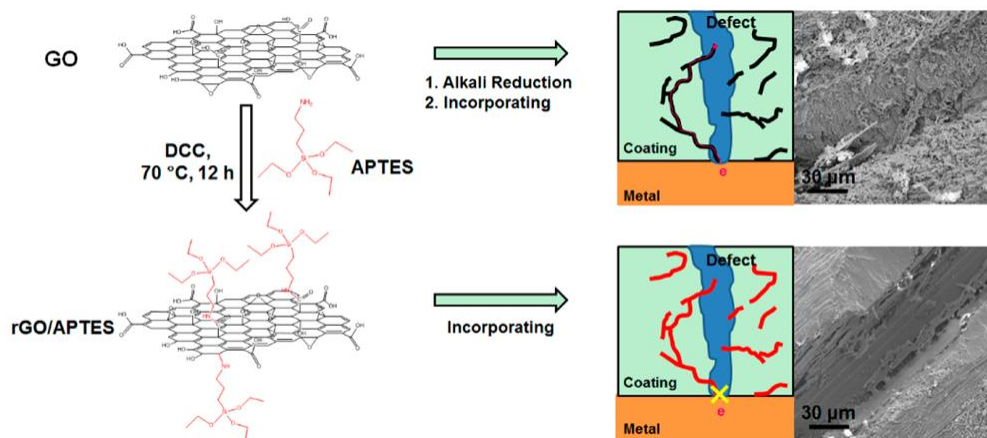
Figure 1.11 Barrier effect of GO derivatives in anticorrosive nanocomposite coatings (Reference 67).

1.5 Summary of Background

In summary, incorporation of Gr, GO (derivatives) in corrosion protection coatings has proved successful on achieving enhanced barrier property, which holds enormous potential for high-performance, cost-effective anticorrosive coating applications. On the other hand, the ultimate design of GO (derivatives) by covalent functionalization remains unsolved and the corrosion control mechanism of PNCs is still unclear. A thorough investigation of the structural-property relationship is desired to illuminate corrosion resistance with regards to barrier effects, and to extend their wider applications in PNCs for protective coatings and many others.

1.6 References

1.   Li, X.; Zhang, D.; Liu, Z.; Li, Z.; Du, C.; Dong, C., Materials science: Share corrosion data. *Nature* **2015,** *527* (7579), 441-2.

2.   Koch, G. H.; Research, U. S. F. H. A. O. o. I.; Development; Laboratories, C. T.; Center, T.-F. H. R.; International, N., *Corrosion cost and preventive strategies in the United States*. Turner-Fairbank Highway Research Center: 2002.

3.   Dickie, R. A.; Floyd, F. L., Polymeric Materials for Corrosion Control: An Overview. In *Polymeric Materials for Corrosion Control*, American Chemical Society: 1986; Vol. 322, pp 1-16.

4.   Schoff, C. K., Organic coatings: the paradoxical materials. *Progress in Organic Coatings* **2005,** *52* (1), 21-27.

5.   Wicks, Z. W., *Organic coatings : science and technology*. 3rd ed ed.; Wiley-Interscience: Hoboken, N.J., 2007; p xxiii, 722 p.

6.   Sangaj, N. S.; Malshe, V. C., Permeability of polymers in protective organic coatings. *Progress in Organic Coatings* **2004,** *50* (1), 28-39.

7.   Sørensen, P. A.; Kiil, S.; Dam-Johansen, K.; Weinell, C. E., Anticorrosive coatings: a review. *Journal of Coatings Technology and Research* **2009,** *6* (2), 135-176.

8.   Gao, W., The Chemistry of Graphene Oxide. In *Graphene Oxide: Reduction Recipes, Spectroscopy, and Applications*, Gao, W., Ed. Springer International Publishing: Cham, 2015; pp 61-95.

9.   Yang, Y.-H.; Bolling, L.; Priolo, M. A.; Grunlan, J. C., Super Gas Barrier and Selectivity of Graphene Oxide-Polymer Multilayer Thin Films. *Advanced Materials* **2013,** *25* (4), 503-508.

10.   Georgakilas, V.; Otyepka, M.; Bourlinos, A. B.; Chandra, V.; Kim, N.; Kemp, K. C.; Hobza, P.; Zboril, R.; Kim, K. S., Functionalization of Graphene: Covalent and Non-Covalent Approaches, Derivatives and Applications. *Chemical Reviews* **2012,** *112* (11), 6156-6214.

11.   Cui, Y.; Kundalwal, S. I.; Kumar, S., Gas barrier performance of graphene/polymer nanocomposites. *Carbon* **2016,** *98*, 313-333.

12.   Richard Prabakar, S. J.; Hwang, Y.-H.; Bae, E. G.; Lee, D. K.; Pyo, M., Graphene oxide as a corrosion inhibitor for the aluminum current collector in lithium ion batteries. *Carbon* **2013,** *52*, 128-136.

13.   Yu, Z.; Lv, L.; Ma, Y.; Di, H.; He, Y., Covalent modification of graphene oxide by metronidazole for reinforced anti-corrosion properties of epoxy coatings. *RSC Advances* **2016,** *6* (22), 18217-18226.

14.   Landolt, D., *Corrosion and Surface Chemistry of Metals*. EFPL Press: 2007.

15.   ISO 12944.

16.   Armelin, E.; Oliver, R.; Liesa, F.; Iribarren, J. I.; Estrany, F.; Alemán, C., Marine paint fomulations: Conducting polymers as anticorrosive additives. *Progress in Organic Coatings* **2007,** *59* (1), 46-52.

17.   Watson, T. M.; Coleman, A. J.; Williams, G.; McMurray, H. N., The effect of oxygen partial pressure on the filiform corrosion of organic coated iron. *Corrosion Science* **2014,** *89*, 46-58.

18.   Wroblowa, H. S.; Qaderi, S. B., Mechanism and kinetics of oxygen reduction on steel. *Journal of Electroanalytical Chemistry and Interfacial Electrochemistry* **1990,** *279* (1), 231-242.

19.   Wroblowa, H. S., Intermediate products of atmospheric oxygen reduction and the integrity of metal—organic coating interface. *Journal of Electroanalytical Chemistry* **1992,** *339* (1), 31-40.

20.   Frankel, G. S., Fundamentals of Corrosion Kinetics. In *Active Protective Coatings: New-Generation Coatings for Metals*, Hughes, A. E.; Mol, J. M. C.; Zheludkevich, M. L.; Buchheit, R. G., Eds. Springer Netherlands: Dordrecht, 2016; pp 17-32.

21.   Murray, J. N., Electrochemical test methods for evaluating organic coatings on metals: an update. Part I. Introduction and generalities regarding electrochemical testing of organic coatings. *Progress in Organic Coatings* **1997,** *30* (4), 225-233.

22.   Walter, G. W., The application of impedance spectroscopy to study the uptake of sodium chloride solution in painted metals. *Corrosion Science* **1991,** *32* (10), 1041-1058.

23.   van Westing, E. P. M.; Ferrari, G. M.; Geenen, F. M.; de Wit, J. H. W., In situ determination of the loss of adhesion of barrier epoxy coatings using electrochemical impedance spectroscopy. *Progress in Organic Coatings* **1993,** *23* (1), 89-103.

24.   Rammelt, U.; Reinhard, G., Characterization of active pigments in damage of organic coatings on steel by means of electrochemical impedance spectroscopy. *Progress in Organic Coatings* **1994,** *24* (1), 309-322.

25.   Bonora, P. L.; Deflorian, F.; Fedrizzi, L., Electrochemical impedance spectroscopy as a tool for investigating underpaint corrosion. *Electrochimica Acta* **1996,** *41* (7), 1073-1082.

26.   Prosek, T.; Nazarov, A.; Thierry, D., Role of steel and zinc coating thickness in cut edge corrosion of coil coated materials in atmospheric weathering conditions; Part 2: Field data and model. *Progress in Organic Coatings* **2016,** *101*, 45-50.

27.   Zhang, L.; Ma, A.; Jiang, J.; Song, D.; Chen, J.; Yang, D., Anti-corrosion performance of waterborne Zn-rich coating with modified silicon-based vehicle and lamellar Zn (Al) pigments. *Progress in Natural Science: Materials International* **2012,** *22* (4), 326-333.

28.   Brooman, E. W., Modifying organic coatings to provide corrosion resistance: Part II—Inorganic additives and inhibitors. *Metal Finishing* **2002,** *100* (5), 42-53.

29.   Brooman, E. W., Corrosion performance off environmentally acceptable alternatives to cadmium and chromium coatings: Chromium—Part I. *Metal Finishing* **2000,** *98* (7), 38-43.

30.   Liu, X.; Xiong, J.; Lv, Y.; Zuo, Y., Study on corrosion electrochemical behavior of several different coating systems by EIS. *Progress in Organic Coatings* **2009,** *64* (4), 497-503.

31.   Brooman, E. W., Modifying organic coatings to provide corrosion resistance—Part I: Background and general principles. *Metal Finishing* **2002,** *100* (1), 48-53.

32.   Perera, D. Y., Effect of pigmentation on organic coating characteristics. *Progress in Organic Coatings* **2004,** *50* (4), 247-262.

33.   Scantlebury, D., The dynamic nature of underfilm corrosion. *Corrosion Science* **1993,** *35* (5), 1363-1366.

34.   Negele, O.; Funke, W., Internal stress and wet adhesion of organic coatings. *Progress in Organic Coatings* **1996,** *28* (4), 285-289.

35.   Funke, W., Problems and progress in organic coatings science and technology. *Progress in Organic Coatings* **1997,** *31* (1), 5-9.

36.   Leng, A.; Streckel, H.; Hofmann, K.; Stratmann, M., The delamination of polymeric coatings from steel Part 3: Effect of the oxygen partial pressure on the delamination reaction and current distribution at the metal/polymer interface. *Corrosion Science* **1998,** *41* (3), 599-620.

37.   Leng, A.; Streckel, H.; Stratmann, M., The delamination of polymeric coatings from steel. Part 2: First stage of delamination, effect of type and concentration of cations on delamination, chemical analysis of the interface. *Corrosion Science* **1998,** *41* (3), 579-597.

38.   Williams, G.; McMurray, H. N., The kinetics of chloride-induced filiform corrosion on aluminum alloy AA2024-T3. *J Electrochem Soc* **2003,** *150* (8), B380-B388.

39.   Sørensen, P. A.; Kiil, S.; Dam-Johansen, K.; Weinell, C. E., Influence of substrate topography on cathodic delamination of anticorrosive coatings. *Progress in Organic Coatings* **2009,** *64* (2), 142-149.

40.   Aksakal, B.; Gavgali, M.; Dikici, B., The Effect of Coating Thickness on Corrosion Resistance of Hydroxyapatite Coated Ti6Al4V and 316L SS Implants. *J Mater Eng Perform* **2010,** *19* (6), 894-899.

41.   Czichos, H.; Saito, T.; Smith, L. R., *Springer handbook of materials measurement methods*. Springer: Germany, 2006; p xxvi, 1208 p.

42.   Bird, R. B.; Stewart, W. E.; Lightfoot, E. N., *Transport phenomena*. Rev. 2nd ed.; J. Wiley: New York, 2007; p xii, 905 p.

43.   Nazarenko, S.; Meneghetti, P.; Julmon, P.; Olson, B. G.; Qutubuddin, S., Gas barrier of polystyrene montmorillonite clay nanocomposites: Effect of mineral layer aggregation. *Journal of Polymer Science Part B: Polymer Physics* **2007,** *45* (13), 1733-1753.

44.   http://www.pod-sabic-ip.com/KBAM/Reflection/Assets/Thumbnail/10620_4.pdf.

45.   Liu, Y.; Soer, W.-J.; Scheerder, J.; Satgurunathan, G.; Keddie, J. L., Water Vapor Sorption and Diffusion in Secondary Dispersion Barrier Coatings: A Critical Comparison with Emulsion Polymers. *ACS Applied Materials & Interfaces* **2015,** *7* (22), 12147-12157.

46.   Zhou, J.; Lucas, J. P., Hygrothermal effects of epoxy resin. Part I: the nature of water in epoxy. *Polymer* **1999,** *40* (20), 5505-5512.

47.   Zanni-Deffarges, M. P.; Shanahan, M. E. R., Diffusion of water into an epoxy adhesive: comparison between bulk behaviour and adhesive joints. *International Journal of Adhesion and Adhesives* **1995,** *15* (3), 137-142.

48.   Liu, M.; Mao, X.; Zhu, H.; Lin, A.; Wang, D., Water and corrosion resistance of epoxy–acrylic–amine waterborne coatings: Effects of resin molecular weight, polar group and hydrophobic segment. *Corrosion Science* **2013,** *75*, 106-113.

49.   He, C.; Mighri, F.; Guiver, M. D.; Kaliaguine, S., Sorption of Water/Methanol on Teflon and Hydrocarbon Proton Exchange Membranes. *ACS Applied Materials & Interfaces* **2016,** *8* (19), 12541-12551.

50.   Hansen, C. M., Aspects of solubility, surfaces and diffusion in polymers. *Progress in Organic Coatings* **2004,** *51* (1), 55-66.

51.   Funke, W., How Organic Coating Systems Protect Against Corrosion. In *Polymeric Materials for Corrosion Control*, American Chemical Society: 1986; Vol. 322, pp 222-228.

52.   Duncan, T. V., Applications of nanotechnology in food packaging and food safety: Barrier materials, antimicrobials and sensors. *Journal of Colloid and Interface Science* **2011,** *363* (1), 1-24.

53.   Sinha Ray, S.; Okamoto, M., Polymer/layered silicate nanocomposites: a review from preparation to processing. *Progress in Polymer Science* **2003,** *28* (11), 1539-1641.

54.   Decker, J. J.; Meyers, K. P.; Paul, D. R.; Schiraldi, D. A.; Hiltner, A.; Nazarenko, S., Polyethylene-based nanocomposites containing organoclay: A new approach to enhance gas barrier via multilayer coextrusion and interdiffusion. *Polymer* **2015,** *61*, 42-54.

55.   Compton, O. C.; Kim, S.; Pierre, C.; Torkelson, J. M.; Nguyen, S. T., Crumpled Graphene Nanosheets as Highly Effective Barrier Property Enhancers. *Advanced Materials* **2010,** *22* (42), 4759-4763.

56.   Geim, A. K.; Novoselov, K. S., The rise of graphene. *Nat Mater* **2007,** *6* (3), 183-191.

57.   Bunch, J. S.; Verbridge, S. S.; Alden, J. S.; van der Zande, A. M.; Parpia, J. M.; Craighead, H. G.; McEuen, P. L., Impermeable Atomic Membranes from Graphene Sheets. *Nano Letters* **2008,** *8* (8), 2458-2462.

58.   Dreyer, D. R.; Park, S.; Bielawski, C. W.; Ruoff, R. S., The chemistry of graphene oxide. *Chemical Society Reviews* **2010,** *39* (1), 228-240.

59.   Marcano, D. C.; Kosynkin, D. V.; Berlin, J. M.; Sinitskii, A.; Sun, Z.; Slesarev, A.; Alemany, L. B.; Lu, W.; Tour, J. M., Improved Synthesis of Graphene Oxide. *ACS Nano* **2010,** *4* (8), 4806-4814.

60.   Paredes, J. I.; Villar-Rodil, S.; Martínez-Alonso, A.; Tascón, J. M. D., Graphene Oxide Dispersions in Organic Solvents. *Langmuir* **2008,** *24* (19), 10560-10564.

61.   Huang, H.-D.; Ren, P.-G.; Chen, J.; Zhang, W.-Q.; Ji, X.; Li, Z.-M., High barrier graphene oxide nanosheet/poly(vinyl alcohol) nanocomposite films. *Journal of Membrane Science* **2012,** *409*, 156-163.

62.   Nine, M. J.; Cole, M. A.; Tran, D. N. H.; Losic, D., Graphene: a multipurpose material for protective coatings. *Journal of Materials Chemistry A* **2015,** *3* (24), 12580-12602.

63.   Li, J.; Cui, J.; Yang, J.; Li, Y.; Qiu, H.; Yang, J., Reinforcement of graphene and its derivatives on the anticorrosive properties of waterborne polyurethane coatings. *Composites Science and Technology* **2016,** *129*, 30-37.

64.   Kang, D.; Kwon, J. Y.; Cho, H.; Sim, J.-H.; Hwang, H. S.; Kim, C. S.; Kim, Y. J.; Ruoff, R. S.; Shin, H. S., Oxidation Resistance of Iron and Copper Foils Coated with Reduced Graphene Oxide Multilayers. *ACS Nano* **2012,** *6* (9), 7763-7769.

65.   Prasai, D.; Tuberquia, J. C.; Harl, R. R.; Jennings, G. K.; Bolotin, K. I., Graphene: Corrosion-Inhibiting Coating. *ACS Nano* **2012,** *6* (2), 1102-1108.

66.   Chang, C.-H.; Huang, T.-C.; Peng, C.-W.; Yeh, T.-C.; Lu, H.-I.; Hung, W.-I.; Weng, C.-J.; Yang, T.-I.; Yeh, J.-M., Novel anticorrosion coatings prepared from polyaniline/graphene composites. *Carbon* **2012,** *50* (14), 5044-5051.

67.   Sun, W.; Wang, L.; Wu, T.; Wang, M.; Yang, Z.; Pan, Y.; Liu, G., Inhibiting the Corrosion-Promotion Activity of Graphene. *Chemistry of Materials* **2015,** *27* (7), 2367-2373.

68.   Bahlakeh, G.; Ramezanzadeh, B.; Saeb, M. R.; Terryn, H.; Ghaffari, M., Corrosion protection properties and interfacial adhesion mechanism of an epoxy/polyamide coating applied on the steel surface decorated with cerium oxide nanofilm: Complementary experimental, molecular dynamics (MD) and first principle quantum mechanics (QM) simulation methods. *Appl Surf Sci* **2017,** *419*, 650-669.

69.   Yu, Y.-H.; Lin, Y.-Y.; Lin, C.-H.; Chan, C.-C.; Huang, Y.-C., High-performance polystyrene/graphene-based nanocomposites with excellent anti-corrosion properties. *Polymer Chemistry* **2014,** *5* (2), 535-550.

70.   Qi, K.; Sun, Y.; Duan, H.; Guo, X., A corrosion-protective coating based on a solution-processable polymer-grafted graphene oxide nanocomposite. *Corrosion Science* **2015,** *98*, 500-506.

CHAPTER II – ECOFRIENDLY FABRICATION OF MODIFIED GRAPHENE

OXIDE LATEX NANOCOMPOSITES WITH HIGH OXYGEN BARRIER

PERFORMANCE

Large-scale industrial applications of barrier films and coatings that prevent permeation of degradative gases and moisture call for the development of cost-efficient and eco-friendly polymer nanocomposites. Herein, we report the facile fabrication of latex nanocomposites (LNCs) by incorporating surface-modified graphene oxide (mGO) at various loading (0.025–1.2 wt.%) into a styrene-acrylic latex using water as the processing solvent. LNCs fabricated with mGO exhibited significant reductions (up to 67%) in water vapor sorption resulting in greater environmental stability when compared to LNCs fabricated with equivalent loading of hydrophilic, unmodified GO. The assembly and coalescence of the exfoliated latex/mGO dispersions during the film formation process produced highly dispersed and well-ordered mGO domains with high aspect ratios, where alignment and overlap of the mGO domains improved with increasing mGO content. The addition of only 0.7 vol.% (1.2 wt.%) mGO led to an 84% decrease (relative to the neat polymer latex film) in oxygen permeability of the LNC films – an excellent barrier performance attributed to the observed LNC film morphologies. This work enables ecofriendly development of mechanically flexible mGO/LNC films with superior barrier properties for many industrial applications including protective coatings, food packaging and biomedical products.

2.1 Introduction

In modern society, high performance polymeric barrier materials have been widely used in a variety of applications owing to their light weight, low cost, easy

processing, and multifunctionality. The performance of barrier films, such as coatings applied for protecting different substrates, and plastic membranes used for storing food, drinks or medicine, is inherently limited by high permeability of penetrant species (e.g., oxygen, water/vapor and organic compounds).[1-2] Adding impermeable nanofillers, such as carbon black, carbon nanotubes, clay, and graphene,[3-6] is a common method to decrease the permeability of a polymer matrix. The barrier property of polymer nanocomposites (PNCs) is dominantly determined by three factors: filler properties (resistance to penetrant diffusion, aspect ratio, and volume fraction), the intrinsic barrier properties of the polymer matrix, and the 'quality' of dispersion within polymer matrix (agglomeration/specific interface, free volume generated by mediocre interface management, and the texture/orientation of filler sheets).[3, 7] The crux of successful development of PNCs is in league with the levels of exfoliation of the layered nanofillers in polymer matrix.[3, 5, 7] Clay, such as delaminated montmorillonite (MMT), is a widely used layered nanofiller for barrier applications of PNCs.[8-13] Organo-montmorillonite demonstrated improved compatibility with hydrophobic polymers via intercalation of the organic moieties, which favored nanoscale dispersion of inorganics into organic phases.[8-9, 12] However, the high face-to-face interaction stability in clays originating from van der Waals forces is still a problem that causes incomplete exfoliation, poor dispersion of clays within the polymer matrix, ultimately limiting the barrier performance of PNCs.[8-9, 12]

Graphene is a monolayer of sp^2–hybridized carbon atoms bonded in the hexagonal lattice that has a lamellar structure.[3, 5, 14] Because of its high electrical conductivity (6000 S cm^{-1}), thermal conductivity (~ 5000 W m^{-1} K^{-1}) and mechanical

strength (Young's modulus ~ 1 TPa, and fracture strength 130 GPa), graphene has gained paramount attention in PNCs for enhanced performances.[3, 5, 14] A defect-free graphene sheet was reported impermeable to helium gas molecules.[15] Crumpled graphene in PNCs[16] enabled gas barrier efficiency similar to clay, but at ~ 25–130 times lower loadings,[10] and one order of magnitude more effective than predicted by the modified-Nielsen[17] and Cussler[18] theories. However, graphene dispersion and its interaction with polymers are often poor, thereby leading to agglomerates and weak interfacial adhesion between graphene and polymer matrix.[3, 5] Graphene oxide (GO) is of eminent interest as an alternative form of atomic-thick carbon scaffold nanofillers in PNCs for improved physical properties.[3, 5, 19-22] GO is synthesized from graphite flakes via strong oxidation reaction (such as Staudenmaier's method, or Hummers' method) followed by physical exfoliation.[19, 23-26] GO has the desirable characteristics under various solvents processing condition ascribing from the oxygenated groups, e.g., hydroxyl and epoxy functionalities on the basal planes, and carbonyl and carboxylic acid moieties on the edge planes.[24] These polar groups also promote exfoliation and dispersion of GO nanosheets in polar solvents and polymer matrices, thus pronouncedly improving the interfacial adhesion between GO and polymer matrix.[3, 20, 24, 27-28] Recently, there has been an interest to employ GO-based nanoplatelets in place of the clay particulates as they potentially possess much higher aspect ratios, thus reducing the required filler loadings needed to achieve high gas barriers.[16, 20, 28] Most of these studies report using up to 1 vol% of graphene-based fillers to achieve considerable gas barrier reinforcement. Compton et al.[16] achieved a 50% reduction in oxygen permeability in polystyrene after adding 0.94 vol% phenyl isocyanate modified reduced graphene oxide (rGO). Huang et al.[20] reported a

45% oxygen permeability reduction in poly(lactic acid) after adding 1.4 vol% unmodified graphene oxide. Unalan *et al.*[28] achieved a 71% reduction of oxygen permeability in pullulan (biopolymer) after adding 1 vol% unmodified graphene oxide.

Legislative restrictions on volatile organic compound (VOC) emissions have driven the development of eco-friendly barrier films and waterborne coatings.[29-30] Latex-based coatings containing clays have been reported to improve barrier, thermal, and mechanical properties on leather, wood, and steel.[31-33] Latex nanocomposites (LNCs) containing rGO have been developed possessing high conductivity and low percolation threshold; properties that were attributed to uniform dispersion of rGO in the polymer matrix.[34] However, the large amount of surfactant required to facilitate rGO dispersion in the aqueous phase increased water sensitivity of the LNCs.[32] *In situ* reduction of GO/latex blending avoided the use of extra surfactant and enabled LNCs exhibiting high conductivity at low loadings; however, the use of toxic reducing agents (e.g., hydrazine hydrate) greatly limits *in situ* reduction for broad adoption in LNCs.[35-36] Hydrophilicity of fillers decreases compatibility and water resistance of the LNCs, while hydrophobicity sacrifices processability (for dispersion) in aqueous systems and causes agglomeration.[3, 32] The balance between hydrophilicity and hydrophobicity can be tuned by properly replacing the partial hydrophilic functional groups on GO.[3, 32] Many reactions were proposed to selectively modify the –OH groups on the basal plane of GO while maintaining the carboxylic acid functionalities that are required for imparting stabilization in aqueous systems.[19, 37-38] Nevertheless, currently it is a crucial challenge to develop LNC films exhibiting superior gas barrier property and reduced water sensitivity

for eco-friendly and mechanically flexible barrier films and waterborne coatings applications.

Herein, we report a simple approach for inexpensive and environmentally friendly fabrication of latex nanocomposite films by incorporating modified GO (mGO) into a styrene-acrylic latex using water as the processing solvent. The focus on styrene-acrylic latex as the polymer matrix is based on the wide use of these materials in coatings and adhesives applications – use that can be attributed to their low cost, excellent continuous film formation, durability, weatherability, and heat, corrosion and stain resistance.[39] mGO nanosheets were synthesized via esterification of the surface hydroxyl groups on GO with α-bromoisobutyryl bromide to decrease hydrophilicity of the nanofiller and improve the water sensitivity of the LNC films. Specifically, a poly (styrene-ethylhexyl acrylate-methacrylic acid) (P-St-EHA-MAA) latex was synthesized and used for the preparation of LNC films containing 0.025–1.2 wt.% mGO. The thermal, mechanical, and water vapor sorption properties of the LNC films were characterized and are described as a function of mGO loading. We further describe how changes in the nanocomposite morphology as a function of mGO loading alter the oxygen permeability, diffusivity, and solubility properties of the LNC films. Finally, we show that a relatively low loading level of mGO (1.2 wt.%) provides a significant decrease (≈ 84%) in oxygen permeability relative to latex films devoid of mGO – a result that points to the possible use of these LNC films in high performance barrier applications.

2.2 Experimental Section

2.2.1 Materials

All solvents and chemicals were purchased from Sigma-Aldrich and used as received without further purification unless otherwise specified. Reagents used for synthesizing the latex included styrene (St, 99.9% pure, distilled under vacuum to remove inhibitor), methacrylic acid (MAA, 99% pure), 2-ethylhexyl acrylate (EHA, 98% pure), ammonium persulfate (APS, 98% pure); and surfactants Igepal® CO-887 and Rhodapex® CO-436 (donated by Rhodia). Reagents for preparing mGO included graphite flakes (cat.#332461, ~150 μm), potassium permanganate (99% pure), phosphoric acid (85% H_3PO_4 in water), sulfuric acid (95–98% H_2SO_4), hydrogen peroxide (30 wt.% H_2O_2 in water), hydrochloric acid (30–35% HCl in water), ethyl alcohol (70% ethanol in water), tetrahydrofuran (THF, anhydrous, 99.9% pure), N-methyl-2-pyrrolidone (NMP, anhydrous, 99.5% pure), α-bromoisobutyryl bromide (98% pure), and triethylamine (TEA, 99% pure), ammonium hydroxide (NH_4OH, 28–30%), BYK®-428 (donated by BYK Additives), and in-house deionized (DI) water (MilliQ, 18 MΩ). The synthetic route of the styrene-acrylic latex resin using ammonium persulfate (APS) as the initiator is shown in Figure A.1.
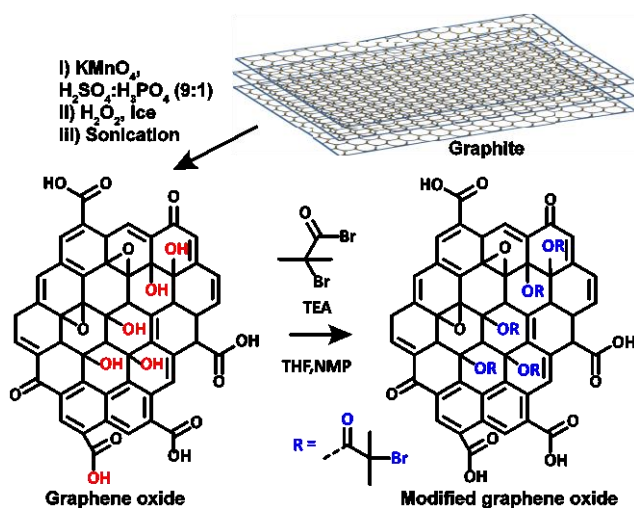
Figure 2.1 Synthetic route to graphene oxide and modified graphene oxide.

2.2.2 Synthesis and Modification of GO

The synthesis of GO and mGO is illustrated in Figure 2.1. GO was synthesized according to a well-reported method.[24] Modified GO was prepared by surface modification of GO via esterification of the surface hydroxyl groups on GO with α-bromoisobutyryl bromide.[37] A concentrated H_2SO_4/H_3PO_4 (120/13.3 by volume) blend was slowly added to a mixture of graphite flakes (1.0 g) and $KMnO_4$ (6.0 g) in a round-bottomed flask kept in an ice bath. The temperature was elevated to 50 °C and maintained under constant mechanical stirring at 900 rpm for 16 h. The flask was then cooled to ambient temperature and its contents were poured into ~ 200 mL of ice containing 2 mL of H_2O_2. The mixture turned bright yellow and the ice melted due to the resulting exothermicity. The blend was centrifuged at 6000 rpm for 1 h and the supernatant was decanted. The solid residue was washed successively with water, HCl, ethanol, and DI water, filtered, and centrifuged at 6000 rpm for 2 h. The solid residue was dried in a vacuum oven at 40 °C to yield GO.

GO (200 mg) was added into a 250 mL round bottom flask containing NMP (100 mL) and THF (50 mL). Ultrasonication for 1.5 h yielded a dark brown dispersion without any noticeable agglomerates. The flask was placed in water bath on a magnetic stirrer and a nitrogen stream was applied. Then, α-bromoisobutyryl bromide (2 mL) and TEA (1.8 mL) were added slowly into the flask and the reaction proceeded at ambient temperature for 36 h. The reaction mixture was centrifuged and the solid residue was washed successively with DI water and ethanol, and dried overnight in a vacuum oven to yield mGO.

2.2.3 Synthesis of The Styrene-Acrylic Emulsion

A styrene-acrylic emulsion (St/EHA/MAA = 59.5/39.5/1.0 by weight) was

prepared via starved semi-continuous emulsion polymerization with APS as the initiator

and surfactants Igepal CO-887 and Rhodapex CO-436.[40] The seed emulsion (St/EHA =

60.5/39.5 by weight) was loaded into a reactor equipped with a stirrer, condenser,

constant nitrogen flow pipe, and two feed pumps. The monomers were blended with

emulsifiers in DI water under high shear for 30 min, and fed drop wise into the reactor by

a pump. Simultaneously, an aqueous solution of the APS initiator was fed separately to

the reactor via another pump. The polymerization was conducted at 83 °C for 7 hours and

then cooled to ambient temperature under constant stirring. The resulting emulsion was

filtered through a metal mesh and its pH was adjusted to ~ 7 with ammonium hydroxide.

2.2.4 Preparation of LNCs and Film Fabrication

In a typical procedure, mGO was dispersed in DI water via ultrasonication before

adding a high shear thickener (BYK®-428). The mixture was shaken for 1 h and blended

with the styrene-acrylic emulsion. LNC films were cast in silicon-rubber molds and dried

at 50 °C/10 h + 60 °C/10 h. The films were cooled to ambient temperature and allowed to

rest for 48 h before evaluation. The complete LNC formulation is provided in Table A.1.

The mGO dispersion concentration was varied from 0.5 to 4 mg mL^{-1} to prepare LNCs

with different filler content. LNCs containing GO were also prepared similarly.

2.2.5 Measurements and Instrumentation

The synthesis and modification of GO was monitored by Raman spectroscopy,

and attenuated total reflectance-Fourier transform infrared (Thermo Scientific, ATR-

FTIR) spectroscopy. A Raman (Thermo Scientific, DER^{TM} Raman) microscope was used

to study the excitation of amorphous carbon bonds universally observed in carbon-based

materials and their derivatives, namely CNTs, graphene, and amorphous carbon.[41-42] All Raman spectra were measured using an excitation wavelength of 532 nm. Light transmission through the films was determined with a Lambda 35 Ultraviolet-visible (UV-Vis) spectrometer (PerkinElmer, Inc.) with a 326 nm UV lamp. X-ray photoelectron spectroscopy (XPS) analyses of GO and mGO were performed on a Thermo Scientific K-Alpha X-ray spectrometer at a maximum background pressure of 2×10^{-9} mbar. Thin film (or graphite flakes) samples used for characterization were deposited on silicon wafers using a small amount of DI water and dried for 1 h in air. The X-ray source utilized an Al anode emitting Al Kα X-rays (1486.6 eV) focused into a spot size of 400 µm. The collected spectra were processed using CasaXPS software and the quantification was expressed in relative atomic percentage with a sensitivity of 0.5–1 at.%. Curve fitting of the C1s and O1s XPS spectra was performed using a Gaussian-Lorentzian peak shape.

Minimum film formation temperature (MFFT) of latex was determined on a MFFT-BAR instrument (Rhopoint, Inc., temperature range −5 to 90 °C). The LNCs dispersion morphology was studied using a ZEISS scanning electron microscopy (MERLIN SEM) in high-vacuum mode. SEM samples were prepared by freeze-drying the dispersion followed by sputter coating with silver. The thicknesses of the exfoliated GO and mGO lamellae were determined via atomic force microscopy (AFM) in tapping-mode with a SiC probe (1/T300 TM, Bruker). Distribution morphology of the GO and mGO filler in the polymer matrix was studied via JEOL 2100 transmission electron microscopy (TEM), operated at 200 kV. Ultra-thin (~100 nm) sections of LNCs film samples embedded in epoxy resin for TEM studies were obtained using a microtome at RT and collected with a copper grid.

Dynamic mechanical analysis was performed on a Q800 DMA (TA Instruments) in multi-frequency-strain mode at 1 Hz and 2 °C min⁻¹ ramping. The glass transition temperauter (T_g) was measured via differential scanning calorimetry on a Q2000 DSC (TA Instruments) at a 10 °C min⁻¹ heating rate in nitrogen. Degradation profile was investigated via thermogravimetric analysis (Q500 TGA, TA Instruments) at 10 °C min⁻¹ heating rate in air. Mechanical tensile testing was performed following modified ASTM D 618 on a universal testing machine (Alliance RT/10 MTS) with a crosshead speed of 10 mm min⁻¹ at ambient temperature. Rectangular LNC strips were mouthed to the clamps with both ends wrapped up in tape. Water vapor absorbance of LNC films was tested via dynamic vapor sorption on a Q5000 SA (TA Instruments) at 25 °C and 98% relative humidity (RH) for 6 hours in isothermal equilibrium. Samples were equilibrated at 85 °C and 0% RH for 1.5 h before testing.

Oxygen barrier of the LNC films and neat polymer were measured at 25 °C, 0% RH, and 1 atm partial oxygen pressure difference using a commercially manufactured diffusion apparatus, OX-TRAN® 2/21 ML (MOCON) which employs a continuous-flow method (ASTM D3985-81) with nitrogen as a carrier gas to measure oxygen flux through polymeric films. Film samples with a surface area of 5 cm² were used for testing. The specimens were conditioned in a vacuum desiccator for more than 12 hours before testing to remove any traces of oxygen. Oxygen flux, $J(t)$, was measured. A solution to Fick's second law was employed (Eq. 1) to fit the experimental oxygen flux data, where Δp is the oxygen partial pressure difference across the film (1 atm here), l is the thickness of the film and t is the time (in second). From this two parametric fit the permeability P and diffusivity D were calculated as described elsewhere.[10]

$$J_{(t)} = \frac{P\Delta p}{l}\left[1 + 2\sum_{n=1}^{\infty}(-1)^n \exp\left(-\frac{D\pi^2 n^2 t}{l^2}\right)\right] \qquad (1)$$

The solubility S was calculated from the relationship $P = D \times S$. The permeability coefficient P can also be calculated directly from the steady-state flux J_∞ value as follows $P = J_\infty l/\Delta P$. The volume fractions (φ) of mGO were calculated according to Eq. 2 using the weight concentration (wt.%) of the fillers. Densities of the neat polymer and mGO fillers[43] used for calculating the volume fraction (φ) were (ρ_1) 1.04 g cm^{-3} and (ρ_2) 1.8 g cm^{-3}, respectively. The standard permeability unit (SPU) is expressed in terms of Barrer (1 Barrer = 10^{-10} (cm^3 O$_2$) cm cm^{-2} s^{-1} cmHg^{-1}).

$$\varphi = \frac{\dfrac{wt}{\rho_2}}{\dfrac{wt}{\rho_2} + \dfrac{100 - wt}{\rho_1}} = \frac{wt}{wt + \dfrac{\rho_2}{\rho_1}(100 - wt)} \qquad (2)$$

2.3 Results and Discussions

2.3.1 Characterization of GO and mGO

X-ray photoelectron spectroscopy (XPS) spectra, Fourier transform infrared spectrum (FTIR), and Raman spectrum of GO and mGO are displayed in Figure 2.2. The proportions of functional groups were calculated from deconvoluted C1s and O1s spectra and are listed in Tables A.2–A.5. Figures 2.2a–c show XPS survey, high-resolution C1s and O1s spectra of GO, respectively. The C1s spectrum of GO (Figure 2.2b) was deconvoluted into four peaks that correspond to the following functional groups: sp^2 carbon (C=C, 284.7 eV), epoxy/hydroxyl (C–O, 286.5 eV), carbonyl (C=O, 287.1 eV), and carboxyl/ester (O–C=O, 289.0 eV).[24, 44] Figures 2.2d–f show XPS survey, high-resolution C1s and O1s spectra of mGO, respectively. The mGO C1s spectrum can also be deconvoluted into four different components: sp^2 carbon (C=C, 284.6 eV),

37

epoxy/hydroxyl/carbon–bromine (C–O/C–Br, 286.5 eV), carbonyl (C=O, 287.1 eV), and

carboxyl/ester (O=C–O, 288.7 eV) (Figure 2.2e).[24, 44]

In comparison to the deconvoluted C–O peak of GO, the deconvoluted peak

located at 286.5 eV of mGO was assigned both to C–O and C–Br bond.[45] This

assignment can be ascribed to the surface modification of GO via esterification of the

surface hydroxyl groups on GO with α-bromoisobutyryl bromide (Figure 2.1).[37] The

primary purpose of the GO surface modification was to decrease the hydrophilicity. The

characteristic C–Br bond was further manifested by the appearance of a single peak at

70.8 eV, which was attributed to a Br-3d excitation process (Figure A.2).[45] The O1s

spectrum of GO (Figure 2.2c) was deconvoluted into three peaks representing three types

of oxygenate bonds, i.e., O=C–O (531.0 eV), O=C (532.6 eV), and O–C (533.7 eV).[44]

The O1s spectrum of mGO (Figure 2.2f) can also be deconvoluted into three peaks

corresponding to three types of oxygenate bonds, i.e., O=C–O (531.3 eV), O=C (532.4

eV), and O–C (533.2 eV).[44] The O1s deconvoluted peaks of mGO exhibited a decrease

of O–C and an increase of O=C–O concentration proportions (Tables A.4 and A.5),

which also validated the successful modification of hydroxyl groups on GO.

FTIR spectra of GO indicated the presence of the following functional groups

(Figure 2.2g): O–H stretching vibration (3400 cm^{-1}), C=O stretching vibration (1750–

1650 cm^{-1}), and C–O vibrations (1250–950 cm^{-1}).[24, 46] The bands in the mGO spectrum

(3000–2800 cm^{-1} and 1460–1380 cm^{-1}) were attributed to the vibrations of –CH$_3$ groups,

specifically, the peaks at ~ 2930 and ~ 2860 cm^{-1} represent C–H vibration on the –CH$_3$

moiety.[37] The pronounced reduction of peak intensity in the wide band of the mGO

spectrum at ~ 3600–3000 cm^{-1} (relative to GO) is ascribed to the partial loss of –OH groups upon modification.
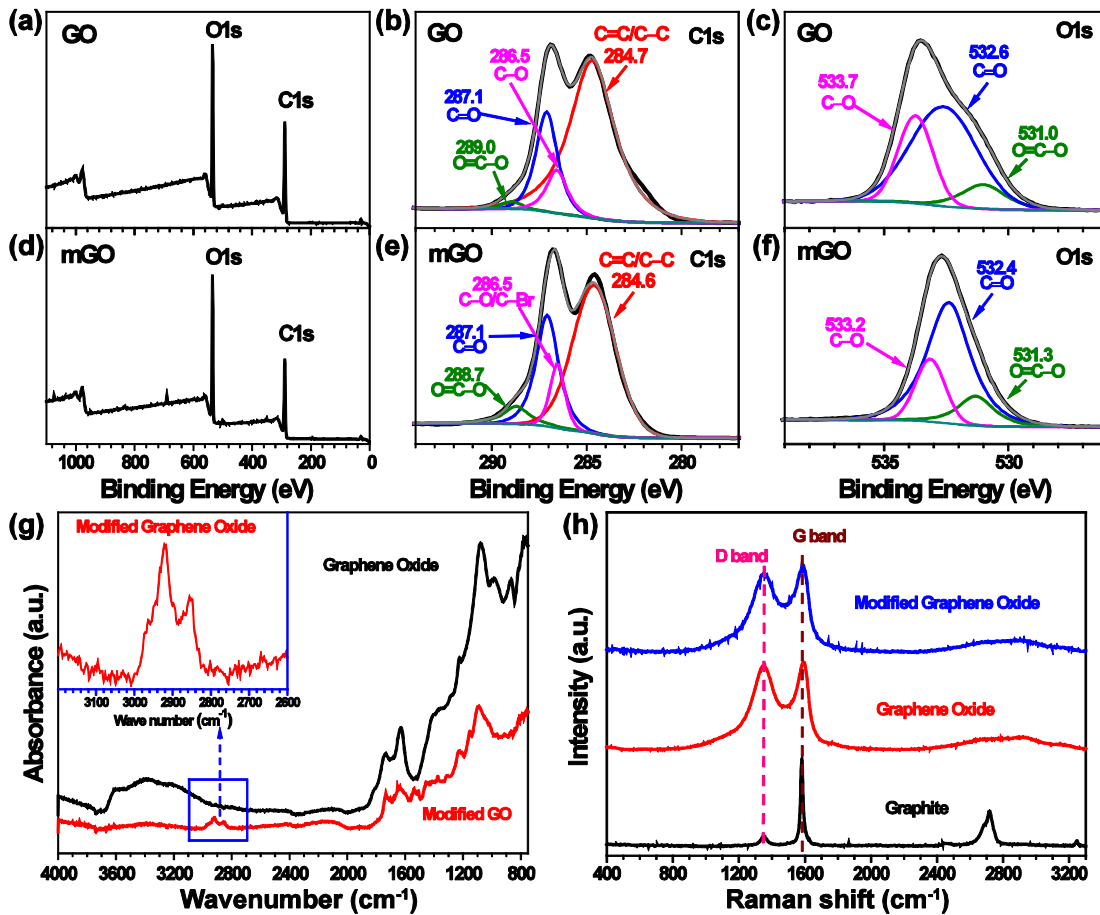
Figure 2.2 XPS spectra of (a) survey scan, (b) C1s and (c) O1s of GO. XPS spectra of (d) survey scan, (e) C1s and (f) O1s of mGO. (g) FTIR spectra of the functional groups on GO and mGO. (h) Raman spectra of graphite, GO and mGO.

Raman spectroscopy is a widely used nondestructive tool to characterize carbon materials owing to the high intensities of disordered graphite sp^2 carbon bonds.[42] The G peak at around 1580~1600 cm^{-1} is due to the first order scattering of the E$_{2g}$ phonon of in-plane vibrations of sp^2 bonded carbon atoms.[42] The D peak at around 1350 cm^{-1} originates from a defect-induced A$_{1g}$ breathing mode of sp^2 rings.[41-42] The intensity of the D band is related to the size of sp^2 domains. The peak intensity ratio of I$_D$/I$_G$ is a measure

39

of the disorder degree, which is inversely proportional to the average size of the sp^2

clusters.[41-42] Raman spectra of graphite, GO, and mGO all indicated the presence of G

($\sim$1580 cm^{-1}) and D ($\sim$1350 cm^{-1}) bands (Figure 2.2h).[24, 42, 47] The highly ordered 3D

structure of graphite showed multiple Raman-active bands: the in-phase vibration (G

band) of the lattice, weak disorder band (D band) caused by graphite edges, and a peak at

2710 cm^{-1} that was ascribed from the second order of D band on graphite and multi-layer

graphene.[41, 47] During amorphization of graphite, sp^3 carbons were formed which leads to

a broadening of both G and D band due to increased disorder. Extended ultrasonication,

required for dispersing GO prior to modification, generates topological defects and

vacancies and can also result in a slight broadening of the G and D bands.[47] However,

the I_D/I_G ratio calculated from the normalized intensity of D and G bands for GO (0.953)

and mGO (0.922) is quite close, indicating that the modification procedure has little

impact on the scaffold structure.

The AFM height image of an exfoliated GO nanosheet coated on the smooth

surface of a silicon wafer is displayed in Figure A.3a. The GO nanosheet exhibited an

irregular shape with a thickness of $\sim$1.2 nm as indicated from the height profile (Figure

A.3b), which is consistent with the values reported for exfoliated GO lamellae by other

researchers.[24] An average aspect ratio of $\sim$2800 can be expected for fully exfoliated GO

nanosheet dispersed in aqueous suspension. Figures A.3c and A.3d show the AFM height

images and the profiles of surface modified mGO nanosheets. The mGO nanosheet

shown in Figure A.2c exhibited folding and some wrinkles on the surface and some small

fragments were found attached to the larger nanosheets. The lamellar thickness was $\sim$1.1

nm with an average aspect ratio of ~800, which resulted from the extended

ultrasonication that reduced the size of GO nanosheets.[24, 27]

2.3.2 LNC Aqueous Dispersion and Film Formation
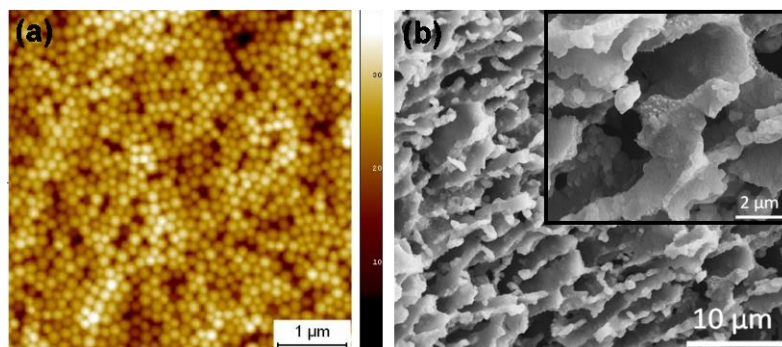
Figure 2.3 (a) AFM height image of the latex particles. (b) SEM images of freeze-dried
LNC dispersion with 0.1 wt.% mGO.

AFM height imaging (Figure 2.3a) shows the spherical morphology of the latex

particles with an average diameter of ~150 nm and highly uniform size distribution. To

investigate the dispersion state of mGO lamellae in emulsion, the LNCs dispersion was

freeze-dried and sputter coated for SEM characterization. Upon freeze-drying, mGO

nanosheets form gelation structures via hydrogen bonding, π-π stacking, and electrostatic

interactions.[48] Figure 2.3b shows the three-dimensional porous scaffold covered with

small latex particles indicating good dispersing of mGO nanosheets in aqueous systems.
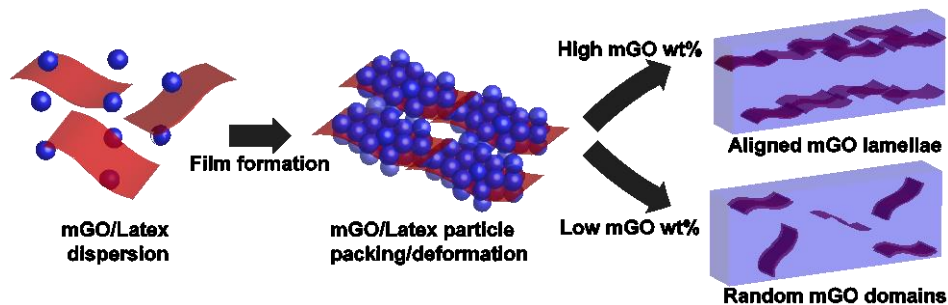
Figure 2.4 Schematic representation of the LNC film formation and morphology
development.

41

A schematic representation of the LNC film formation process in the presence of mGO nanofiller is illustrated in Figure 2.4. Since both mGO and the latex nanoparticles disperse very well in water, the mGO intercalates with the latex nanoparticles and forms a stable colloidal dispersion without agglomeration, as shown in Figures 2.3b.[22, 29] During film formation, latex nanoparticles undergo packing as water evaporates creating excluded volume that forces mGO nanosheets into the interstitial spaces between latex nanoparticles.[34-36] As time elapses, the latex nanoparticles deform and interfuse at the nanoparticle boundaries to bind with each other, followed by chain entanglement to yield a continuous film.[29] The LNC morphology obtained depends on several factors, including filler-filler interactions, filler-matrix interactions, filler loading, and the relative dimensions of the latex and mGO.[49] mGO/LNC films were fabricated at 50–60 °C – well above the MFFT of the nanocomposite (27.5 °C) to ensure good film quality.[29] The nomenclature of mGO-0.1 indicates 0.1 wt.% mGO on resin solids in the nanocomposite. Digital photo images of free-standing LNC films with different mGO loadings are shown in Figure 2.5. As expected, the transparency of the LNC films decreased with increasing mGO loading. LNCs containing 1.2 wt.% mGO yielded completely opaque films – an observation that was further confirmed by UV-vis spectroscopy (Figure A.4). Optical microscopy (Figure A.5) also indicated good uniformity of LNC films with few large aggregates. Raman spectroscopy was used to confirm a uniform increase in mGO concentration (Figure A.6). TEM was employed to directly observe the dispersion state and morphology of the LNCs using microtomed thin sections.
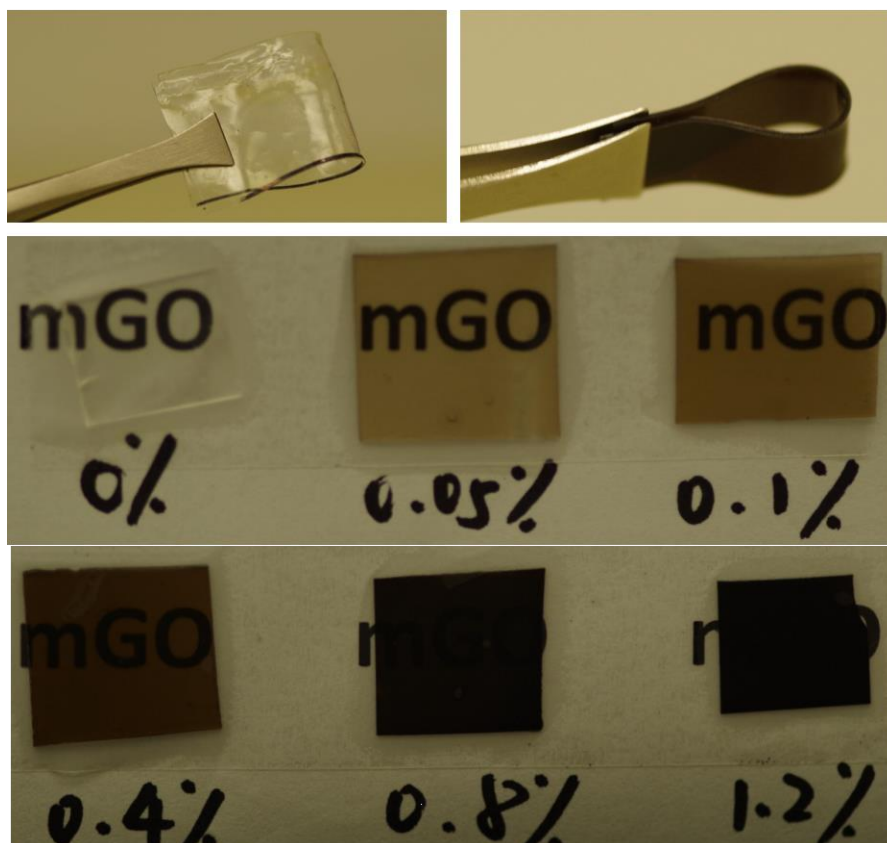
Figure 2.5 Digital images of LNC films with different mGO loadings.

Figure 2.6 shows cross-sectional TEM images of mGO/LNC films at various loading levels. The mGO provided adequate contrast against the polymer matrix to be imaged without staining.[50] Uniform dispersion of mGO was observed at each concentration. At low mGO loading (0.125 wt.%), the mGO domains exhibited a random orientation with several microns between mGO domains (Figure 2.6a). Increasing the mGO concentration to 0.8–1.2 wt.% resulted in alignment of the mGO domains and the formation of a lamellar-like morphology, with a distance between mGO lamellae of several hundred nanometers (Figure 2.6e–g).
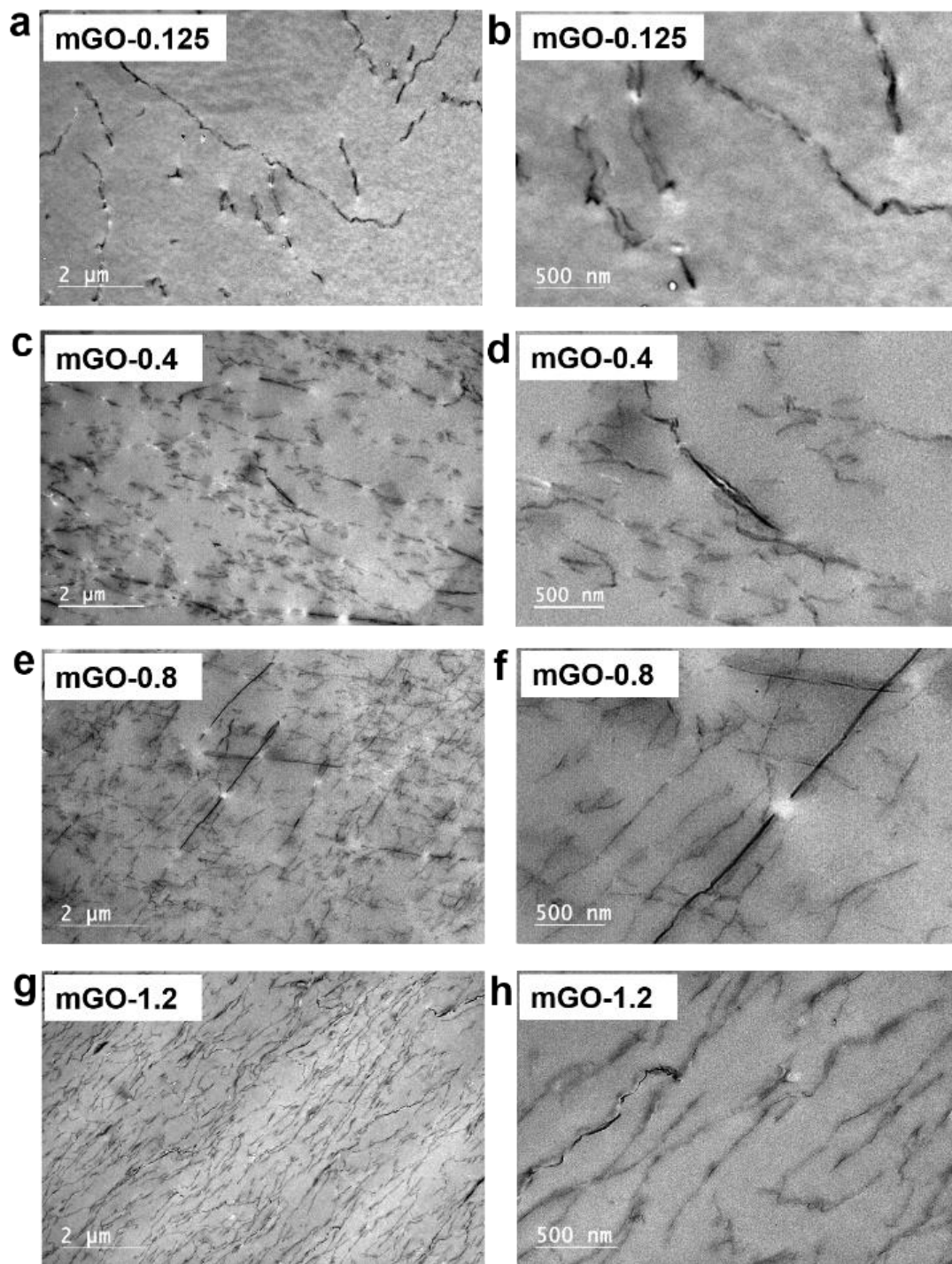
Figure 2.6 Cross-sectional TEM images of mGO/LNC films with different mGO loadings under low and high magnifications: (a,b) 0.125 wt.%, (c,d) 0.4 wt.%, (e,f) 0.8 wt.%, and (g,h) 1.2 wt.%.

At 1.2 wt.% (Figure 2.6g and 2.6h), the aligned mGO lamellae can be estimated to be ~ 0.5–5 μm in length and ~ 5–15 nm in thickness – dimensions that indicate the mGO nanosheets stack during the film formation process. The aligned lamellar morphologies are in good agreement with work by Yousefi *et al.*[51] that attributed alignment to steric interactions between GO sheets, and are typically observed when the lateral GO dimensions are larger than the diameter of the latex nanoparticles. For comparison, the cross-sectional TEM images of GO/LNC films at various loading levels (0.2–1.2 wt.%) are shown in Figure A.7. The distribution and morphology of GO nanoplatelets in LNC films with different GO loadings were similar to that observed for mGO/LNCs, where a 1.2 wt.% GO loading also resulted in aligned lamellar morphologies (Figure A.7). Thus, chemical modification of GO played a minimal role in the final LNC morphology.

2.3.3 Thermal and Mechanical Properties of LNC Films

The glass transition temperatures (T_g) of the LNC films, as determined via differential scanning calorimetry (DSC) and dynamic mechanical analysis (DMA), are summarized in Table A.6. A T_g (DSC) difference of 1.9 °C was noted between the pristine latex and LNCs containing 1.2 wt.% of mGO composite films (Figure A.8a). Similarly, a T_g (DMA) range of 2 °C was observed via the tan δ peak (Figure A.8b) and 2.3 °C when measured from the first derivative of the storage modulus (E′) curves (Figure 2.7a). The steady rise in storage modulus of the LNC films with increasing mGO loadings (Figure 2.7a) can be attributed to increased interfacial interactions between mGO and polymer matrix, thereby resulting in restricted chain mobility and increased stiffness of LNC films.[21-22]
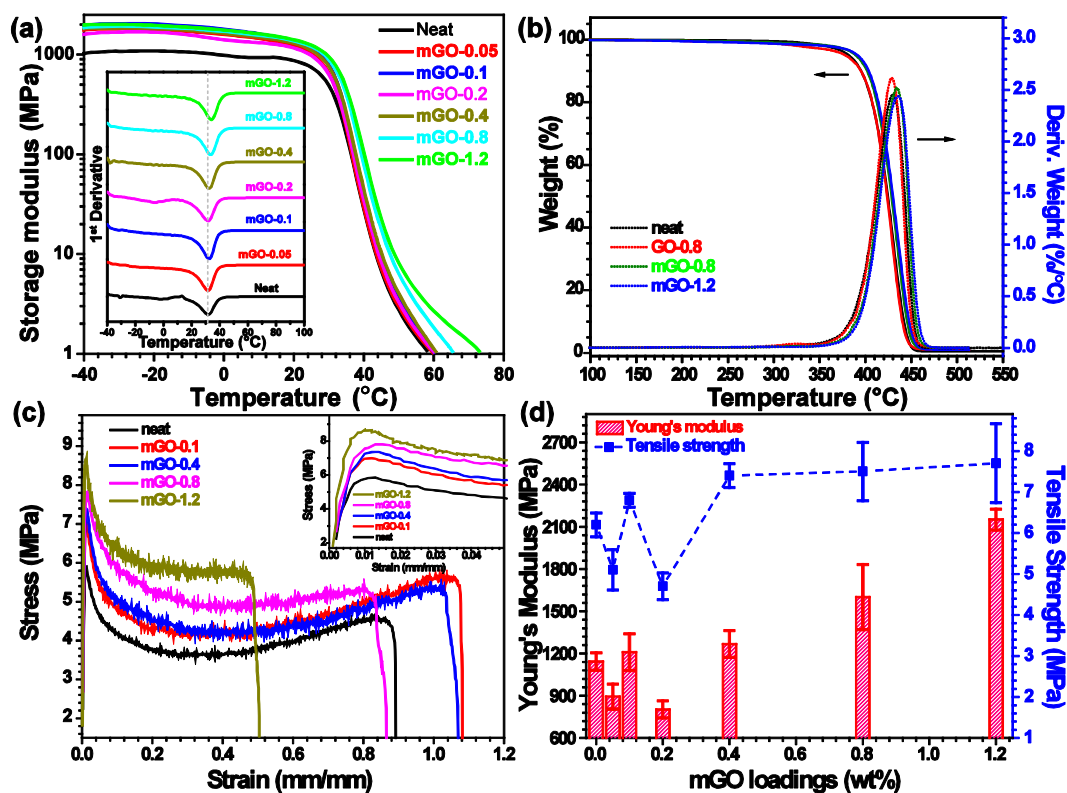
Figure 2.7 Thermal mechanical testing of mGO/LNC films (a) DMA storage modulus and first derivative, (b) TGA and its weight loss derivative curves. Mechanical tensile properties of mGO/ LNC films (c) stress-strain curve, (d) tensile strength and Young's modulus at ambient temperature.

Figure 2.7b shows the TGA thermograms of LNC films containing GO and mGO. The temperature at 5% weight loss ($T_{d,5\%}$) for the GO-0.8/LNC film was lower by ~ 4 °C in comparison to the neat sample ($T_{d,5\%}$, 382 °C). In comparison to the neat sample, the $T_{d,5\%}$ values for the mGO-0.8 and mGO-1.2/LNC films were higher by ~ 7 and 10 °C, respectively. TGA studies indicated a small shift towards a higher degradation temperature for LNC films with increasing mGO loading. Figure 2.7c displays the stress-strain curves of LNC films at different mGO loadings. The sample with the highest mGO loading (mGO-1.2) exhibited the lowest strain-at-break (0.48 mm mm–1) and highest tensile strength (8.65 MPa). The mGO-0.1 sample demonstrated the highest strain-at-

break (1.07 mm mm–1), and larger tensile strength (6.89 MPa) than the neat sample (5.85

MPa).
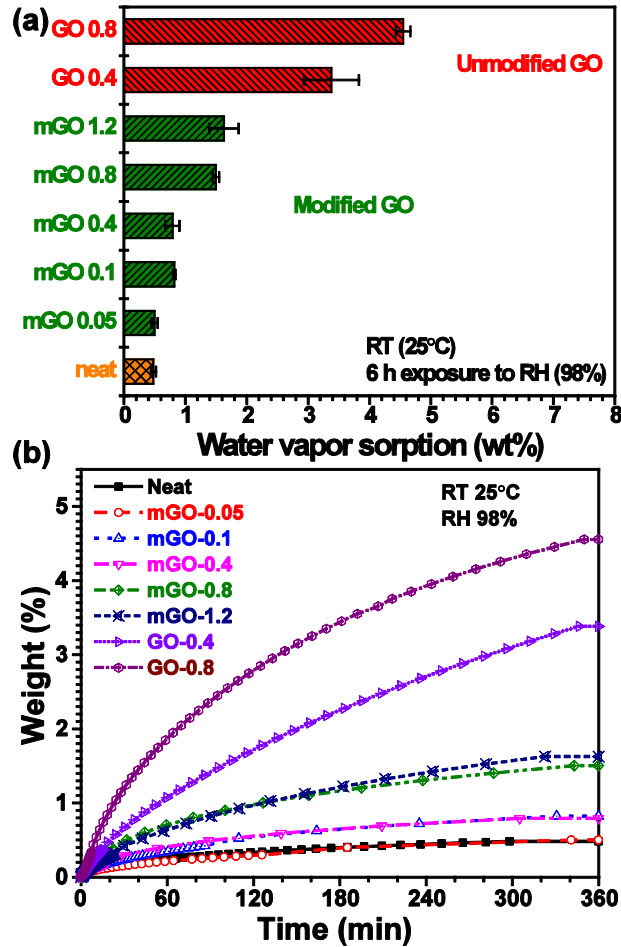
Figure 2.8 (a) Water vapor sorption of LNC films in 98% RH air for 6 h and (b) dynamic weight change versus time curves.

Figure 2.7d displays the Young's modulus and average tensile strength of the

LNC films as a function of mGO loading. An increase in mGO loading was associated

with a decrease in strain-at-break and increased Young's modulus, indicating that mGO

contributes to polymer matrix stiffening. The interruption in latex nanoparticle

deformation and chain entanglement by mGO lamellae causes the LNC films becoming

47

less rubbery, thereby resulting in increased Young's modulus and decreased strain-at-break.[16, 29, 34-35]

2.3.4 Water Vapor Sorption of LNC Films

Water vapor sorption analysis of LNC films containing 0.05–1.2 wt.% of mGO were compared with those containing 0.4 and 0.8 wt.% GO (Figure 2.8a). LNC films containing GO absorbed more moisture than LNC films containing similar amounts of mGO. For instance, the film containing 0.8 wt.% mGO absorbed 67% less moisture than the film with 0.8 wt.% GO in the dynamic water vapor sorption test (Figure 2.8a). The higher water vapor sorption in samples containing GO can be attributed to more hydrophilic groups existing on GO nanosheets, which leads to greater moisture retention in the films.[52] The weight change versus time curves (Figure 2.8b) taken from the dynamic water vapor sorption tests indicate LNC films with GO absorbed moisture much faster than LNC films with mGO (25 °C, 98% relative humidity).

2.3.5 O_2 Permeability of LNC Films

Oxygen flux curves for all of the nanocomposite films, normalized to the same film thickness, are depicted in Figure 2.9a. The curves show both the non-steady state and steady state regions of oxygen permeation. The slope of the non-steady state region is mainly controlled by the diffusivity while the steady state region is controlled by the permeability. As one can clearly see, adding a small amount of mGO dramatically affected both the slope of the non-steady and the steady state regions of the oxygen flux curves as compared to that of the neat polymer, making them shallower and reducing the steady state value. The oxygen permeability, diffusivity, and solubility coefficients were calculated from the oxygen flux data as described in the Experimental Section. A

48

representative plot of an experimental fit to Fick's second law is included in Figure A.9. Figures 2.9b–d display permeability, diffusivity, and solubility changes with mGO volume fraction added. This data is also summarized in Table 2.1.

A decrease of permeability in nanoplatelet based composite systems has been primarily attributed to a drop in gas diffusivity as the added particles create a more tortuous pathway for the penetrating gas molecules through the composite.[3-7] This decrease in diffusivity is affected by the volume fraction (φ), aspect ratio ($\alpha = 2R/d$), orientation, and the dispersion state of the nanoplatelets throughout the composite.[10, 17-18] As compared to diffusivity, the solubility is an additive thermodynamic property so it should depend linearly on the volume fraction of the gas insoluble phase (presumably the filler) assuming that the polymer solubility does not change in the presence of the filler.[8]

As shown in Figure 2.9b and Table 2.1, the permeability of the LNCs progressively decreased with the mGO loading. The addition of only 0.7 vol.% mGO decreased the oxygen permeability of the nanocomposite by 84% as compared to the neat polymer, which is a considerable gas barrier improvement. For comparison, we also analyzed the oxygen gas permeability performance of GO/LNC films with different GO loadings. The results are shown in Figure A.10 and summarized in Table A.7. Adding 0.7 vol.% GO decreased the oxygen permeability of the nanocomposite by 78% relative to the neat polymer, which is 6% less than that of the mGO/LNC film with similar loading. Similar results are expected from the mGO and GO LNCs as the modification did not significantly alter the dispersion or morphology of the LNC films, as previously discussed. For context, we have compared the oxygen permeability for the 1.2wt.% (0.7vol.%) mGO/LNC (0.69 Barrer) and GO/LNC (0.98 Barrer) films reported herein

with other polymer/graphene oxide nanocomposite systems reported in the literature

(Table 2.2).
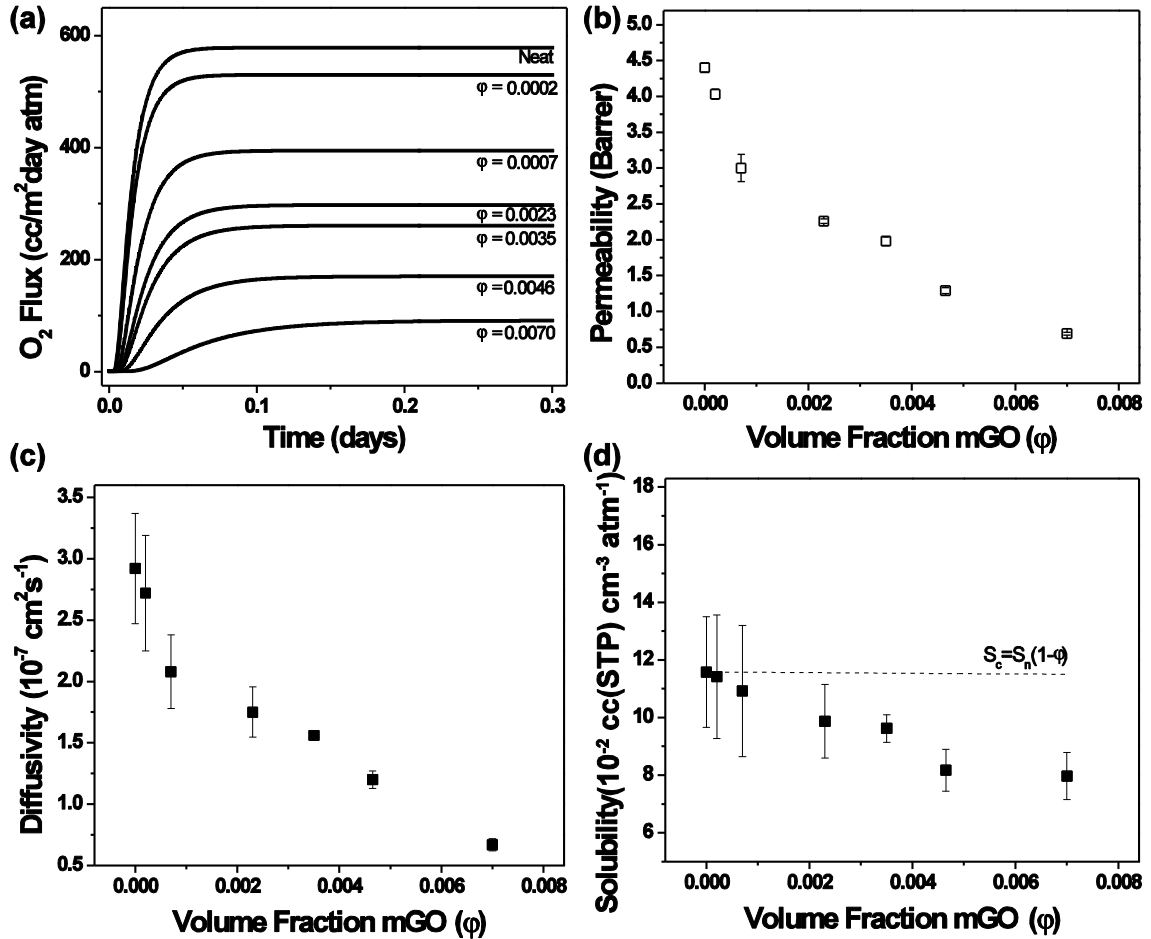
Figure 2.9 (a) Generated O_2 flux curves for 0.5 mm LNC films, (b) permeability, (c) diffusivity, and (d) solubility plots vs. volume fraction mGO. Error bars represent uncertainties from sample measurement variance and the fits to Fick's second law.

The oxygen permeability changes exhibited a stronger decrease at very low

loadings (0–0.07 vol.%) while at higher loadings (0.2–0.7 vol.%) the rate of change

reduced (Figure 2.9b). Interestingly, this behavior was similar to that reported by

Compton et al.[16] especially when smaller loadings were considered. However, the

reduction in permeability was steeper in this study than that by Compton et al. at higher

loadings.[16] As expected, the diffusivity trend, which is shown in Figure 2.9c, exhibited an

apparent correlation with the permeability trend indicative that an increase in tortuosity of the diffusion path was the predominant cause of the permeability reduction. The diffusivity describes the kinetic aspect of the transport that reflects the mobility of the gas molecules in the polymeric phase.[3, 8] The diffusivity decreased by 77% at the highest loading (0.7 vol.%) measured.

Table 2.1 O_2 gas permeability, diffusivity, and solubility of LNC films with different mGO loadings.

Sample (wt.%)	Volume Fraction mGO (φ)	Permeability (P) [Barrer]	Relative Permeability (P_c/P_n)	Diffusivity (D) [10^{-7} cm^2 s^{-1}]	Relative Diffusivity (D_c/D_n)	Solubility (S) [10^{-2} cc(STP) cm^{-3} atm^{-1}]	Relative Solubility (S_c/S_n)
Neat-0	0.0000	4.40 ± 0.06	1.00	2.92 ± 0.45	1.00	11.6 ± 1.92	1.00
mGO-0.025	0.0002	4.03 ± 0.07	0.92	2.72 ± 0.47	0.93	11.4 ± 2.14	0.98
mGO-0.125	0.0007	3.00 ± 0.19	0.68	2.08 ± 0.30	0.71	10.9 ± 2.28	0.94
mGO-0.4	0.0023	2.26 ± 0.03	0.51	1.75 ± 0.21	0.59	9.87 ± 1.28	0.85
mGO-0.6	0.0035	1.98 ± 0.06	0.45	1.56 ± 0.03	0.53	9.62 ± 0.48	0.83
mGO-0.8	0.0046	1.29 ± 0.04	0.29	1.20 ± 0.07	0.41	8.17 ± 0.73	0.71
mGO-1.2	0.0070	0.69 ± 0.02	0.16	0.67 ± 0.05	0.23	7.97 ± 0.81	0.69

Typically changes in relative permeability in impermeable platelet filled nanocomposite systems are analyzed using a variety of tortuosity based models that show a correlation with filler loading concentration and aspect ratio, most commonly those devised by Nielsen[17] and Cussler.[18] However, even with our thorough morphological analysis (cross-sectional TEM images shown in Figure 2.6) it is difficult to determine an average aspect ratio of these platelets as there is a vast dispersity in platelet sizes ranging from small particles to enormous high aspect ratio nanoplatelets. Also, there is an apparent change in orientation of the particulates from a more random to an aligned orientation at higher loadings as seen in the cross-sectional TEM images (Figure 2.6).

Therefore, none of these models would prove useful in this circumstance; consequently, we have simply reported on the actual experimental data.

Table 2.2 Survey of O_2 permeability for polymer/graphene oxide nanocomposites.

Polymer matrix	Filler	Filler loading	Processing	Gas	Permeability [Barrer]	Reduction (%)	Reference
Styrene-acrylic latex	mGO	0.7 vol.%	Latex dispersion	O_2	0.69	84	This work
Styrene-acrylic latex	GO	0.7 vol.%	Latex dispersion	O_2	0.98	78	This work
PS	Gr [a*]	0.94 vol.%	Solution	O_2	2.44	49	[16]
PS	Gr [a*]	2.27 vol.%	Solution	O_2	1.84	61	[16]
PS	pv-GO [b*]	2 wt.%	In situ	O_2	2.24	25	[53]
PEI	GO	91 wt.%	LbL	O_2	3.3×10^{-7}	99.9	[54]
PMMA	Gr	0.5 wt.%	In situ	O_2	0.81	70	[55]
PVA	GO [c*]	0.72 vol.%	Solution	O_2	3.2×10^{-3}	98.9	[56]
SBR	Gr	7 wt.%	Latex compounding	O_2	NA	87.8	[57]

Note: [a*] graphene/reduced graphene oxide; [b*] p-phenylenediamine/4-vinylbenzoic acid-modified graphene oxide (pv-GO); [c*] tested at room temperature with 50% relative humidity; PS: polystyrene; PEI: polyethylenimine; PMMA: poly(methyl methacrylate); PVA: poly(vinyl alcohol); SBR: styrene-butadiene rubber; LbL: layer-by-layer.

The solubility trend is shown in Figure 2.9d. The solubility relates to the penetrant affinity and the thermodynamic aspect of the transport that associated with the interactions between polymer and gas molecule.[3, 8] Unlike typical nanocomposite systems with low loadings of impermeable filler, the drop in permeability of these composite films was noticeably affected by a drop in solubility with increased filler content. At 0.7 vol.% mGO, there was a 31% decrease in solubility as compared to the neat polymer. This solubility decrease is unexpected as typically the solubility coefficient only changes with filler loading, $S_c = S_n(1-\varphi)$ as shown as a dashed line in Figure 2.9d, where S_c and S_n are the solubility coefficient of nanocomposite and polymer matrix, respectively.

However, there is precedent for this phenomenon in the work by Compton et al.[16] on a polystyrene/isocyanate-modified graphene system and a select others.[20, 56, 58] They attributed this drop in solubility to a densification of the system through increased polymer–graphene interactions that limited the formation of free volume between the polymer chains in the matrix. An alternative possibility we considered included the formation of regions in which polymer is trapped (screened) inside the very high aspect ratio nanoplatelet assemblies and does not participate in the dynamic permeation process. We plan to conduct a more thorough investigation of this interesting gas solubility phenomenon in the future by probing the free volume of the polymer matrix by positron annihilation lifetime spectroscopy and direct testing of gas solubility.

2.4 Conclusions

This study reports a facile and environmentally friendly fabrication of latex nanocomposites by incorporating surface-modified graphene oxide into a styrene-acrylic latex using water as the processing solvent. An 84% decrease (relative to the neat polymer) in oxygen permeability of LNC films was achieved by adding only 0.7 vol.% (1.2 wt.%) mGO. The oxygen barrier performance of mechanically flexible mGO/LNC films stems from the intrinsic impermeability, high aspect ratio, and complete exfoliation of mGO nanosheets, their uniform dispersion and high alignment in the polymer matrix, and strong interfacial adhesion between mGO and polymer matrix. The oxygen barrier property is in excellent agreement with cross-sectional TEM imaging of mGO/LNC films. Importantly, LNCs containing mGO absorbed 67% less moisture than LNCs with similar levels of unmodified GO due to fewer hydrophilic groups on mGO upon esterification. This work broadly defines a set of design parameters for ecofriendly

development of mechanically flexible latex/graphene oxide nanocomposite oxygen

barrier films with improved moisture resistance for potential utility in protective coating

and packaging applications.

2.5 References

1. Su, Y.; Kravets, V. G.; Wong, S. L.; Waters, J.; Geim, A. K.; Nair, R. R., Impermeable barrier films and protective coatings based on reduced graphene oxide. *Nat. Commun.* **2014,** *5*, 4843.
2. Vaia, R. A.; Maguire, J. F., Polymer Nanocomposites with Prescribed Morphology: Going beyond Nanoparticle-Filled Polymers. *Chem. Mater.* **2007,** *19* (11), 2736-2751.
3. Cui, Y.; Kundalwal, S. I.; Kumar, S., Gas barrier performance of graphene/polymer nanocomposites. *Carbon* **2016,** *98*, 313-333.
4. Huang, J.-C., Carbon black filled conducting polymers and polymer blends. *Adv. Polym. Tech.* **2002,** *21* (4), 299-313.
5. Kim, H.; Abdala, A. A.; Macosko, C. W., Graphene/Polymer Nanocomposites. *Macromolecules* **2010,** *43* (16), 6515-6530.
6. Moniruzzaman, M.; Winey, K. I., Polymer Nanocomposites Containing Carbon Nanotubes. *Macromolecules* **2006,** *39* (16), 5194-5205.
7. Möller, M. W.; Kunz, D. A.; Lunkenbein, T.; Sommer, S.; Nennemann, A.; Breu, J., UV-Cured, Flexible, and Transparent Nanocomposite Coating with Remarkable Oxygen Barrier. *Adv. Mater.* **2012,** *24* (16), 2142-2147.
8. Choudalakis, G.; Gotsis, A. D., Permeability of polymer/clay nanocomposites: A review. *Eur. Polym. J.* **2009,** *45* (4), 967-984.
9. Decker, J. J.; Meyers, K. P.; Paul, D. R.; Schiraldi, D. A.; Hiltner, A.; Nazarenko, S., Polyethylene-based nanocomposites containing organoclay: A new approach to enhance gas barrier via multilayer coextrusion and interdiffusion. *Polymer* **2015,** *61*, 42-54.
10. Nazarenko, S.; Meneghetti, P.; Julmon, P.; Olson, B. G.; Qutubuddin, S., Gas barrier of polystyrene montmorillonite clay nanocomposites: Effect of mineral layer aggregation. *J. Polym. Sci. B Polym. Phys.* **2007,** *45* (13), 1733-1753.
11. Priolo, M. A.; Holder, K. M.; Greenlee, S. M.; Stevens, B. E.; Grunlan, J. C., Precisely Tuning the Clay Spacing in Nanobrick Wall Gas Barrier Thin Films. *Chem. Mater.* **2013,** *25* (9), 1649-1655.
12. Ray, S.; Okamoto, M., Polymer/layered silicate nanocomposites: a review from preparation to processing. *Prog. Polym. Sci.* **2003,** *28* (11), 1539-1641.
13. Triantafyllidis, K. S.; LeBaron, P. C.; Park, I.; Pinnavaia, T. J., Epoxy−Clay Fabric Film Composites with Unprecedented Oxygen-Barrier Properties. *Chem. Mater.* **2006,** *18* (18), 4393-4398.
14. Geim, A. K.; Novoselov, K. S., The rise of graphene. *Nat. Mater.* **2007,** *6* (3), 183-191.

15.   Bunch, J. S.; Verbridge, S. S.; Alden, J. S.; van der Zande, A. M.; Parpia, J. M.; Craighead, H. G.; McEuen, P. L., Impermeable Atomic Membranes from Graphene Sheets. *Nano Lett.* **2008,** *8* (8), 2458-2462.

16.   Compton, O. C.; Kim, S.; Pierre, C.; Torkelson, J. M.; Nguyen, S. T., Crumpled Graphene Nanosheets as Highly Effective Barrier Property Enhancers. *Adv. Mater.* **2010,** *22* (42), 4759-4763.

17.   Nielsen, L. E., Models for the Permeability of Filled Polymer Systems. *J. Macromol. Sci. Part A: Chem.* **1967,** *1* (5), 929-942.

18.   Lape, N. K.; Nuxoll, E. E.; Cussler, E. L., Polydisperse flakes in barrier films. *J. Membrane Sci.* **2004,** *236* (1-2), 29-37.

19.   Dreyer, D. R.; Park, S.; Bielawski, C. W.; Ruoff, R. S., The chemistry of graphene oxide. *Chem. Soc. Rev.* **2010,** *39* (1), 228-240.

20.   Huang, H.-D.; Ren, P.-G.; Xu, J.-Z.; Xu, L.; Zhong, G.-J.; Hsiao, B. S.; Li, Z.-M., Improved barrier properties of poly(lactic acid) with randomly dispersed graphene oxide nanosheets. *J. Membrane Sci.* **2014,** *464*, 110-118.

21.   Putz, K. W.; Compton, O. C.; Palmeri, M. J.; Nguyen, S. T.; Brinson, L. C., High-Nanofiller-Content Graphene Oxide-Polymer Nanocomposites via Vacuum-Assisted Self-Assembly. *Adv. Funct. Mater.* **2010,** *20* (19), 3322-3329.

22.   Seyedin, M. Z.; Razal, J. M.; Innis, P. C.; Jalili, R.; Wallace, G. G., Achieving Outstanding Mechanical Performance in Reinforced Elastomeric Composite Fibers Using Large Sheets of Graphene Oxide. *Adv. Funct. Mater.* **2014,** *25* (1), 94-104.

23.   Hummers, W. S.; Offeman, R. E., Preparation of Graphitic Oxide. *J. Am. Chem. Soc.* **1958,** *80* (6), 1339-1339.

24.   Marcano, D. C.; Kosynkin, D. V.; Berlin, J. M.; Sinitskii, A.; Sun, Z.; Slesarev, A.; Alemany, L. B.; Lu, W.; Tour, J. M., Improved Synthesis of Graphene Oxide. *ACS Nano* **2010,** *4* (8), 4806-4814.

25.   Staudenmaier, L., Verfahren zur Darstellung der Graphitsäure. *Berichte der deutschen chemischen Gesellschaft* **1898,** *31* (2), 1481-1487.

26.   Zhu, Y.; Murali, S.; Cai, W.; Li, X.; Suk, J. W.; Potts, J. R.; Ruoff, R. S., Graphene and Graphene Oxide: Synthesis, Properties, and Applications. *Adv. Mater.* **2010,** *22* (35), 3906-3924.

27.   Paredes, J. I.; Villar-Rodil, S.; Martínez-Alonso, A.; Tascón, J. M. D., Graphene Oxide Dispersions in Organic Solvents. *Langmuir* **2008,** *24* (19), 10560-10564.

28.   Unalan, I. U.; Wan, C.; Figiel, Ł.; Olsson, R. T.; Trabattoni, S.; Farris, S., Exceptional oxygen barrier performance of pullulan nanocomposites with ultra-low loading of graphene oxide. *Nanotechnology* **2015,** *26* (27), 275703.

29.   Steward, P. A.; Hearn, J.; Wilkinson, M. C., An overview of polymer latex film formation and properties. *Adv. Colloid Interface Sci.* **2000,** *86* (3), 195-267.

30.   Kang, H.; Zuo, K.; Wang, Z.; Zhang, L.; Liu, L.; Guo, B., Using a green method to develop graphene oxide/elastomers nanocomposites with combination of high barrier and mechanical performance. *Compos. Sci. Technol.* **2014,** *92*, 1-8.

31.   Chang, K.-C.; Chen, S.-T.; Lin, H.-F.; Lin, C.-Y.; Huang, H.-H.; Yeh, J.-M.; Yu, Y.-H., Effect of Clay on the Corrosion Protection Efficiency of PMMA/Na+-MMT Clay Nanocomposite Coatings Evaluated by Electrochemical Measurements. *Eur. Polym. J.* **2008,** *44* (1), 13-23.

32.   Yilmaz, O., A hybrid polyacrylate/OMMT nanocomposite latex: Synthesis, characterization and its application as a coating binder. *Prog. Org. Coat.* **2014,** *77* (1), 110-117.

33.   Yilmaz, O.; Cheaburu, C. N.; Durraccio, D.; Gulumser, G.; Vasile, C., Preparation of stable acrylate/montmorillonite nanocomposite latex via in situ batch emulsion polymerization: Effect of clay types. *Appl. Clay Sci.* **2010,** *49* (3), 288-297.

34.   Tkalya, E.; Ghislandi, M.; Alekseev, A.; Koning, C.; Loos, J., Latex-based concept for the preparation of graphene-based polymer nanocomposites. *J. Mater. Chem.* **2010,** *20* (15), 3035-3039.

35.   Pham, V. H.; Dang, T. T.; Hur, S. H.; Kim, E. J.; Chung, J. S., Highly Conductive Poly(methyl methacrylate) (PMMA)-Reduced Graphene Oxide Composite Prepared by Self-Assembly of PMMA Latex and Graphene Oxide through Electrostatic Interaction. *ACS Appl. Mater. Interfaces* **2012,** *4* (5), 2630-2636.

36.   Yousefi, N.; Gudarzi, M. M.; Zheng, Q.; Aboutalebi, S. H.; Sharif, F.; Kim, J.-K., Self-alignment and high electrical conductivity of ultralarge graphene oxide– polyurethane nanocomposites. *J. Mater. Chem.* **2012,** *22* (25), 12709-12117.

37.   Lee, S. H.; Dreyer, D. R.; An, J.; Velamakanni, A.; Piner, R. D.; Park, S.; Zhu, Y.; Kim, S. O.; Bielawski, C. W.; Ruoff, R. S., Polymer Brushes via Controlled, Surface-Initiated Atom Transfer Radical Polymerization (ATRP) from Graphene Oxide. *Macromol. Rapid Commun.* **2010,** *31* (3), 281-288.

38.   Yoo, B. M.; Shin, H. J.; Yoon, H. W.; Park, H. B., Graphene and graphene oxide and their uses in barrier polymers. *J. Appl. Polym. Sci.* **2013,** *131* (1), 39628.

39.   Wicks, Z. J., F.; Pappas, S.; Wicks, D., *Organic Coatings: Science and Technology*. 3rd ed.; John Wiley & Sons: Hoboken, 2007.

40.   Wang, W.; Yu, Z.; Li, B.; Pan, Z., Seed Semicontinuous Emulsion Multi-Copolymerization of (Meth) Acrylates with High-Solid Content: Effect of The Operation Conditions. *Chin. J. Polym. Sci.* **1995,** *13* (2), 162-172.

41.   Cançado, L. G.; Jorio, A.; Ferreira, E. H. M.; Stavale, F.; Achete, C. A.; Capaz, R. B.; Moutinho, M. V. O.; Lombardo, A.; Kulmala, T. S.; Ferrari, A. C., Quantifying Defects in Graphene via Raman Spectroscopy at Different Excitation Energies. *Nano Lett.* **2011,** *11* (8), 3190-3196.

42.   Ferrari, A. C.; Robertson, J., Interpretation of Raman spectra of disordered and amorphous carbon. *Phys. Rev. B* **2000,** *61* (20), 14095-14107.

43.   Dikin, D. A.; Stankovich, S.; Zimney, E. J.; Piner, R. D.; Dommett, G. H. B.; Evmenenko, G.; Nguyen, S. T.; Ruoff, R. S., Preparation and characterization of graphene oxide paper. *Nature* **2007,** *448* (7152), 457-460.

44.   Tao, C.-a.; Wang, J.; Qin, S.; Lv, Y.; Long, Y.; Zhu, H.; Jiang, Z., Fabrication of pH-sensitive graphene oxide–drug supramolecular hydrogels as controlled release systems. *J. Mater. Chem.* **2012,** *22* (47), 24856.

45.   Zheng, J.; Liu, H.-T.; Wu, B.; Di, C.-A.; Guo, Y.-L.; Wu, T.; Yu, G.; Liu, Y.-Q.; Zhu, D.-B., Production of Graphite Chloride and Bromide Using Microwave Sparks. *Sci. Rep.* **2012,** *2*, 1-6.

46.   Chen, J.-T.; Fu, Y.-J.; An, Q.-F.; Lo, S.-C.; Huang, S.-H.; Hung, W.-S.; Hu, C.-C.; Lee, K.-R.; Lai, J.-Y., Tuning nanostructure of graphene oxide/polyelectrolyte LbL

assemblies by controlling pH of GO suspension to fabricate transparent and super gas barrier films. *Nanoscale* **2013,** *5* (19), 9081-9088.

47.   Kudin, K. N.; Ozbas, B.; Schniepp, H. C.; Prud'homme, R. K.; Aksay, I. A.; Car, R., Raman Spectra of Graphite Oxide and Functionalized Graphene Sheets. *Nano Lett.* **2008,** *8* (1), 36-41.

48.   Bai, H.; Li, C.; Wang, X.; Shi, G., On the Gelation of Graphene Oxide. *J. Phys. Chem. C* **2011,** *115* (13), 5545-5551.

49.   Bourgeat-Lami, E.; Faucheu, J.; Noel, A., Latex Routes to Graphene-Based Nanocomposites. *Polym. Chem.* **2015,** *6* (30), 5323-5357.

50.   Potts, J. R.; Dreyer, D. R.; Bielawski, C. W.; Ruoff, R. S., Graphene-based polymer nanocomposites. *Polymer* **2011,** *52* (1), 5-25.

51.   Yousefi, N.; Sun, X.; Lin, X.; Shen, X.; Jia, J.; Zhang, B.; Tang, B.; Chan, M.; Kim, J.-K., Highly Aligned Graphene/Polymer Nanocomposites with Excellent Dielectric Properties for High-Performance Electromagnetic Interference Shielding. *Adv. Mater.* **2014,** *26* (31), 5480-5487.

52.   Medhekar, N. V.; Ramasubramaniam, A.; Ruoff, R. S.; Shenoy, V. B., Hydrogen Bond Networks in Graphene Oxide Composite Paper: Structure and Mechanical Properties. *ACS Nano* **2010,** *4* (4), 2300-2306.

53.   Yu, Y.-H.; Lin, Y.-Y.; Lin, C.-H.; Chan, C.-C.; Huang, Y.-C., High-performance polystyrene/graphene-based nanocomposites with excellent anti-corrosion properties. *Polym. Chem.* **2014,** *5* (2), 535-550.

54.   Yang, Y.-H.; Bolling, L.; Priolo, M. A.; Grunlan, J. C., Super Gas Barrier and Selectivity of Graphene Oxide-Polymer Multilayer Thin Films. *Adv. Mater.* **2013,** *25* (4), 503-508.

55.   Chang, K.-C.; Ji, W.-F.; Lai, M.-C.; Hsiao, Y.-R.; Hsu, C.-H.; Chuang, T.-L.; Wei, Y.; Yeh, J.-M.; Liu, W.-R., Synergistic Effects of Hydrophobicity and Gas Barrier Properties on the Anticorrosion Property of PMMA Nanocomposite Coatings Embedded with Graphene Nanosheets. *Polym. Chem.* **2014,** *5* (3), 1049-1056.

56.   Huang, H.-D.; Ren, P.-G.; Chen, J.; Zhang, W.-Q.; Ji, X.; Li, Z.-M., High barrier graphene oxide nanosheet/poly(vinyl alcohol) nanocomposite films. *J. Membrane Sci.* **2012,** *409-410*, 156-163.

57.   Xing, W.; Tang, M.; Wu, J.; Huang, G.; Li, H.; Lei, Z.; Fu, X.; Li, H., Multifunctional properties of graphene/rubber nanocomposites fabricated by a modified latex compounding method. *Compos. Sci. Technol.* **2014,** *99*, 67-74.

58.   Mallakpour, S.; Abdolmaleki, A.; khalesi, Z.; Borandeh, S., Surface functionalization of GO, preparation and characterization of PVA/TRIS-GO nanocomposites. *Polymer* **2015,** *81*, 140-150.

CHAPTER III – FACILE FUNCTIONALIZATION OF GRAPHENE OXIDE VIA
LOW DENSITY AEROGEL PRECURSOR AND FABRICATION OF POLYMER-g-
GO NANOCOMPOSITES CORROSION PROTECTION COATINGS

Polymer nanocomposites containing two-dimensional (2D) nanomaterials
graphene oxide (GO) and reduced graphene oxide (rGO) show immense potential for
applications such as membrane separations, thin-film electronics, protective coatings, and
drug delivery because of their outstanding physiochemical properties. Facile and efficient
covalent-functionalizations of GO are desired for tuning the surface properties (i.e.
wettability) that permit extended applications and processing compatibility for fabricating
novel nanocomposites. Existing protocols have demonstrated successful covalent
functionalization of GO, however, those methods usually suffer from extended
ultrasonication, excess levels of reagents and reduced efficiency due to the diffusion
barriers resulting from poor miscibility of GO in most organic solvents. Attainment of
GO derivatives with well-defined structure and compositional homogeneity is
challenging, especially for reactions that use large molecules, e.g. polymer grafting.
Herein, we report a simple method of preparing well-defined GO derivatives from a low-
density aerogel precursor (LDGOAero) with increased surface area, that allows for
improved solvent accessibility. The protocol requires minimal ultrasonication and a small
amount of high boiling point cosolvents, such as dimethylformamide (DMF) and
dimethyl sulfoxide (DMSO). Moreover, the degree of modification can be easily adjusted
by varying the reagent/substrate ratio allowing the surface of GO derivatives to be tuned
for polar or non-polar solvent processing conditions. We also validated the capability of
fabricating polymer-*g*-GO nanocomposites through polymer grafting method using the

58

GO precursor. Thin-film coating was fabricated from a suspension of polyisobutylene grafted GO (PIB-*g*-GO) on low carbon steel, and it exhibited improved corrosion protection efficiency with measured corrosion rate ~50 times lower than that of unmodified GO.

3.1 Introduction

Graphene oxide (GO) is a two-dimensional (2D) carbon allotrope and building blocks with diverse applications in energy storage devices[1] and sensors[2], functional fibers[3], catalysis[4], filtration membranes[5], barrier and protective coatings,[6-7] and composites technologies[8] due to its unique physicochemical properties[9]. The potential utilization of GO can be extended through covalent and noncovalent functionalization via introduction of functional groups, which enables tuning its electronic, mechanical and surface properties.[10-11] For instance, chemically functionalized GO is often required to enhance solubility and processability for applications in polymer nanocomposites.[12-13] As a 2D macromolecule, many of its intrinsic properties, for example, electric/thermal conductivity, mechanical strength, barrier/permeation, and suspension/rheology behaviors, largely depend on its size stability (aspect ratio) and structural uniformity.[14-16] However, functionalization of GO by common methods[17] is generally limited by its poor dispersibility in most non-polar organic solvents[18], diminished reactivity, and the need for extensive ultrasonication and excess reagent(s)[19] that are required to overcome the diffusion barrier induced by stacked GO nanosheets.[20] Consequently, achieving structural homogeneity and stability of GO derivatives with reasonable cost-effectiveness is challenging, especially for polymer modifiers that suffer from low accessibility of functional groups on stacked GO nanosheets, leading to limited control and

59

productivity.[17] Therefore, a new strategy that provides better control, higher efficiency, and lower product inhomogeneity for synthesizing GO derivatives under more flexible reaction conditions (solvent choice) is highly desirable.

McGrail and coauthors reported that GO and rGO can be functionalized via Pinner reaction between hydroxyl groups (on the basal plane of GO and rGO) and nitriles under acidic aqueous conditions.[21] Although this method addressed the issue of GO dispersing by using water as a cosolvent in the reaction, it limits the modification reactions to be only on the basal plane that contains hydroxyl groups. Functionalization that endows GO and rGO with tailored solubility and functionality was demonstrated using small molecules and polymers with nitrile groups, however, use of highly toxic sodium cyanide compound for nitrilization is not desirable. Sierra and coauthors reported that by using a multi-step ultrasonication exfoliation procedure, size stability of GO platelet can be improved as compared with a continuous sonication procedure.[22] However, multi-step ultrasonication is not sufficient to disperse GO stacks in a reaction that requires non-polar solvent for dissolving the modifier(s), such as non-polar polymer.

Dong and coauthors reported the preparation of ultra-large GO by using chemically expanded graphite that turns a diffusion controlled reaction into a reactivity controlled oxidation procedure.[14] With pre-expanded graphite precursor, no physical agitation was applied during the oxidation reaction, and thus the lateral size of GO was well maintained with high exfoliation of GO nanosheets. This strategy can provide a solution for enabling highly efficient and regulated functionalization protocol of GO by using a designed pre-expanded precursor. GO nanosheets are highly exfoliated and stable in water due to a large number of hydroxyl and carboxylic acid functional groups.[23] Upon

60

drying, GO nanosheets collapse and form stacked layers via hydrogen bonding, π-π stacking, and electrostatic interactions when water molecules evaporate.[24]

Inspired by the pre-expanded graphite precursor, herein, we report the use of low density GO aerogel precursor (LDGOAero), which was prepared from dilute GO aqueous suspension via freeze-drying, as crucial preconditions for facile and scalable preparation of GO derivatives with well-defined structure and properties. Compared with traditional starting materials, three dimensional (3D) porous architecture of GO aerogel can provide large solvent-accessible surface areas.[25] Due to this porous structure, solvents (polar or nonpolar) can rapidly swell LDGOAero precursor to fully expose its reactive sites to functionalization reagents with minimal energy input (ultrasonication and mechanical stirring). LDGOAero can be easily redispersed in water to relatively loose GO platelet stacking by a small amount of ultrasonication or shaking, which makes it an ideal precursor for GO functionalization.

Numerous studies were conducted with ultra-thin graphene film, among which graphene-based coating(s) and additive(s) for metal protection have shown varying short- and long-term performances.[26-29] Corrosion protection property of GO was also investigated for different metals,[30-32] however, its intrinsic sensitivity towards water/moisture can be a problem for immersion or humid atmospheric corrosive environment(s).[33-34] The hydrophilicity of GO can be tuned by decreasing the hydrophilic moieties and attaching R-groups with minimal polar functionality to GO platelets.[35] Polyisobutylene, a saturated hydrocarbon elastomer with linear structure, is widely used in commercial products including fuel stabilizer, motor oil additive such as soot dispersants, packaging, and tack improvers in adhesives and biomedical applications.[36-39]

PIB-based synthetic rubber shows good thermal and oxidative stability, very low gas and moisture permeability, good chemical resistance, high flexibility and permanent tack properties.[39] Besides, covalent attachment of PIB onto a 2D nanomaterial, such as GO are rarely reported nor well-studied.[40] The PIB chains can facilitate GO dispersing in a non-polar solvent[21], thereby expand its compatibility for wider applications, such as solvent borne coatings.

In order to validate the synthetic strategy using our designed precursor (LDGOAero) and prepare GO derivatives with reduced water sensitivity, we conducted small molecule and polymer functionalization with hexanoyl chloride[17] and oligomeric amine-terminated polyisobutylene (PIB) (M_n = 4400 Da), respectively.[13, 41] Functionalized GO was thoroughly characterized by X-ray photoelectron spectroscopy (XPS), Fourier transform infrared spectroscopy (FTIR), Raman spectroscopy, and atomic force microscope (AFM). We found that this approach offers many advantages over existing GO modification methods, including flexibility to solvent selection, easy control on the degree of modification, scalability, and high grafting density of polymer. Covalently anchored PIB significantly improved the water barrier property of the resultant PIB-*g*-GO nanocomposite. Corrosion rate of cold rolled steel (CRS) substrates coated with pristine GO and PIB-*g*-GO (~2 µm), respectively, were measured to compare the protection effeciency.[30, 42]

This study addresses the limitation of existing approaches for GO modifications and offers opportunities for fabricating novel functional materials and nanocomposites.[43-44] The proof-of-concept study on polymer grafting demonstrates the capability for fabricating nanocomposites with high grafting density on GO.[45] Moreover, we verified

that the conductivity of the resultant GO derivatives can be recovered to an adequate level by a simple chemical reduction[46-47], which enables wider applications of these materials in sensor[48] and electronic fields.[49]

3.2 Experimental

3.2.1 Materials

All reagents were purchased from Sigma-Aldrich and used as received unless otherwise specified. Experiments and testing were conducted under ambient conditions unless noted. Reagents used for preparing GO and its derivatives included graphite (~150 µm), potassium permanganate (99% pure), phosphoric acid (85 wt%), sulfuric acid (95−98 wt %), hydrogen peroxide (30 vol %), hydrochloric acid (30−35 vol %), tetrahydrofuran (THF, 99.9% pure), N-methyl-2-pyrrolidone (NMP, 99.5% pure), hexanoyl chloride (97% pure), triethylamine (TEA, 99% pure), N,N'-Dicyclohexylcarbodiimide (DCC, 99% pure), Hydroiodic acid (HI, 55 vol %), acetic acid (97% pure), solvents EMPLURA® (acetone, ethyl alcohol, cyclohexane, chloroform, n-hexane, toluene) and in-house deionized (DI) water (Milli-Q, 18 MΩ).

3.2.2 Measurements and Instrumentation

FTIR spectra of GO and its derivatives were acquired using a Nicolet 6700 FTIR spectrometer in attenuated total reflectance (ATR) mode. Raman spectra were collected with a Thermo Scientific DXR Raman microscope with 633 nm excitation laser. XPS was performed on a Thermo Scientific K-Alpha X-ray spectrometer at a maximum background pressure of 2×10^{-9} mbar. Thin film samples were prepared by deposition on a silicon wafer and thoroughly dried in air. The software used for spectra analysis was CasaXPS and the quantification was expressed in relative atomic percentage with a

sensitivity of 0.5−1 atom %. XPS spectra of the carbon (C 1s), oxygen (O 1s), and nitrogen (N 1s) were fitted using a Gaussian-Lorentzian peak shape. UV absorption spectra were collected by a Lambda 35 ultraviolet–visible (UV–vis) spectrometer (PerkinElmer, Inc.) with a 326 nm UV lamp.

The dimensions of GO platelet and its derivatives were determined via AFM in tapping-mode with a SiC probe (1/T300 TM, Bruker). Samples for AFM analysis were prepared by drop-casting films from diluted (~0.0001 wt %) suspensions (solvent specified in the text). The morphology of stacked GO and GO-aerogels were studied using a ZEISS scanning electron microscope (MERLIN SEM) in high-vacuum mode. Samples were sputter-coated with silver before scanning. Thermogravimetric analysis (TGA) was acquired with a Q500 (TA Instruments) at 1 ℃/min ramping rate from room temperature to 600 ℃ in nitrogen atmosphere. Water vapor sorption was measured by using a Q5000 SA (TA Instruments) at 35 ℃ and 95% relative humidity (RH). Samples were equilibrated at 75 ℃ and 0% RH for 2 h before testing. Water contact angle (WCA) were acquired on thin film surface deposited on polished cold rolled steel (CRS) substrate using a Ramé-hart 200-00 Std.-Tilting B. goniometer with 4 μL water droplets. Rheological measurments were performed using a TA rheometer (AR G2) with a cone-plate geometry (60 mm, 2°) at 25 ℃.

3.2.3 Methylene Blue Surface Area Measurement[50-52]

UV-vis spectra of 0.01 mg/mL methylene blue (MB) aqueous solution was taken before and after 24 h as control. The same MB solution was added into vails with GO flake, and GO aerogels obtained from 1 and 10 mg/mL GO aqueous suspension, respectively. No mechanical stirring or ultrasonication was applied before or during the

adsorption test to preserve the pristine surface areas. The vails were kept still at ambient for 24 h to allow full adsorption of MB molecules in a box to avoid light. Then UV-vis spectra of the supernant from each vail were taken and analyzed. The surface area of GO and GO aerogels that covered by per milligram of MB was estimated to be 2.54 m^2.

3.2.4 Preparation of GO and LDGOAero

GO was synthesized as previously reported.[23,53] The resulting GO suspension was thoroughly purified and washed by centrifugation to remove residual ions. LDGOAero was prepared directly from the concentrated GO suspension without drying. The GO suspension was diluted with DI water to ~ 1 mg/mL, exhibiting a dark yellow color. The diluted suspension was then frozen with liquid nitrogen (−196 ℃) and freeze-dried to remove water without the collapse of the porous gel structure. Preparation of standard GO starting materials was conducted by drying the concentrated GO suspension in an oven operating at 50 ℃ for about 2 days. The resulting GO was weighted and dispersed in DI water to form a series of suspensions with different concentrations (0.01~20 mg/mL), which were used for the rheological study and aerogel fabrication for MB adsorption analysis.

3.2.5 Procedure for Hexanoyl Chloride Functionalization.

LDGOAero (1000 mg) was suspended in 225 mL of THF/NMP (8:1 v/v) in a 500 mL round bottom flask. The flask was then ultrasonicated (Fisher Scientific/FS9, 55W, 43 Hz) for a total of 10 min using two 5 min periods separated by a 1 min rest period to ensure thorough swelling of the precursor. In our experiments, we varied the degree of modification on GO by altering the reagent/LDGOAero mass ratio (r = wt./wt.), for which two separate experiments were conducted for the r = 3.85 and 9.65 mGOs using

hexanoyl chloride. Hexanoyl chloride (4 mL and 10 mL for the r = 3.85 and 9.65 cases, respectively) dissolved in 15 mL THF was added to the flask followed by TEA (3.8 mL and 9.5 mL, respectively) in 10 mL of THF under stirring using a magnetic stir bar (300 rpm). The reaction was kept at ambient for 10 h. The resultant mGOs were thoroughly washed with acetone, ethanol, and water in succession by high speed centrifugation, and dried in a forced air oven for 3 days at 40 ℃.

3.2.6 Procedure for PIB Oligomer Functionalization.

LDGOAero (750 mg) was loaded into a round bottom flask (500 mL) with a solvent mixture of THF (175 mL) and NMP (25 mL). The flask was ultrasonicated as described in the previous section to ensure full swelling of the precursor. Amino functional oligomeric PIB (a viscose liquid with Mn = 4400 Da, ~3 g) was dissolved in THF (40 mL) and added into the flask with stirring (300 rpm). DCC catalyst was dissolved in THF (10 mL) and added to the mixture. The reaction was maintained at ~65 ℃ for 6 h and then cooled to room temperature. The reaction products were thoroughly washed with THF and precipitated with ethanol. The precipitant was subjected to Soxhlet extraction with THF to remove unreacted PIB. The final products were collected and dried in an oven for 3 days at 40 ℃.

3.2.7 Procedure for Chemically Reduced GO and PIB-*g*-GO

GO and PIB-*g*-GO thin films were fabricated on a non-conductive polycarbonate substrate and immersed in acetic acid/DI water (1:1 v/v, 8 mL) solution containing 1 mL of hydroiodic acid (HI 55% in H_2O). The mixture was heated to 80 °C and maintained for 60 min with magnetic stirring. The reaction was cooled to room temperature and the thin films were thoroughly rinsed with water and dried in oven for 3 days at 40 ℃.

3.2.8 Coating Application and Electrochemical Measurements

In a typical procedure, a homogeneous suspension (0.5 mg/mL) of PIB-*g*-GO in cyclohexane was prepared by 3 min of ultrasonication for 5 times in water bath (ambient). CRS panels (compositional parameters summarized in Table B.1) were sanded using #220, 400, 600, 800, and 1200 sanding paper and cleaned thoroughly with acetone. PIB-*g*-GO coating was drop cast on pretreated CRS with thickness ranging from ~50 nm to ~2 µm. The coated panels were then dried at 70 °C for 2 days and fully cooled before conducting any tests.

Electrochemical corrosion test was performed in 3.5 wt.% NaCl solution by using a three-electrode flat cell equipped with a platinum mesh counter electrode and a Ag/AgCl reference electrode. The sample panel attached to the cell with an electrolyte exposure area of ~1 cm^2 that performs as the working electrode. Potentiodynamic polarization curves (Tafel plots) and electrochemical impedance spectroscopy (EIS) data were acquired on a VersaSTAT4 (Princeton Applied Research) workstation after the sample being stabilized for ~30−60 min at ambient. Polarization curves were measured at a scan rate of 1 mV/s from cathodic to anodic direction ±500 mV from open circuit potential (OCP). EIS (potential static) were performed in the frequency range of 100 kHz~10 mHz with ±10 mV amplitude. Corrosion rate and inhibiting efficiency were calculated, and the impedance data were simulated with equivalent circuit models using a Zview® software.
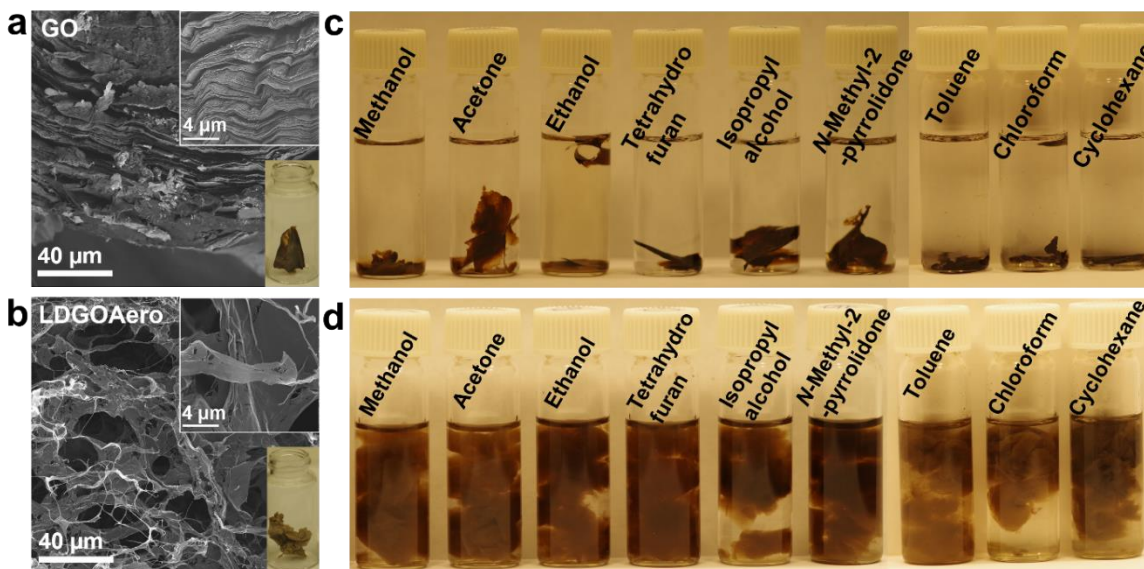
Figure 3.1 SEM images of (a) GO, (b) LDGOAero, and Digital images of suspensions of (c) GO and (d) LDGOAero in various organic solvents without ultrasonication or mechanical stirring.

3.3 Results and Discussion

3.3.1 GO Aqueous Suspension and LDGOAero Preparation

The rheological behavior of GO aqueous dispersions has been studied to provide fundamental guidance for materials assembly at an atomic level through π–π stacking and hydrogen bonding interactions.[54] As a soft material with lamellar shape, GO exhibits unique properties between a rigid 2D material and a flexible 1D polymer.[55] GO dispersions exhibit unique viscoelastic behavior showing strong dependence on aspect ratio and concentration.[14, 54] GO dispersions with a concentration of 10 or 20 mg/mL reveal typical viscoelastic gel behavior (Figure B.1a), wherein storage modulus (G') is greater than loss modulus (G"). The digital images in Figure B.2 also indicate a solid-like behavior of GO suspension at 10 mg/mL. Under this circumstance, GO dispersions exhibit a nematic phase and GO monolayers are packed with long-range orientation due to high volume fraction.[54] Upon freeze-drying that removes water from the system, the

closely-packed monolayers will assemble through π–π stacking and hydrogen bonding interactions to form walls in the aerogel pore cells as shown in Figure B.3a and B.3f. This cell wall with several layers of GO sheets enables the structural stability of resulting aerogel, which makes it difficult to be dispersed even into polar protic solvents including water (Figure B.4). GO suspension with a concentration around 5 mg/mL behaves like a viscoelastic soft solid that flows above yield stress, with G' still larger than G".[54] At this point, GO monolayers were trapped by their neighbors but no long-range positional order was exhibited.[54] The resulting aerogel (Figure B.3b and g) indicates relatively thinner cell wall with less strength (telling from their ability to sustain SEM electron beam), and the digital image in Figure B.4 reveals some dispersing in water at the applied condition. At low concentrations GO suspension exhibited a liquid-to-solid transitional state as shown in Figure B.1b, wherein G" is above G' at lower shear frequency and crossover at higher frequency.[54] This behavior indicates a critical condition whereby the monolayers can impart elasticity to the system by packing during shearing.[54] SEM images of resulting GO aerogels shown in Figure B.3c−e and Figure B.3h−j reveal large pore size and thin cell walls. Those aerogels give better dispersibility in water upon shaking and ultrasonication (Figure B.4) compared with GO aerogels obtained from 5 and 10 mg/mL suspensions. In this study, we found that GO aerogels can be obtained at a concentration as low as 0.3 mg/mL. However, from a cost-effective perspective, we chose 1 mg/mL GO suspension for making LDGOAero for the rest of the functionalization study.
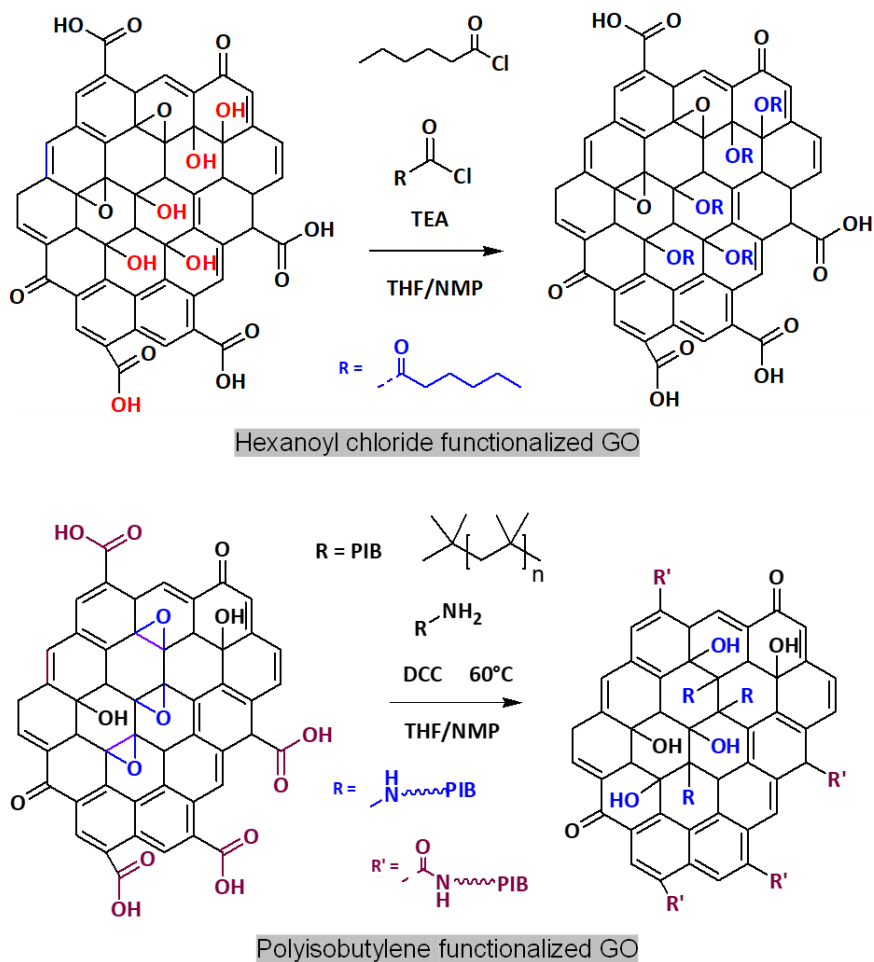
Figure 3.2 Synthetic route of hexanoyl chloride functionalized GO (named as mGO) and polyisobutylene functionalized GO (PIB-*g*-GO).

Figures 3.1a and b show SEM images of GO flake, the traditional starting material for synthesizing GO/rGO derivatives, and LDGOAero precursor used in this work. Digital photographs of their corresponding behavior in representative organic solvents are shown in Figures 3.1c and d. Without ultrasonication, most organic solvents cannot wet and penetrate GO flake due to low polarity that is insufficient for breaking π–π stacking and hydrogen bonding interactions between GO monolayers responsible for the formation of stacked morphology. Therefore, strong ultrasonication and polar solvents are usually required in order to produce sufficient mixing of GO sheets with the

70

modifiers.[18, 56] On the contrary, LDGOAero with an open-porous 3D architecture exhibits sufficient swelling in organic solvents without the need of ultrasonication or mechanical stirring, thereby enabling better solvent wetting and the potential for uniform functionalization of GO sheets.

Surface areas of LDGOAero and GO flake were determined using MB adsorption measurements in aqueous solution by UV-vis spectroscopy.[50] The absorbance intensity of MB in aqueous solution at 664 nm exhibited a linear relationship with concentrations, whereby a decrease of intensity resulted from physical adsorption of MB on GO surface.[50] Digital images of this process as shown in Figure B.5a indicate higher adsorption of aerogels compared to GO flake under the same condition without any mechanical stirring or ultrasonication. The accessible surface area under such circumstances was calculated to be ~171, 301, and 331 m^2/g for GO flake, GO aerogel obtained from 10 mg/mL suspension, and LDGOAero obtained from 1 mg/mL GO suspension, respectively (Figure B.5b−e). The surface area calculated from dilute GO aqueous suspension by Montes-Navajas and coworkers is ~736 m^2/g, much larger than the values we obtained here. However, it is not possible to achieve such a large surface area in organic solvents under actual reaction conditions when considering higher GO concentrations for cost-effectiveness. Therefore, by applying minimal ultrasonication we can ensure sufficiently larger accessible surface areas using LDGOAero compared to traditional GO flakes and achieve better control.

3.3.2 GO Functionalization and Characterizations
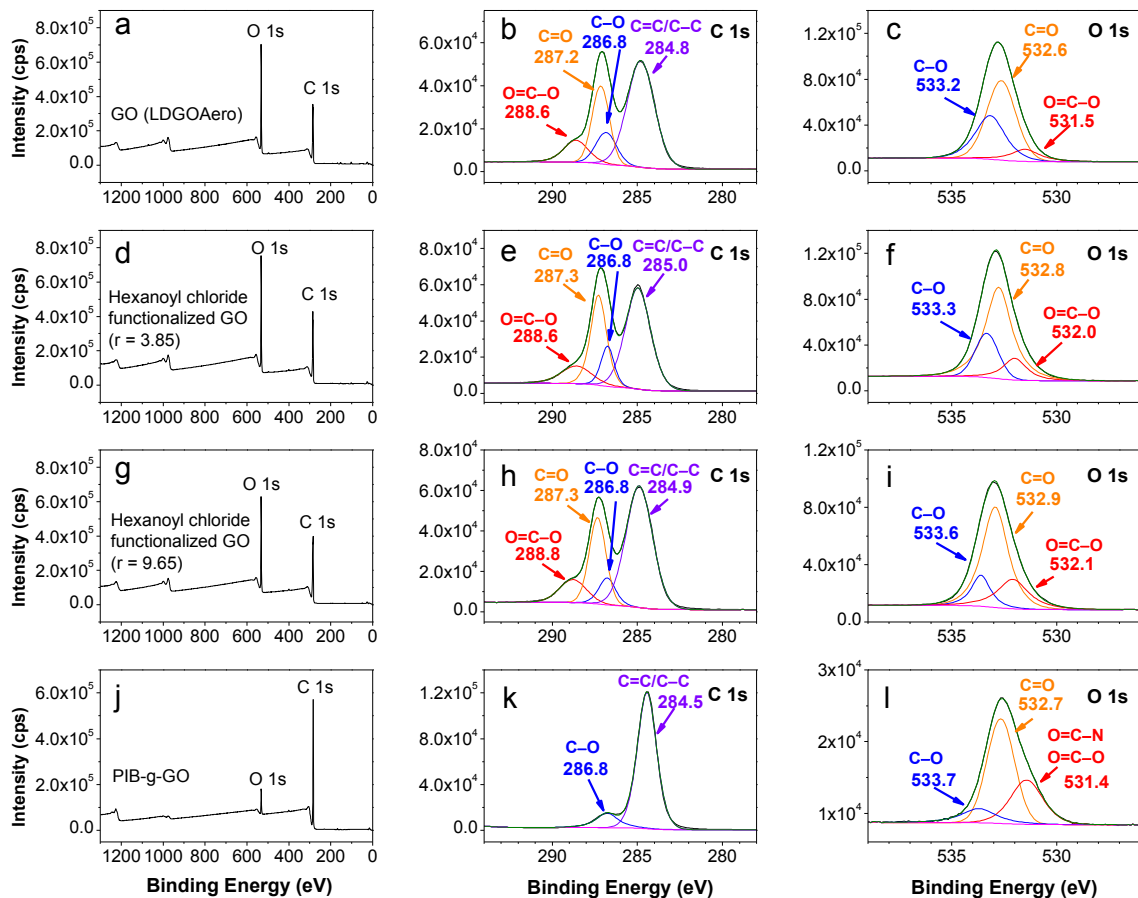
Figure 3.3 XPS spectra of (a) the survey scan, (b) C 1s and (c) O 1s high-resolution scans of GO (LDGOAero); XPS spectra of (d-i) the survey, C 1s and O 1s high-resolution scans of hexanoyl chloride functionalized GO (mGOs with r = 3.85 and 9.65, respectively); XPS spectra of (j-l) the survey, C 1s and O 1s high-resolution scans of PIB-*g*-GO.

Covalent functionalization(s) on GO was demonstrated (Figure 3.2) using hexanoyl chloride (a small molecule), and amino functional oligomeric polyisobutylene (PIB), respectively. Pristine and functionalized GO were characterized with XPS, FTIR, Raman spectroscopy, and AFM. The XPS spectra of GO, hexanoyl chloride functionalized GO (namely mGO), and GO functionalized with PIB (PIB-*g*-GO) are shown in Figure 3.3. The proportions of functional groups calculated by deconvoluting of C 1s and O 1s spectra are summarized in Tables B.2−B.9. Figure 3.3a−c show survey and

high-resolution C 1s and O 1s spectra of LDGOAero, respectively. The C 1s spectrum of LDGOAero (Figure 3.3b) was deconvoluted into four peaks corresponding to the following structures: sp^2 and sp^3 hybridized carbon (C=C/C–C, 284.8 eV), epoxy/hydroxyl (C–O, 286.8 eV), carbonyl (C=O, 287.2 eV), and carboxyl (O–C=O, 288.6 eV), with a carbon to oxygen atomic ratio (C/O) of 1.6.[30, 57] The O 1s spectrum in Figure 3.3c was deconvoluted into three peaks representing the oxygenated bonds: O=C–O (531.5 eV), C=O (532.6 eV), and O–C (533.2 eV).[53, 58]
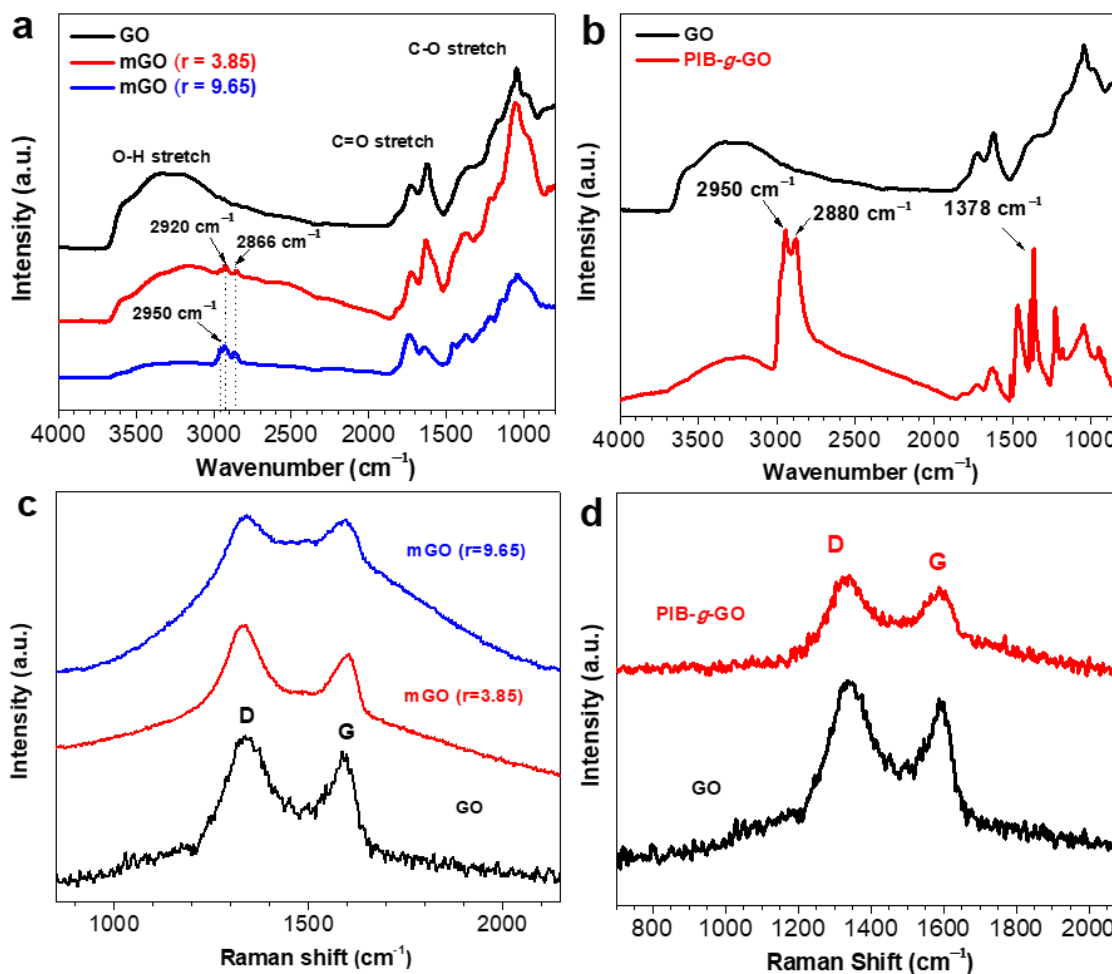
Figure 3.4 FTIR and Raman spectra of (a, c) the hexanoyl chloride functionalized mGOs (r = 3.85 and 9.63) and (b, d) PIB-*g*-GO.

Figure 3.3d–f show XPS survey and high-resolution C 1s and O 1s spectra of

mGO that was synthesized at lower modifier/GO mass ratio (r = 3.85). XPS survey and

high-resolution C 1s and O 1s spectra of mGO prepared at higher r value (r = 9.65) are

shown in Figure 3.3g–i. The C 1s spectra of mGOs are also deconvoluted into four

components: sp^2 and sp^3 carbon (C=C/C–C, ~284.9 eV), epoxy/hydroxyl (C–O, 286.8

eV), carbonyl (C=O, 287.3 eV), and carboxyl/ester (O–C=O, ~288.6 eV).[53] In this

modification reaction, hydroxyl groups on GO were reacted with chloride from hexanoyl

chloride, forming an ester linkage between GO and R group (C_6H_{10}). The C–O peak

intensity in C 1s spectra decreased while O–C=O peak increased for mGO due to the

modification reaction. The C/O atomic ratio also increased from 1.6 (GO) to 1.82 (mGO,

r = 3.85) and 2.14 (mGO, r = 9.65), respectively. The O 1s deconvoluted peaks of mGO

(Figure 3.3f and i) also displayed a decrease in O–C (~533.3 eV) peak intensity and an

increase in O=C–O (~532.0 eV), which validated successful functionalization on GO.

Additionally, the O–C=O functionality proportion of mGO (r = 9.65) is higher than that

of mGO (r = 3.85) as summarized in Tables B.3–4 and B.7–8.

Figure 3.3j–l show XPS survey and high-resolution C 1s and O 1s spectra for GO

with grafted PIB polymer. The survey spectrum of PIB-*g*-GO reveals a much higher C/O

atomic ratio (15.7) due to high carbon content in PIB and high grafting density that was

also validated by TGA. The C 1s spectrum of PIB-*g*-GO was deconvoluted into two

components: sp^3/sp^2 carbon (C–C/C=C, 284.5 eV), and epoxy/hydroxyl (C–O, 286.8 eV).

The O 1s spectrum (Figure 3.3l) was deconvoluted into O=C–O/N–C=O (531.4 eV),

C=O (532.7 eV), and C–O (533.7 eV). In addition, high-resolution N 1s spectrum is

shown in Figure B.6a with two deconvoluted peaks corresponding to amide N–C=O

74

(401.8 eV) and secondary amine N–C (399.7 eV) due to grafting reactions via the primary amine functionalities.[59] The content proportion of deconvoluted N 1s spectrum is summarized in Table B.10.
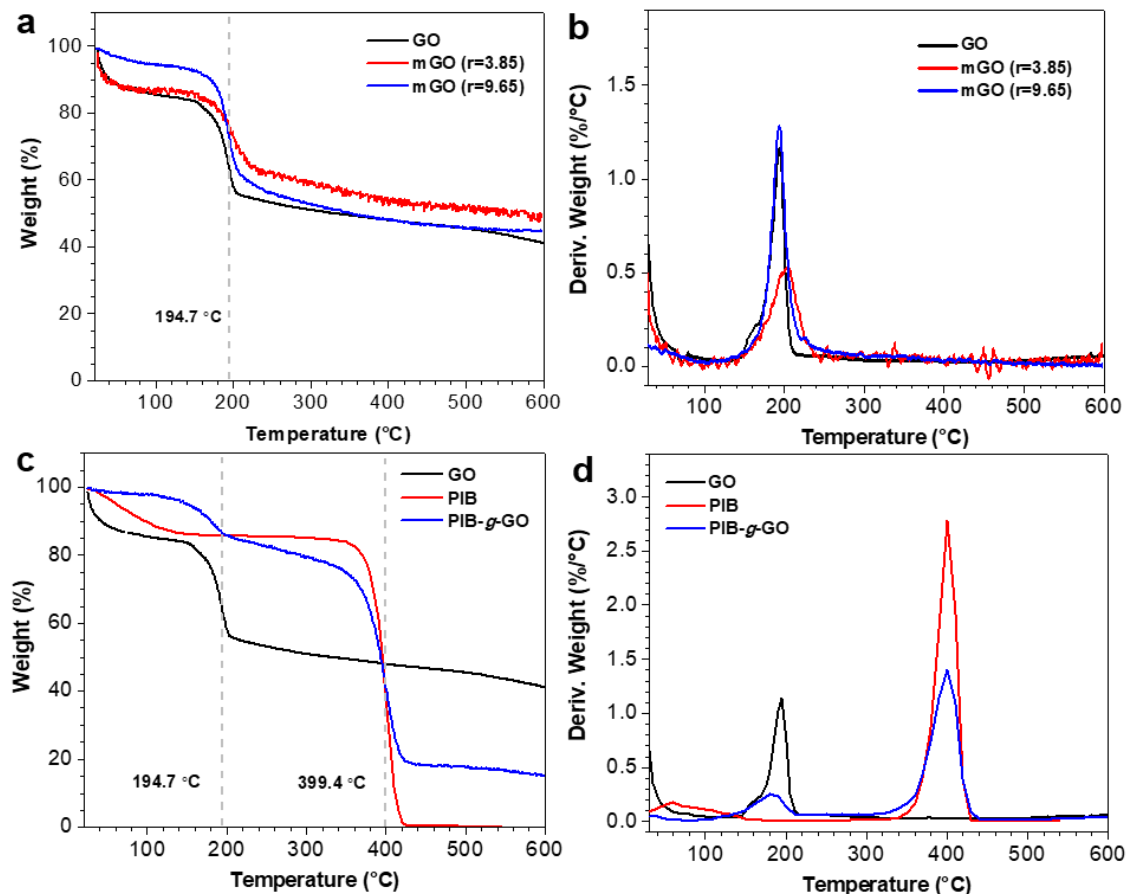
Figure 3.5 Degradation profiles and derivatives from TGA of (a, b) GO and the hexanoyl chloride functionalized mGOs (r = 3.85 and 9.63) and (c, d) GO, PIB oligomer, and PIB-*g*-GO.

The FTIR bands observed at ~3400, ~1750−1650, and ~1250−950 cm^{-1} in the spectrum (Figure 3.4a) of unmodified GO indicated the presence of hydroxyl, carboxylic acid/carbonyl, and epoxy functional groups.[23, 60] New bands at ~2950, 2920, and 2866 cm^{-1} in FTIR spectra (Figure 3.4a) of mGO (r = 3.85 and 9.65) were attributed to C–H stretching vibration in –CH$_3$ and –CH$_2$ groups from hexanoyl chloride

functionalization.[17] A pronounced reduction on the IR band (~3500−3000 cm^{-1}) representing −OH stretch can be observed for mGO (r = 9.65) due to the consumption of hydroxyl groups. Graphitic composition of GO and mGOs (r = 3.85 and 9.65) was characterized by Raman spectroscopy owing to high intensities of disordered graphite sp^2 carbon bonds in carbon materials.[61] The G (~1580−1600 cm^{-1}) and D (~1350 cm^{-1}) bands are typically observed on Raman spectra of chemically exfoliated GO and its derivatives.[23, 61] The former results from the first order scattering of the E$_{2g}$ phonon of in-plane vibrations of sp^2 bonded carbon atoms; the later stems from a defect-induced A$_{1g}$ breathing mode of sp^2 rings.[61-62] Peak intensity ratio of I$_D$/I$_G$ is applied to determine the degree of disorder, which is inversely proportional to the average size of sp^2 domains.[61-62] Raman spectra of GO and mGOs (r = 3.85 and 9.65) shown in Figure 3.4c indicated the presence of the G (~1590 cm^{-1}) and D (~1345 cm^{-1}) bands. The I$_D$/I$_G$ ratio calculated for GO (1.104) and mGOs (1.134 and 1.077) was quite close, implying that the modifications has minor impact on the scaffold structure.

Table 3.1 TGA analysis of GO, mGOs (r = 3.85 and 9.65) and PIB-*g*-GO

Sample	Mass loss (%) within temperature range (ºC)					
	RT−160	160−210	210−600	210−430	430−600	Char
GO	20%	25%	12%	−	−	43%
mGO (r = 3.85)	15%	19%	16%	−	−	50%
mGO (r = 9.65)	9%	30%	16%	−	−	45%
PIB	14%	0%	−	86%	−	0%
PIB-*g*-GO	6%	9%	−	66%	4%	15%

Covalent grafting of PIB onto GO platelet was also verified by FTIR and Raman spectra as shown in Figure 3.4b−d, respectively. The prominent peaks emerging at ~2933 cm^{-1} and ~2820 cm^{-1} on IR spectrum of PIB-g-GO correspond to the stretching vibrational mode of methyl and methylene groups of PIB segments.[40] The strong peak at ~1378 cm^{-1} is ascribed to dimethyl group on PIB chains.[63] The broadened bands arising from –NH, –OH, and –COOH are weaker in the spectrum of PIB-g-GO partially due to the shielding effect of PIB chains on the surface[64] and the consumption of functional groups in the grafting reactions. The I_D/I_G ratio calculated from the intensity of D and G bands on Raman spectra (Figure 3.4d) of PIB-g-GO was 1.088, which is also quite close to that of GO (1.104). Raman mapping images of D band on GO and PIB-g-GO film samples in an area of 500×500 µm^2 were also given in Figure B.7. Some heterogeneity of D band intensity can be observed for PIB-g-GO due to high coverage of PIB on carbon scaffold by functionalization that results in diminution of vibrational signals.[64]

Four-probe conductivity was collected on chemically reduced GO (rGO) and PIB-g-GO film samples which were drop-casted on polycarbonate sheets. The rGO sample exhibited high conductivity with a Rsq of ~137 Ω, and the R_{sq} of reduced PIB-g-GO is ~1589 Ω. Although the resistance of reduced PIB-g-GO is about one order of magnitude larger than that of rGO, it is sufficiently low enough for applications such as conductive coatings and sensors.[21] XPS spectra of reduced PIB-g-GO in Figure B.8 also indicated the reduction of oxygenated groups with an increased C/O ratio of 39.5 (the content proportions are summarized in Tables B.11−14).

AFM height images and profiles of exfoliated GO, mGO (r = 3.85 and 9.63), and PIB-g-GO indicating irregular lamellar shapes for GO and its derivatives (Figure B.8).

77

The exfoliated GO sheet (Figure B.8a–b) deposited from aqueous suspension resulted in a thickness of ~1.3 nm. This thickness is consistent with the values reported for exfoliated GO lamellae by similar preparation method.[24] Lamellae thickness for mGO (r = 3.85) (Figure B.8c–d) platelet was ~2.5 nm and ~3 nm for mGO (r = 9.65) (Figure B.8e–f) platelet. mGOs were deposited on silicon wafer from their ethanol suspensions. AFM height image and profile of PIB-*g*-GO that was drop-casted from its dilute cyclohexane suspension is shown in Figure B.8g–h. The average platelet thickness for PIB-*g*-GO was ~4 nm owing to polymer grafting with sheet size ranging from hundreds of nanometers to several micrometers.[21, 30, 40]

TGA plots (Figure 3.5) of GO, mGOs (r = 3.85 and 9.65), and PIB-*g*-GO depict the thermal degradation process, and the corresponding values are summarized in Table 3.1. Thermograms were collected under N_2 gas atmosphere with a heating rate of 1 ºC/min to avoid rapid expansion of GO, which can cause partial physical loss of materials from an open platinum pan.[65] Two steps were observed in the mass loss of GO, and mGOs (r = 3.85 and 9.65) in Figure 3.5a–b. Mass loss occurred during RT–160 ºC stage for GO, mGO (r = 3.85) and mGO (r = 9.65) is attributed to residual water or solvents from synthesis.[65] Above 160 ºC, a significant mass loss was observed on the TGA plots of GO and mGOs (a sharp slope between 160 and 210 ºC) due to thermal decomposition of unstable oxygenated functional groups on GO platelet.[57, 66] The mass loss between 210 and 600 ºC for GO and mGOs (r = 3.85 and 9.65) was also caused by thermal degradation of oxygenated moieties.[57]

TGA plots of oligomeric PIB and PIB-*g*-GO are displayed in Figure 3.5c–d, and analyzed to determine the grafting density of polymers per area (chains/nm^2).[67] PIB

oligomer alone exhibited a sharp mass loss (~86%) between 210 and 430 ℃, which is typical for polyolefin degradation via chain-scission reaction.[68] The mass loss (~14%) occurred between RT and 210 ℃ for PIB oligomer was due to residual solvents. The TGA curve for PIB-*g*-GO contains four steps: mass loss between RT and 160 ℃ was due to residual solvents and moisture; mass loss between 160 and 210 ℃ corresponded to the TGA curve of GO; mass loss between 210 and 430 ℃ was attributed to the decomposition of grafted PIB; mass loss between 430 and 600 ℃ resulted from thermal decomposition of oxygenated groups existing on GO. The residual mass at 600 ℃ was 0% for PIB oligomer and 15% for PIB-*g*-GO. The mass ratio (2.36) of grafted PIB chains (~66%) to GO (~28%) platelets was thus calculated from the thermal decomposing profile.

The grafting density can then be calculated through Eq. (1), where M_n is the number of the average molecular weight of PIB, N_A is Avogadro's constant, and A_{GO} is surface area of GO. The maximum grafting density was calculated to be 0.973 using the measured initial surface area of LDGOAero. The minimal grafting density calculated from dilute GO aqueous suspension by other researchers is 0.438.[50] The weight fraction of PIB in PIB-*g*-GO was determined to be 70.2% by TGA, indicating successful grafting reaction with high grafting density when using LDGOAero for making novel polymer nanocomposites.

$$\text{Grafting Density} \left(\frac{\text{chain}}{nm^2}\right) = \frac{N_A \times 10^{-18}}{M_n \times A_{GO}} \times \frac{wt_{PIB}}{wt_{GO}} \tag{1}$$

Figure 3.6 demonstrates the dispersibility of GO and its derivatives obtained from different functionalization in selected polar and nonpolar solvents.[18, 69] GO can form a stable suspension in water or polar solvent such as ethanol via ultrasonication, but not

into solvents with lower polarity as shown in Figure 3.6a. The reaction of hydroxyl

moieties with hexanoyl chloride results in the disruption of interlayer hydrogen bonding

and π–π stacking interactions. Solvent molecules access the alkane R group on the

platelet, resulting in improved dispersion of surface modified GO lamellae upon

ultrasonication (Figure 3.6b).[20-21, 64] Variation of the r value of mGO exhibited an impact

on the dispersibility of mGOs within selected solvents that shows different polarity

(solvent polarity was summarized in Table B.15). For example, mGO (r = 3.85) can be

dispersed into water by ultrasonication, while mGO (r = 9.65) is not. On the contrary,

mGO (r = 9.65) forms stable suspension in chloroform via ultrasonication, but mGO (r =

3.85) is only slightly dispersed under the same condition. This indicated that solvent

property of GO can be altered by varying the degree of modification using hydrophobic

conjugant. Therefore, mGO with lower r value displayed increased dispersibility within

organic solvents and maintained some water dispersible property. However, for a non-

polar solvent such as toluene, hexanoyl chloride functionalization is not sufficient to aid

in the dispersion of platelet even at higher r value. GO derivatives with grafted polymers

were reported to be able to disperse in non-polar solvents such as methylene chloride, n-

hexane, and toluene.[21, 30, 40] Grafting of PIB resulted in stable suspensions in several non-

polar solvents via small ultrasonication (15 min) as shown in Figure 3.6c. Figure 3.6d

also depicts the solvent interaction of GO and PIB-*g*-GO within a non-miscible solvent

system of water and cyclohexane.
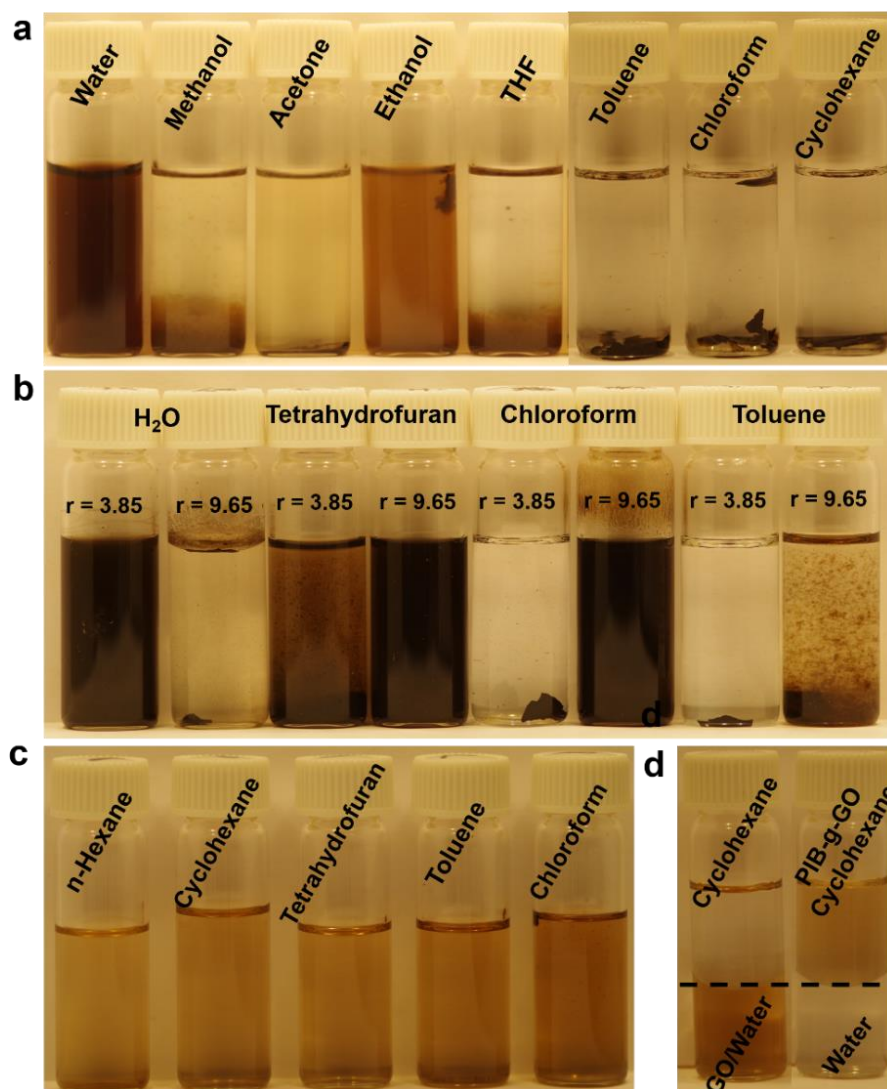
Figure 3.6 (a) Suspensions of GO in selected solvents after 1 h of ultrasonication; (b) suspensions of the hexanoyl chloride functionalized GO (r = 3.85 and 9.65) in selected solvents; (c) suspension of PIB-*g*-GO in selected non-polar solvents, (d) GO and PIB-*g*-GO's solvent property.

One of the most established methods for studying surface property of materials is contact angle measurement, which was performed on thin film samples applied on a CRS substrate as shown in Figure 3.7a and b.[70] Water contact angle (WCA) measured for bare CRS substrate (polished) was ~54.8 ± 0.5°, indicating a hydrophilic surface. WCA measured for GO thin films (~50 nm and ~2 µm) applied on CRS substrate showed minor

difference (53.9 ± 0.4° and 51.9 ± 0.3°, respectively), which was attributed to the hydrophilic nature of GO. Hexanoyl chloride functionalized GO exhibited increasing WCA, 58.1 ± 0.5° and 62.8 ± 0.4° for mGOs (r = 3.85 and 9.65), respectively. This result indicated that wetting property of GO platelet can be adjusted by hydrophobic R groups obtained from surface modification, which is in agreement with solvent dispersing property (Figure 3.6). Figure 3.7b shows WCA measured for PIB-*g*-GO coated CRS substrate with varying film thickness (~50 nm–2 µm). A significant increase (by ~40°) can be observed on PIB-*g*-GO samples regardless of film thickness, exhibiting a hydrophobic surface (WCA > 90°) that resulted from high coverage of hydrophobic PIB chains.

As a companion characterization to contact angle measurement, water vapor sorption (Figure 3.7c) was conducted to determine the interaction between moisture and hydrophilic moieties on GO and its derivatives.[71] Vapor sorption of LDGOAero (61%) is about two-fold higher than that of pristine GO (33%), and is in correlation with the accessible surface area measured from MB experiments. Water uptake for mGO (r = 3.85) decreases slightly compared to GO due to lower r value. Additional decrease can be observed for mGO (r = 9.65), which is about half of the uptake value of GO. Water uptake for PIB grafted GO demonstrated an ~85% decrease from pristine GO, however, this ~5% sorption value indicates that some hydrophilic oxygen-containing moieties are still available to interact with water during long-term exposure to high humidity conditions. These results corroborate the smaller mass loss of mGO (r = 9.65) and PIB-*g*-GO on TGA plots between RT and 100 °C due to moisture adsorption from the air.
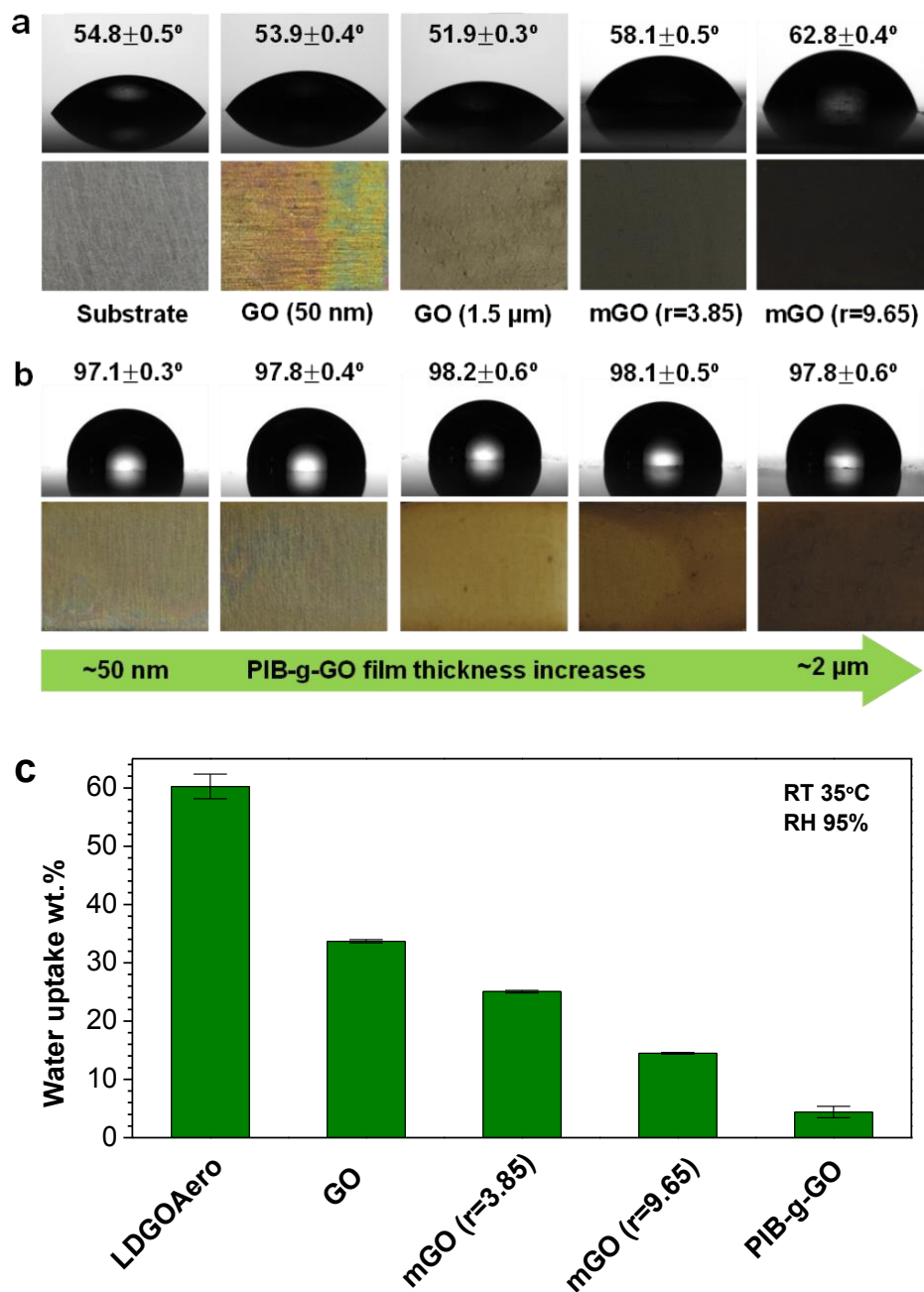
Figure 3.7 Water contact angle of (a) bare CRS substrate, CRS coated with GO, hexanoyl chloride functionalized GO, mGOs (r = 3.85 and 9.65); (b) CRS coated with PIB-*g*-GO of varying thickness (~50 nm to ~2 µm); (c) water vapor sorption of LDGOAero, GO flake, mGOs (r = 3.85 and 9.65) and PIB-*g*-GO.

3.3.3 Electrochemical Study on PIB-*g*-GO Nanocomposite Coatings
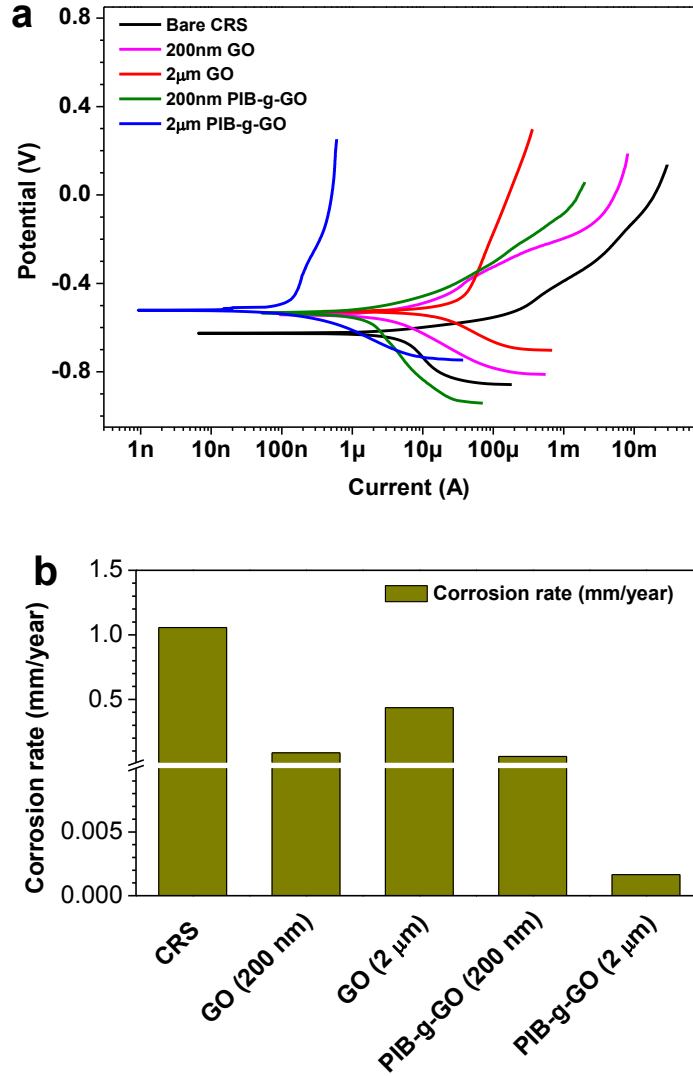
Figure 3.8 (a) Tafel plots and (b) corrosion rates of bare metal, PIB-*g*-GO and GO coated CRS in 3.5 wt.% NaCl solution immersion.

The characterization of hydrophobic/hydrophilic properties is important for the relative solubility, water management, and degree of modification. However, the ultimate proof of value comes from functional performance based testing such as EIS. Aqueous corrosion occurs on steel when it is submerged into an electrolyte solution due to redox reaction between iron and oxygen.[72] The redox reaction for steel corrosion consists of two partial reactions, also known as half reactions (given below).

$$\text{Fe} \rightarrow \text{Fe}^{2+} + 2\text{e}^- \qquad\qquad \text{Anodic reaction}$$

$$\text{O}_2 + 2\text{H}_2\text{O} + 4\text{e}^- \rightarrow 4\text{OH}^- \qquad \text{Cathodic reaction}$$
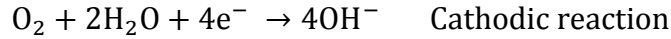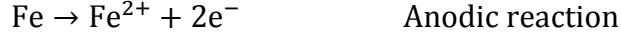
The anodic reaction of metal dissolution is controlled by charge transfer process, while cathodic reduction reaction is affected by many factors including oxygen dissolution.[72] Tafel analysis was used to quantify corrosion rates (CR) on bare and coated CRS with GO and PIB-*g*-GO films immersed in 3.5% NaCl solution.[26, 30] Because this is a kinetically controlled electrochemical reaction and obeys the Butler-Volmer equation (which reveals an exponential dependence of current to the deviation of over voltage value), by measuring and plotting the logarithm of the current density (*i*) *vs* the electrode potential (*E*), the reaction kinetic parameters can be extrapolated.[73] The equilibrium corrosion potential (E_{corr}) and corrosion current density i_{corr} is determined from Tafel plots (as specified in Figure B.10) and corrosion rate (CR) can be calculated accordingly by Faraday's Law.[72] Eq. (2) is applied to calculate CR: where the CR constant K is 3272 mm/year; the equivalent weight (EW) and density of iron (Fe) is 27.9 g and 7.872 g/cm^3, respectively; and the electrode surface area (A) is 1 cm^2.[26, 72] Tafel plots for all systems are displayed in Figure 3.8a and the corresponding CR values are shown in Figure 3.8b. The protection efficiency can be determined from the corrosion current density measured on bare (i_{corr}) and coated (i'_{corr}) steel through Eq. (3).[30] The parameters obtained from Tafel analysis are summarized in Table 3.2.

$$CR = \frac{i_{corr} \times K \times EW}{\rho A} \qquad\qquad (2)$$

$$\eta = 1 - \frac{i'_{corr}}{i_{corr}} \qquad\qquad (3)$$

Table 3.2 Electrochemical parameters summarized for Tafel analysis.

Sample	E_{corr}	I_{corr}	CR	η
	(mV)	($\mu A/cm^2$)	(mm/year)	(%)
Bare CRS	−628.6	91.07	1.057	−
GO (200 nm)	−548.3	7.498	0.087	91.7
GO (2 µm)	−522.8	37.58	0.436	58.7
PIB-*g*-GO (200 nm)	−532.8	5.045	0.058	94.4
PIB-*g*-GO (2 µm)	−518.5	0.1421	0.0016	99.8

The corrosion potential of CRS in 3.5% NaCl solution is −628.6 mV (vs SCE) and shifts positively (up to ~ 518.5 mV) when coated with GO or PIB-*g*-GO thin films. The corrosion current density of CRS was 91.07 $\mu A/cm^2$, and the corresponding rate was ~1.057 mm/year, meaning that a layer of 1.057 mm thick steel on 1 cm^2 area will be eroded due to uniform corrosion under such an immersion condition every year.[72] For CRS coated with ~200 nm thick GO or PIB-*g*-GO films, corrosion current density decreased to ~7.5 and 5.0 $\mu A/cm^2$, respectively. However, increasing the thickness of GO coating does not improve coating protection effect and corrosion current density is ~37.58 $\mu A/cm^2$. One reason could be that thicker GO film shows poor adhesion to steel substrate due to film-formation from high-concentration GO aqueous suspension, as shown from cross-sectional SEM image in Figure B.11a. In contrast, a prominent decrease of corrosion current density is observed for PIB-*g*-GO coated CRS with increased thickness (~2 µm), and the calculated protection efficiency was 99.8%. PIB-*g*-

GO films exhibit tacky adhesion to substrate (Figure B.11b), that may confer corrosion protection in addition to inhibiting diffusion of water (and ions) to substrate due to the presence of the flexible, hydrophobic PIB chain (Figure 3.9). Figure B.12 demonstrates the time dependence of protection by PIB-*g*-GO films (~1.5 µm) under the same immersion condition, indicating a decreased protection efficiency of ~0.8% after 144 h.
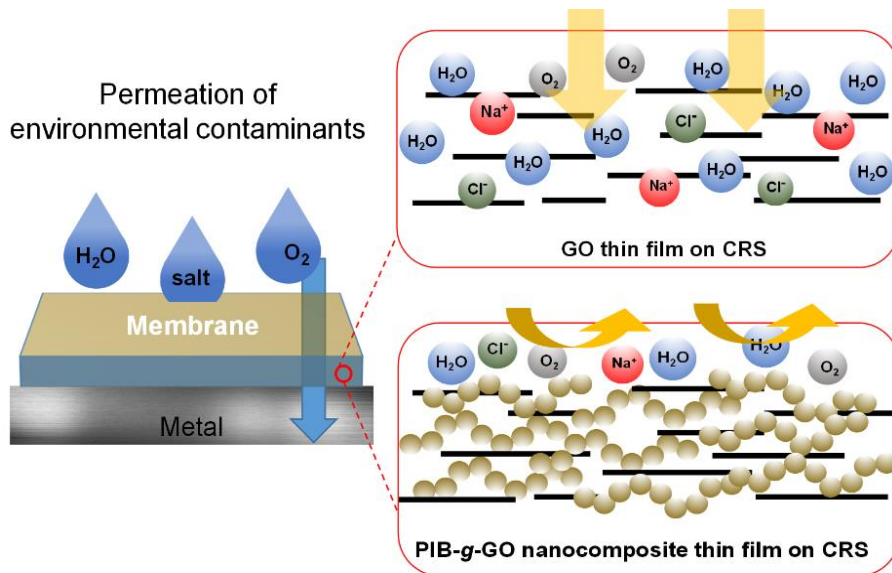
Figure 3.9 Schematic representation of GO and PIB-*g*-GO thin film as a better barrier layer for corrosion protection on metal substrate under salt immersion condition.

EIS measurement is an in-situ and non-destructive technique usually applied to study corrosion resistance of coated or bare metals under immersion conditions.[74] In potentiostatic EIS, a small sinusoidal perturbation of voltage is applied to the system and a sinusoidal current is induced with a phase shift (phase angle) with respect to the potential.[72] The impedance Z is recorded as a function of frequency ω containing two parts, real (Z_{re}) and imaginary (Z_{im}) impedance which arises from resistance and capacitance/inductance elements in the system, respectively. With equations of model equivalent circuit that describes the electrochemical system, it is possible to calculate the

impedance as a function of frequency, thereby simulating the data from experimental

impedances that leads to the confirmation or rejection of the model.[72, 74]
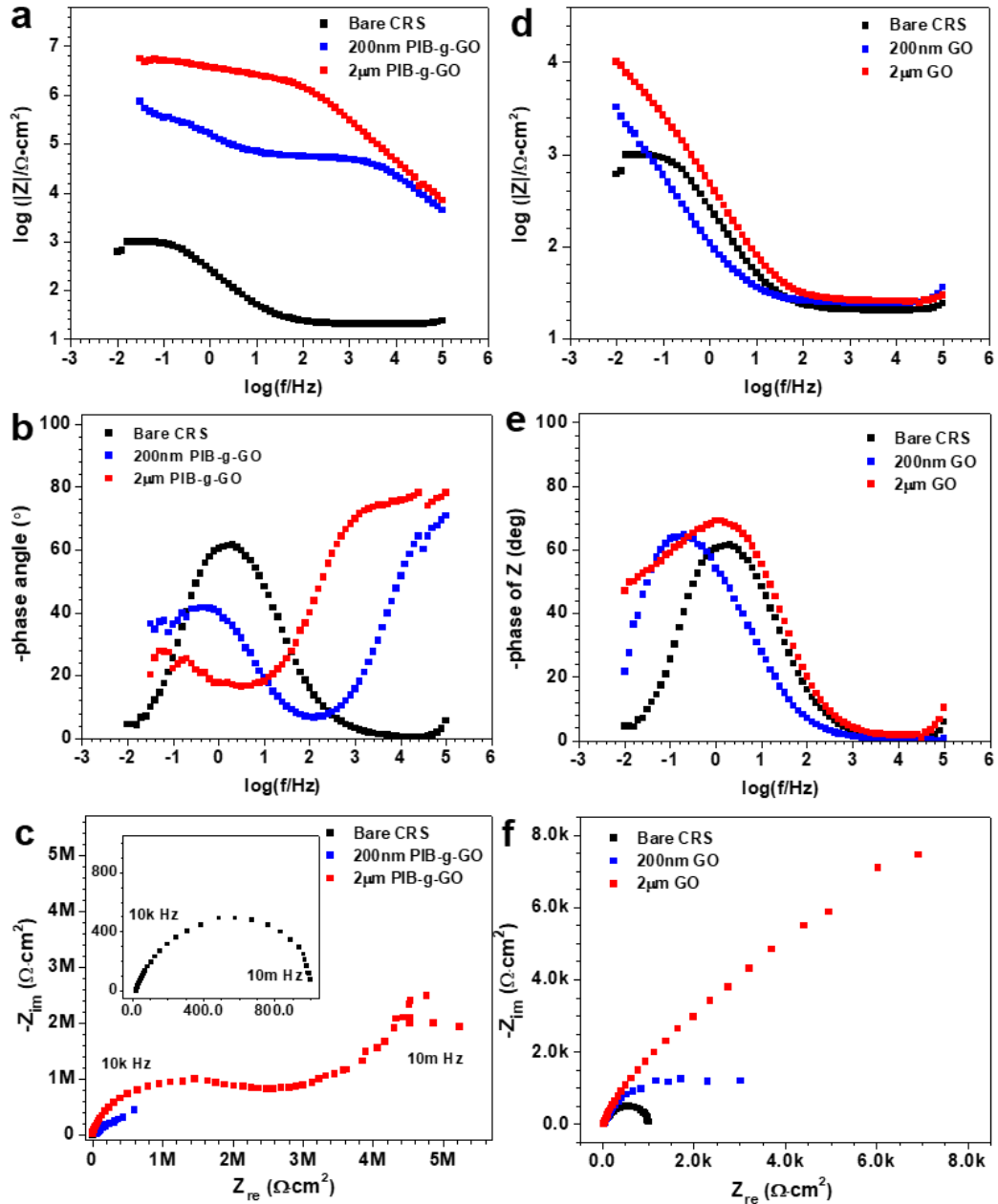
Figure 3.10 EIS Bode modulus (a, d), Bode phase (b, e), and Nyquist (c, f) plots of bare and coated CRS with PIB-*g*-GO (a−c) and GO (d−f), respectively.

The modulus of impedance ($|Z|$) at low frequencies is employed to measure the

resistance of the coating system towards water/electrolyte solution.[75] Figure 3.10a and d

show Bode plots (log $|Z|$ vs log ω) of bare and coated CRS with PIB-*g*-GO and GO thin films, respectively. The impedance for bare CRS at the low frequency region is $\sim 10^3$ Ω/cm^2. The CRS coated with GO exhibits slightly increased impedance values up to $\sim 10^4$ Ω/cm^2. PIB-*g*-GO coated samples displayed that the impedance increased to $\sim 10^7$ Ω/cm^2 (for ~ 2 μm film), which is a significant increase over that of GO coating. Bode phase plots ($-$phase angle *vs* log ω) of all systems shown in Figure 3.10b and e. In general, the total impedance at high frequencies ($10^4 \sim 10^5$ Hz) is attributed to the charge transfer resistance (in metal corrosion); the impedance at medium frequencies ($10^0 \sim 10^3$ Hz) is related to coating defects; the impedance at low frequency region ($10^{-2} \sim 10^0$ Hz) is governed by the dielectric property of a barrier coating (capacitance).[13, 42] Therefore, the corrosion resistance property of a coating is correlated with this barrier effect towards water and electrolyte solution.
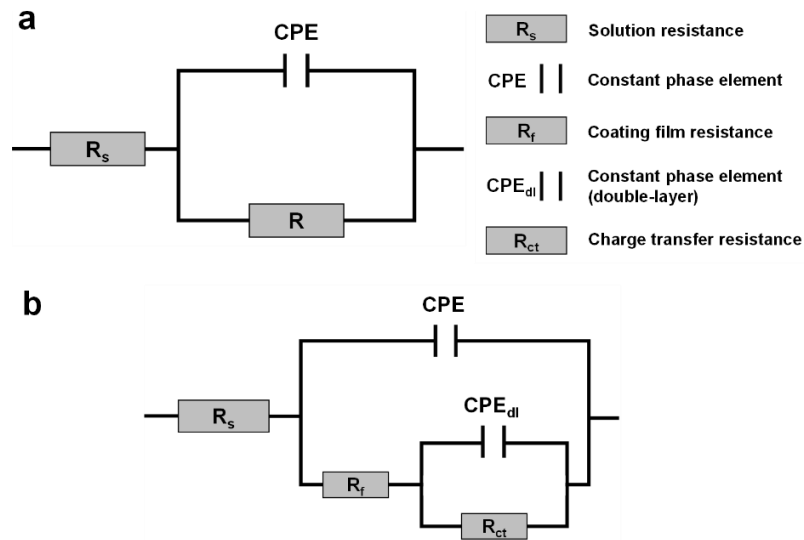
Figure 3.11 Equivalent circuits for fitting (a) one time-constant and (b) two time-constant impedance.

Bode phase plots ($-$phase angle *vs* log ω) of all systems are shown in Figure 3.10b and e. Generally, a peak that appeared at high frequencies ($10^4 \sim 10^5$ Hz) was assigned to

89

the responses of coating (capacitance), a peak located at medium frequencies (10^0 ~10^3 Hz) was the responses of coating defects, and a peak in low frequency region (10^{-2} ~10^0 Hz) could be attributed to metal corrosion (charge transfer resistance).[13, 42] A single peak on the Bode phase plot around 10^0 Hz was observed for bare and GO coated CRS corresponds to the corrosion of iron. PIB-*g*-GO coated CRS differ markedly showing two peaks on the Bode phase plot.

Table 3.3 Electrochemical parameters for EIS.

Sample	Q_0 (CPE$_f$) (S·sec^n/cm^2)	n (CPE$_f$)	R_f (Ω/cm^2)	Q_0 (CPE$_{dl}$) (S·sec^n/cm^2)	n (CPE$_f$)	R_{ct} (Ω/cm^2)
Bare CRS	–	–	–	7.6×10^{-4}	0.84	1.1×10^3
GO (200 nm)	–	–	–	1.6×10^{-3}	0.81	3.2×10^3
GO (2 µm)	–	–	–	1.7×10^{-3}	0.79	3.4×10^3
PIB-*g*-GO (200 nm)	3.5×10^{-9}	0.83	5.2×10^4	2.8×10^{-6}	0.61	1.3×10^6
PIB-*g*-GO (2 µm)	2.0×10^{-9}	0.84	2.5×10^6	2.6×10^{-7}	0.59	7.2×10^6

The Nyquist plots (Z_{re} *vs* Z_{im}) that depicted real and imaginary parts of the total impedance values are shown in Figure 3.10c and f. Bare CRS shows a typical resistance semicircle that represents resistivity of metal electrode.[76] CRS coated with GO films shows similar hemicircles but with larger diameters, indicating increased resistivity.[77] The flattened semicircle that differs from bare metal is due to diffusion at electrode interface resulting from GO deposition.[78] PIB-*g*-GO coated CRS exhibits an initial arch followed with a tail, also indicating ion diffusion at the electrode.[79] Impedance data were analyzed by simulation with equivalent circuit models as shown in Figure 3.11. A one-

time constant model (Figure 3.11a) was used for bare and GO coated CRS samples, and a two-time constant model (Figure 3.11b) was applied for PIB-*g*-GO coated CRS.[30, 33, 80]

In the equivalent circuits shown in Figure 3.11: R_s accounts for solution resistance; R_f represents coating film resistance; a constant phase element (CPE) was used instead of a capacitor due to heterogeneity on the metal substrate and in the coating films especially when immersed in aggressive electrolyte solution. The impedance value of a CPE was determined by two parameters Q_0 and n with the expression of $Z=(1/Q_0)\times(\omega \cdot i)^{-n}$, where n value refers to the heterogeneity ranging from 0~1, and Q_0 will be an equivalent to a simple capacitor when n is 1. Additionally, in this circuit: CPE_f represents the capacitance behavior of coating films; CPE_{dl} represents electric double-layer capacitance; and R_{ct} is charge transfer resistance.[81] The values of the equivalent circuit elements for each sample were obtained by data fitting and are listed in Table 3.3. Charge transfer resistance for GO coated CRS increased, but less than that of PIB-*g*-GO coated samples. One explanation for this difference could be the increased surface hydrophobicity due to polymer grafting improved the coating resistance towards the electrolyte solution. Corrosion resistance of the PIB-*g*-GO coating on CRS also increased with increasing film thickness, while double-layer capacitance decreased slightly.

3.4 Conclusions

In summary, we report a simple method of preparing well-defined GO derivatives using a low-density aerogel precursor (LDGOAero) with increased surface area, which allows for improved access of small and large functionalization molecules to GO platelet in various solvents systems. This protocol requires minimal ultrasonication and a small amount of high boiling point co-solvents (such as DMF, DMSO, or NMP). Furthermore,

91

the degree of modification can be easily tuned by varying the reagent/substrate ratio so

that suspension property of GO derivatives can be adapted for different processing

conditions (i.e. polar or non-polar solvents). We also validated the capability of

fabricating polymer-*g*-GO nanocomposites directly via this functionalization method by

polymer grafting. Ultra-thin coatings were fabricated from suspension of polyisobutylene

grafted GO (PIB-*g*-GO) on low carbon steel and tested for their corrosion protection

property. The corrosion rate of low carbon steel immersed in electrolyte solution

decreased by 99.8% when a layer of ~2 µm of this nanocomposite coating was applied.

3.5 Reference

1.   Raccichini, R.; Varzi, A.; Passerini, S.; Scrosati, B., The role of graphene for electrochemical energy storage. *Nat Mater* **2015,** *14* (3), 271-9.
2.   Urbanova, V.; Hola, K.; Bourlinos, A. B.; Cepe, K.; Ambrosi, A.; Loo, A. H.; Pumera, M.; Karlicky, F.; Otyepka, M.; Zboril, R., Thiofluorographene-hydrophilic graphene derivative with semiconducting and genosensing properties. *Adv Mater* **2015,** *27* (14), 2305-10.
3.   Xin, G.; Yao, T.; Sun, H.; Scott, S. M.; Shao, D.; Wang, G.; Lian, J., Highly thermally conductive and mechanically strong graphene fibers. *Science (New York, N.Y.)* **2015,** *349* (6252), 1083-7.
4.   Liang, Y.; Li, Y.; Wang, H.; Zhou, J.; Wang, J.; Regier, T.; Dai, H., Co(3)O(4) nanocrystals on graphene as a synergistic catalyst for oxygen reduction reaction. *Nat Mater* **2011,** *10* (10), 780-6.
5.   Akbari, A.; Sheath, P.; Martin, S. T.; Shinde, D. B.; Shaibani, M.; Banerjee, P. C.; Tkacz, R.; Bhattacharyya, D.; Majumder, M., Large-area graphene-based nanofiltration membranes by shear alignment of discotic nematic liquid crystals of graphene oxide. *Nature Communication* **2016,** *7*, 10891.
6.   Su, Y.; Kravets, V. G.; Wong, S. L.; Waters, J.; Geim, A. K.; Nair, R. R., Impermeable barrier films and protective coatings based on reduced graphene oxide. *Nature Communication* **2014,** *5*, 4843.
7.   Novoselov, K. S.; Falko, V. I.; Colombo, L.; Gellert, P. R.; Schwab, M. G.; Kim, K., A roadmap for graphene. *Nature* **2012,** *490* (7419), 192-200.
8.   Potts, J. R.; Dreyer, D. R.; Bielawski, C. W.; Ruoff, R. S., Graphene-based polymer nanocomposites. *Polymer* **2011,** *52* (1), 5-25.
9.   Geim, A. K.; Novoselov, K. S., The rise of graphene. *Nat Mater* **2007,** *6* (3), 183-191.
10.   Dreyer, D. R.; Park, S.; Bielawski, C. W.; Ruoff, R. S., The chemistry of graphene oxide. *Chemical Society Reviews* **2010,** *39* (1), 228-240.

11.   Chen, D.; Feng, H.; Li, J., Graphene oxide: preparation, functionalization, and electrochemical applications. *Chem Rev* **2012,** *112* (11), 6027-53.

12.   Compton, O. C.; Kim, S.; Pierre, C.; Torkelson, J. M.; Nguyen, S. T., Crumpled Graphene Nanosheets as Highly Effective Barrier Property Enhancers. *Advanced Materials* **2010,** *22* (42), 4759-4763.

13.   Sun, W.; Wang, L.; Wu, T.; Wang, M.; Yang, Z.; Pan, Y.; Liu, G., Inhibiting the Corrosion-Promotion Activity of Graphene. *Chemistry of Materials* **2015,** *27* (7), 2367-2373.

14.   Dong, L.; Chen, Z.; Lin, S.; Wang, K.; Ma, C.; Lu, H., Reactivity-Controlled Preparation of Ultralarge Graphene Oxide by Chemical Expansion of Graphite. *Chemistry of Materials* **2017,** *29* (2), 564-572.

15.   Pan, S.; Aksay, I. A., Factors Controlling the Size of Graphene Oxide Sheets Produced via the Graphite Oxide Route. *ACS Nano* **2011,** *5* (5), 4073-4083.

16.   Wang, P.; Zhang, J.; Dong, L.; Sun, C.; Zhao, X.; Ruan, Y.; Lu, H., Interlayer Polymerization in Chemically Expanded Graphite for Preparation of Highly Conductive, Mechanically Strong Polymer Composites. *Chemistry of Materials* **2017,** *29* (8), 3412-3422.

17.   Lee, S. H.; Dreyer, D. R.; An, J.; Velamakanni, A.; Piner, R. D.; Park, S.; Zhu, Y.; Kim, S. O.; Bielawski, C. W.; Ruoff, R. S., Polymer Brushes via Controlled, Surface-Initiated Atom Transfer Radical Polymerization (ATRP) from Graphene Oxide. *Macromolecular Rapid Communications* **2010,** *31* (3), 281-288.

18.   Paredes, J. I.; Villar-Rodil, S.; Martínez-Alonso, A.; Tascón, J. M. D., Graphene Oxide Dispersions in Organic Solvents. *Langmuir* **2008,** *24* (19), 10560-10564.

19.   Yang, H.; Li, F.; Shan, C.; Han, D.; Zhang, Q.; Niu, L.; Ivaska, A., Covalent functionalization of chemically converted graphene sheets via silane and its reinforcement. *Journal of Materials Chemistry* **2009,** *19* (26), 4632-4638.

20.   Medhekar, N. V.; Ramasubramaniam, A.; Ruoff, R. S.; Shenoy, V. B., Hydrogen Bond Networks in Graphene Oxide Composite Paper: Structure and Mechanical Properties. *ACS Nano* **2010,** *4* (4), 2300-2306.

21.   McGrail, B. T.; Rodier, B. J.; Pentzer, E., Rapid Functionalization of Graphene Oxide in Water. *Chemistry of Materials* **2014,** *26* (19), 5806-5811.

22.   Sierra, U.; Álvarez, P.; Santamaría, R.; Granda, M.; Blanco, C.; Menéndez, R., A multi-step exfoliation approach to maintain the lateral size of graphene oxide sheets. *Carbon* **2014,** *80*, 830-832.

23.   Marcano, D. C.; Kosynkin, D. V.; Berlin, J. M.; Sinitskii, A.; Sun, Z.; Slesarev, A.; Alemany, L. B.; Lu, W.; Tour, J. M., Improved Synthesis of Graphene Oxide. *ACS Nano* **2010,** *4* (8), 4806-4814.

24.   Bai, H.; Li, C.; Wang, X.; Shi, G., On the Gelation of Graphene Oxide. *The Journal of Physical Chemistry C* **2011,** *115* (13), 5545-5551.

25.   Sudeep, P. M.; Narayanan, T. N.; Ganesan, A.; Shaijumon, M. M.; Yang, H.; Ozden, S.; Patra, P. K.; Pasquali, M.; Vajtai, R.; Ganguli, S.; Roy, A. K.; Anantharaman, M. R.; Ajayan, P. M., Covalently Interconnected Three-Dimensional Graphene Oxide Solids. *ACS Nano* **2013,** *7* (8), 7034-7040.

26.   Prasai, D.; Tuberquia, J. C.; Harl, R. R.; Jennings, G. K.; Bolotin, K. I., Graphene: Corrosion-Inhibiting Coating. *ACS Nano* **2012,** *6* (2), 1102-1108.

27.   Kirkland, N. T.; Schiller, T.; Medhekar, N.; Birbilis, N., Exploring graphene as a corrosion protection barrier. *Corrosion Science* **2012,** *56*, 1-4.

28.   Zhou, F.; Li, Z.; Shenoy, G. J.; Li, L.; Liu, H., Enhanced Room-Temperature Corrosion of Copper in the Presence of Graphene. *ACS Nano* **2013,** *7* (8), 6939-6947.

29.   Kang, D.; Kwon, J. Y.; Cho, H.; Sim, J.-H.; Hwang, H. S.; Kim, C. S.; Kim, Y. J.; Ruoff, R. S.; Shin, H. S., Oxidation Resistance of Iron and Copper Foils Coated with Reduced Graphene Oxide Multilayers. *ACS Nano* **2012,** *6* (9), 7763-7769.

30.   Qi, K.; Sun, Y.; Duan, H.; Guo, X., A corrosion-protective coating based on a solution-processable polymer-grafted graphene oxide nanocomposite. *Corrosion Science* **2015,** *98*, 500-506.

31.   Richard Prabakar, S. J.; Hwang, Y.-H.; Bae, E. G.; Lee, D. K.; Pyo, M., Graphene oxide as a corrosion inhibitor for the aluminum current collector in lithium ion batteries. *Carbon* **2013,** *52*, 128-136.

32.   Krishnamoorthy, K.; Jeyasubramanian, K.; Premanathan, M.; Subbiah, G.; Shin, H. S.; Kim, S. J., Graphene oxide nanopaint. *Carbon* **2014,** *72*, 328-337.

33.   Sørensen, P. A.; Kiil, S.; Dam-Johansen, K.; Weinell, C. E., Anticorrosive coatings: a review. *Journal of Coatings Technology and Research* **2009,** *6* (2), 135-176.

34.   Sangaj, N. S.; Malshe, V. C., Permeability of polymers in protective organic coatings. *Progress in Organic Coatings* **2004,** *50* (1), 28-39.

35.   Vergelati, C.; Perwuelz, A.; Vovelle, L.; Romero, M. A.; Holl, Y., Poly(ethylene terephthalate) surface dynamics in air and water studied by tensiometry and molecular modelling. *Polymer* **1994,** *35* (2), 262-270.

36.   Campbell, C. G.; Ummadisetty, S.; Storey, R. F., Decoupling and Functionalization of Coupled Polyisobutylene via Alkoxybenzene Quenching. *Macromolecules* **2016,** *49* (20), 7642-7652.

37.   Magenau, A. J. D.; Chan, J. W.; Hoyle, C. E.; Storey, R. F., Facile polyisobutylene functionalization via thiol-ene click chemistry. *Polymer Chemistry* **2010,** *1* (6), 831-833.

38.   Tan, H. S.; Pfister, W. R., Pressure-sensitive adhesives for transdermal drug delivery systems. *Pharmaceutical Science & Technology Today* **1999,** *2* (2), 60-69.

39.   Willenbacher, N.; Lebedeva, O., Polyisobutene-Based Pressure-Sensitive Adhesives. In *Technology of Pressure-Sensitive Adhesives and Products*, CRC Press: 2008; pp 4-1-4-18.

40.   Liu, Z.; Li, Y.; Yang, Y.; Li, Y.; Huang, X., ATNRC/SET-NRC synthesis of graphene/polyisobutylene nanocomposites. *Journal of Polymer Science Part A: Polymer Chemistry* **2013,** *51* (21), 4505-4514.

41.   Yang, Y.; Wang, J.; Zhang, J.; Liu, J.; Yang, X.; Zhao, H., Exfoliated Graphite Oxide Decorated by PDMAEMA Chains and Polymer Particles. *Langmuir* **2009,** *25* (19), 11808-11814.

42.   Oliveira, C. G.; Ferreira, M. G. S., Ranking high-quality paint systems using EIS. Part I: intact coatings. *Corrosion Science* **2003,** *45* (1), 123-138.

43.   Mao, H. Y.; Laurent, S.; Chen, W.; Akhavan, O.; Imani, M.; Ashkarran, A. A.; Mahmoudi, M., Graphene: Promises, Facts, Opportunities, and Challenges in Nanomedicine. *Chemical Reviews* **2013,** *113* (5), 3407-3424.

44.   Yin, P. T.; Shah, S.; Chhowalla, M.; Lee, K.-B., Design, Synthesis, and Characterization of Graphene–Nanoparticle Hybrid Materials for Bioapplications. *Chemical Reviews* **2015,** *115* (7), 2483-2531.

45.   Cui, Y.; Kundalwal, S. I.; Kumar, S., Gas barrier performance of graphene/polymer nanocomposites. *Carbon* **2016,** *98*, 313-333.

46.   Pei, S.; Cheng, H.-M., The reduction of graphene oxide. *Carbon* **2012,** *50* (9), 3210-3228.

47.   Pei, S.; Zhao, J.; Du, J.; Ren, W.; Cheng, H.-M., Direct reduction of graphene oxide films into highly conductive and flexible graphene films by hydrohalic acids. *Carbon* **2010,** *48* (15), 4466-4474.

48.   Georgakilas, V.; Tiwari, J. N.; Kemp, K. C.; Perman, J. A.; Bourlinos, A. B.; Kim, K. S.; Zboril, R., Noncovalent Functionalization of Graphene and Graphene Oxide for Energy Materials, Biosensing, Catalytic, and Biomedical Applications. *Chemical Reviews* **2016,** *116* (9), 5464-5519.

49.   Cheng, C.; Li, S.; Thomas, A.; Kotov, N. A.; Haag, R., Functional Graphene Nanomaterials Based Architectures: Biointeractions, Fabrications, and Emerging Biological Applications. *Chemical Reviews* **2017,** *117* (3), 1826-1914.

50.   Montes-Navajas, P.; Asenjo, N. G.; Santamaría, R.; Menéndez, R.; Corma, A.; García, H., Surface Area Measurement of Graphene Oxide in Aqueous Solutions. *Langmuir* **2013,** *29* (44), 13443-13448.

51.   McAllister, M. J.; Li, J.-L.; Adamson, D. H.; Schniepp, H. C.; Abdala, A. A.; Liu, J.; Herrera-Alonso, M.; Milius, D. L.; Car, R.; Prud'homme, R. K.; Aksay, I. A., Single Sheet Functionalized Graphene by Oxidation and Thermal Expansion of Graphite. *Chemistry of Materials* **2007,** *19* (18), 4396-4404.

52.   Rubino, R. S.; Takeuchi, E. S., The study of irreversible capacity in lithium-ion anodes prepared with thermally oxidized graphite. *J Power Sources* **1999,** *81*, 373-377.

53.   Guan, Y.; Meyers, K. P.; Mendon, S. K.; Hao, G.; Douglas, J. R.; Trigwell, S.; Nazarenko, S. I.; Patton, D. L.; Rawlins, J. W., Ecofriendly Fabrication of Modified Graphene Oxide Latex Nanocomposites with High Oxygen Barrier Performance. *ACS Applied Materials & Interfaces* **2016,** *8* (48), 33210-33220.

54.   Naficy, S.; Jalili, R.; Aboutalebi, S. H.; Gorkin Iii, R. A.; Konstantinov, K.; Innis, P. C.; Spinks, G. M.; Poulin, P.; Wallace, G. G., Graphene oxide dispersions: tuning rheology to enable fabrication. *Materials Horizons* **2014,** *1* (3), 326-331.

55.   Cheng, C.; Li, D., Solvated Graphenes: An Emerging Class of Functional Soft Materials. *Advanced Materials* **2013,** *25* (1), 13-30.

56.   Stankovich, S.; Piner, R. D.; Nguyen, S. T.; Ruoff, R. S., Synthesis and exfoliation of isocyanate-treated graphene oxide nanoplatelets. *Carbon* **2006,** *44* (15), 3342-3347.

57.   Ganguly, A.; Sharma, S.; Papakonstantinou, P.; Hamilton, J., Probing the Thermal Deoxygenation of Graphene Oxide Using High-Resolution In Situ X-ray-Based Spectroscopies. *The Journal of Physical Chemistry C* **2011,** *115* (34), 17009-17019.

58.   Tao, C.-a.; Wang, J.; Qin, S.; Lv, Y.; Long, Y.; Zhu, H.; Jiang, Z., Fabrication of pH-sensitive graphene oxide-drug supramolecular hydrogels as controlled release systems. *Journal of Materials Chemistry* **2012,** *22* (47), 24856-24861.

59.   Roy, S.; Das, T.; Yue, C. Y.; Hu, X., Improved Polymer Encapsulation on Multiwalled Carbon Nanotubes by Selective Plasma Induced Controlled Polymer Grafting. *ACS Applied Materials & Interfaces* **2014,** *6* (1), 664-670.

60.   Chen, J.-T.; Fu, Y.-J.; An, Q.-F.; Lo, S.-C.; Huang, S.-H.; Hung, W.-S.; Hu, C.-C.; Lee, K.-R.; Lai, J.-Y., Tuning nanostructure of graphene oxide/polyelectrolyte LbL assemblies by controlling pH of GO suspension to fabricate transparent and super gas barrier films. *Nanoscale* **2013,** *5* (19), 9081-9088.

61.   Ferrari, A. C.; Robertson, J., Interpretation of Raman spectra of disordered and amorphous carbon. *Physical Review B* **2000,** *61* (20), 14095-14107.

62.   Cançado, L. G.; Jorio, A.; Ferreira, E. H. M.; Stavale, F.; Achete, C. A.; Capaz, R. B.; Moutinho, M. V. O.; Lombardo, A.; Kulmala, T. S.; Ferrari, A. C., Quantifying Defects in Graphene via Raman Spectroscopy at Different Excitation Energies. *Nano Letters* **2011,** *11* (8), 3190-3196.

63.   Yang, B.; Parada, C. M.; Storey, R. F., Synthesis, Characterization, and Photopolymerization of Polyisobutylene Phenol (Meth)acrylate Macromers. *Macromolecules* **2016,** *49* (17), 6173-6185.

64.   Fang, M.; Wang, K.; Lu, H.; Yang, Y.; Nutt, S., Covalent polymer functionalization of graphene nanosheets and mechanical properties of composites. *Journal of Materials Chemistry* **2009,** *19* (38), 7098-7105.

65.   Dikin, D. A.; Stankovich, S.; Zimney, E. J.; Piner, R. D.; Dommett, G. H. B.; Evmenenko, G.; Nguyen, S. T.; Ruoff, R. S., Preparation and characterization of graphene oxide paper. *Nature* **2007,** *448* (7152), 457-460.

66.   Pan, Q.; Chung, C.-C.; He, N.; Jones, J. L.; Gao, W., Accelerated Thermal Decomposition of Graphene Oxide Films in Air via in Situ X-ray Diffraction Analysis. *The Journal of Physical Chemistry C* **2016,** *120* (27), 14984-14990.

67.   Sato, M.; Kato, T.; Ohishi, T.; Ishige, R.; Ohta, N.; White, K. L.; Hirai, T.; Takahara, A., Precise Synthesis of Poly(methyl methacrylate) Brush with Well-Controlled Stereoregularity Using a Surface-Initiated Living Anionic Polymerization Method. *Macromolecules* **2016,** *49* (6), 2071-2076.

68.   Sawaguchi, T.; Seno, M., Thermal degradation of polyisobutylene: effect of end initiation from terminal double bonds. *Polymer Degradation and Stability* **1996,** *54* (1), 33-48.

69.   Reichardt, C., Front Matter. In *Solvents and Solvent Effects in Organic Chemistry*, Wiley-VCH Verlag GmbH & Co. KGaA: 2004; pp i-xxvi.

70.   Farris, S.; Introzzi, L.; Biagioni, P.; Holz, T.; Schiraldi, A.; Piergiovanni, L., Wetting of Biopolymer Coatings: Contact Angle Kinetics and Image Analysis Investigation. *Langmuir* **2011,** *27* (12), 7563-7574.

71.   Liu, Y.; Soer, W.-J.; Scheerder, J.; Satgurunathan, G.; Keddie, J. L., Water Vapor Sorption and Diffusion in Secondary Dispersion Barrier Coatings: A Critical Comparison with Emulsion Polymers. *ACS Applied Materials & Interfaces* **2015,** *7* (22), 12147-12157.

72.   Landolt, D., *Corrosion and Surface Chemistry of Metals*. EFPL Press: 2007.

73.   Frankel, G. S., Fundamentals of Corrosion Kinetics. In *Active Protective Coatings: New-Generation Coatings for Metals*, Hughes, A. E.; Mol, J. M. C.;

Zheludkevich, M. L.; Buchheit, R. G., Eds. Springer Netherlands: Dordrecht, 2016; pp 17-32.

74.   Liu, X.; Xiong, J.; Lv, Y.; Zuo, Y., Study on corrosion electrochemical behavior of several different coating systems by EIS. *Progress in Organic Coatings* **2009,** *64* (4), 497-503.

75.   Hinderliter, B. R.; Croll, S. G.; Tallman, D. E.; Su, Q.; Bierwagen, G. P., Interpretation of EIS data from accelerated exposure of coated metals based on modeling of coating physical properties. *Electrochimica Acta* **2006,** *51* (21), 4505-4515.

76.   Behzadnasab, M.; Mirabedini, S. M.; Esfandeh, M., Corrosion protection of steel by epoxy nanocomposite coatings containing various combinations of clay and nanoparticulate zirconia. *Corrosion Science* **2013,** *75*, 134-141.

77.   iknahad, M.; Moradian, S.; Mirabedini, S. M., The adhesion properties and corrosion performance of differently pretreated epoxy coatings on an aluminium alloy. *Corrosion Science* **2010,** *52* (6), 1948-1957.

78.   Boinovich, L. B.; Gnedenkov, S. V.; Alpysbaeva, D. A.; Egorkin, V. S.; Emelyanenko, A. M.; Sinebryukhov, S. L.; Zaretskaya, A. K., Corrosion resistance of composite coatings on low-carbon steel containing hydrophobic and superhydrophobic layers in combination with oxide sublayers. *Corrosion Science* **2012,** *55*, 238-245.

79.   Parhizkar, N.; Shahrabi, T.; Ramezanzadeh, B., A new approach for enhancement of the corrosion protection properties and interfacial adhesion bonds between the epoxy coating and steel substrate through surface treatment by covalently modified amino functionalized graphene oxide film. *Corrosion Science* **2017,** *123*, 55-75.

80.   Bard, A. J.; Faulkner, L. R., *Electrochemical Methods: Fundamentals and Applications*. Wiley: 2000.

81.   Yu, Z.; Lv, L.; Ma, Y.; Di, H.; He, Y., Covalent modification of graphene oxide by metronidazole for reinforced anti-corrosion properties of epoxy coatings. *RSC Advances* **2016,** *6* (22), 18217-18226.

CHAPTER IV – CORROSION PROTECTION STUDY OF WATERBORNE EPOXY

BILAYER COATINGS WITH HYDROPHOBIC SURFACE AND GRAPHENE

OXIDE OXYGEN BARRIER

Time-dependent corrosion protection performance of bilayer waterborne epoxy-amine (WBEP) coatings were studied in simulated corrosive environments by monitoring the coating impedance or coating delamination. In the first layer (primer), lamellar graphene oxide (GO) were incorporated to improve oxygen barrier property, which were studied by measuring permeability of O_2 through free-standing films that contained increasing loading of GO. Permeability of O_2 was decreased by ~80% with ~1.8 wt.% GO loading owing to tortuosity effect, which was confirmed by cross-sectional transmission electron microscopical (TEM) images showing highly dispersed lamellar morphology of GO in polymer matrix. The second layer (top coat) contained an organic wax, polyethylene (PE-alloy), which could increase water contact angle (WCA) by ~30º with 1-5 wt.% loading in polymer, thereby endowing water repellant property. Electrochemical impedance spectroscopy (EIS) analysis of intact coatings indicated that the bilayer coating with a hydrophobic surface exhibited higher impedance and lower microscopical delamination (calculated by breaking point frequency) in comparison with the neat WBEP coating under immersion and exposure corrosive conditions. In addition, coating delamination induced from a scribe was analyzed on simulated defect coatings to study the anticorrosive property under both environmental conditions.

4.1 Introduction

Corrosion has a profound impact on the reliability and service lifetime of metallic devices. Billions of dollars are spent on corrosion-related maintenance and replacement

every year.[1-2] Although corrosion, the process of metal oxidation by interacting with oxidants (i.e. O_2, CO_2, HCl), is thermodynamically favored, the rate can be significantly different depends on the environmental conditions and the presence of moisture and salts that affect the kinetics.[3-4] Numerous corrosion protection techniques have been developed for metallic facilities in various environmental conditions based on three strategies: 1) isolation of metals from corrosive environment; 2) suppression of anodic metal dissolution; and 3) suppression of the corresponding cathodic reaction.[3, 5] Organic (polymeric) coatings are generally used to afford corrosion mitigations through the isolation mechanism due to barrier effect.[3, 6]

Successful environmental isolation requires that organic coatings have good barrier properties and enduring adherence to metal substrate at the same time.[7] Many polymers, including alkyd, epoxy, polyurethane, polyvinyl chloride, acrylates, polyester, and chlorinated rubber have been employed as binder matrices in anticorrosive coatings.[6, 8-14] Among them, epoxy resin is the most widely used polymer owing to its low cost, high electrical insulation, strong adhesion for various surfaces, thermal and mechanical stability, and excellent barrier properties.[6] However, the structural integrity of epoxy coatings diminishes over time due to absorbed water from environments, which leads to inevitable penetration of corrosive species and reduces barrier effect.[12, 15-16] Besides, water ingress at the metal/coating interface can jeopardize adhesion of coatings and result in coating delamination and corrosive failure.[17-19]

Increasing the crosslink density of epoxy resin was shown to be effective on reducing water uptake and water diffusion rate by Sangaj and coworkers.[20-21] However, brittleness and high glass transition temperature (Tg) may have a negative impact on

adhesive property.[22] Pigments and inorganic fillers incorporated in polymeric coatings have shown improving corrosion resistance in long-term performance, which is believed to be related with decreased permeability or increased adhesion.[18, 23-25] Addition of nanofillers such as carbon nanotubes, hydrophobic silica, and graphene have been shown successful on increasing barrier property and oxidation/corrosion resistance much more effectively than conventional materials in polymer nanocomposites (PNCs).[26-28] Therefore, surface coatings for marine, aerospace, pipelines, automobile, and construction applications can be developed with the benefit of prolonged service lifetime and reduced weight by using advanced nanomaterials.[29-30]

Graphene (Gr), with a unique two-dimensional honeycomb structure, exhibits chemical inertness and stability, thermal and electrical conductivity, high modulus and strength, as well as gas impermeability.[31-33] Gr thin films deposited on copper can protect metal from high-temperature oxidation and aqueous corrosion[29-30], however, long-term performance can be restricted by the difficulties on immobilization of graphene directly to metal surfaces.[34] Moreover, Gr shows poor dispersibility in most solvents due to lack of surface functionalities, and incorporation of graphene functional additives in organic coatings is still challenging.[35] Graphene oxide (GO) is an alternative form of lamellar carbon nanomaterials, which exhibits much ameliorated dispersibility and compatibility due to oxygenated functional groups (hydroxyl and epoxide functional group on its basal plane, and carbonyl and carboxyl groups on the edges).[36-37] GO reinforced PNCs have been studied for various applications including surface coatings, and the effectiveness of reinforcement was shown to increase with GO loading.[38-39] Prabakar and coworkers found that GO could effectively suppress the oxidation of aluminum current collector in

lithium ion battery.[40] Sun and coworkers synthesized 3-aminopropyl triethoxysilane

modified reduced GO (rGO) derivative, which exhibited enhanced barrier and corrosion

resistance property when adding in polyvinylbutyral (PVB) coating.[34] Ramezanzadeh and

coworkers[41], Yu and coworkers[42] investigated the anticorrosive performance of GO and

GO derivatives incorporated in epoxy coatings, respectively. Qi and coworkers also

reported anticorrosive performance of polymer-grafted GO nanocomposite coatings on

steel substrate.[43] These studies indicated a synergistic effect due to grafting endows

elevated property over neat polymer or GO coating with increasing grafting density.

Besides the impact of tortuosity effect in the bulk of organic coatings, surface

wettability also can be tuned to retard water penetration and maintain sufficient corrosion

protection.[3, 20] Incorporation of low surface energy materials, such as silicone resin (22

mN/m) or fluorine-containing compounds (10 mN/m), can significantly increase the

surface hydrophobicity and water repellent property.[44-46] Moreover, incorporation of

hierarchical microstructures to hydrophobic surface endows superhydrophobicity, for

which water contact angle is larger than 150º and sliding angle is smaller than 10º.[46-47]

Because of such a strong self-cleaning effect, it is difficult for water and dissolved

corrosive species (i.e. O_2 and NaCl) to diffuse into coating bulk and aqueous corrosion

can be diminished.[46-47] However, such a surface modification method still suffers from

low durability and high cost, which greatly limit its applications as anticorrosive coatings.

Legislative restrictions on volatile organic compound (VOC) emissions have

driven the development of ecofriendly coatings, such as high-solid coatings, powder

coatings, non-solvent coatings, and waterborne coatings.[48] Although commercial

waterborne epoxy coatings have been available for several years, their market shares stay

small on anticorrosive coatings.[49] One possible reason is that their low water resistance in comparison with traditional solvent-based systems can decrease the overall barrier effect and reduce corrosion resistance.[49-50] Incorporation of hydrophobic copolymers has been reported to successfully improve the performance of waterborne epoxy coatings[14, 49], however, using functional filler/additive instead will bring more flexibility and higher cost-effectiveness to the formulation ability of epoxy coating system.[51] Therefore, in this study, functional fillers that can modify surface and bulk property of waterborne epoxy-amine coating (WBEP) were incorporated to enhance coating barrier to water and O_2.

Anticorrosive bilayer waterborne coating system contains a thicker primer with GO incorporated and a thinner top layer with polyethylene wax additive (PE-alloy). An in-house waterborne epoxy dispersion cured with an aliphatic amine hardener was used as binder polymer for both layers. GO lamellae exhibited excellent dispersibility and compatibility in this water-based epoxy-amine coating. O_2 permeability of the resulting GO nanocomposite significantly decreased. WBEP top layer coating with PE-alloy showed increasing water contact angle and reduced moisture adsorption with increasing filler concentration. Coating impedance of single-layer WBEP and bilayer coating system was measured over time under immersion and salt spray exposure conditions by electrochemical impedance spectroscopy (EIS). EIS is an in situ and non-destructive technique for studying corrosion resistance of coated and bare metal substrate in simulated environmental conditions.[4, 52-53] The impedance response of a given metal/coating system under a small-amplitude alternating potential signal is influenced by many factors, such as the surface roughness of metal, the coating/substrate interface, the porosity of coating with water ingress over time and so on. The impedance value of

organic coatings is normally measured on an intact coating, where the barrier effect towards water/electrolyte solution is the dominating factor.[46, 54] On the other hand, in many cases corrosion failure of an anticorrosive coating can be largely due to a macroscopic defect, by which the coating/metal interface is exposed. Therefore, in addition to impedance measurements, corrosion protection performance was also studied on coatings with simulated defects (i.e. a scribe) to investigate the delamination distance from the scribe.
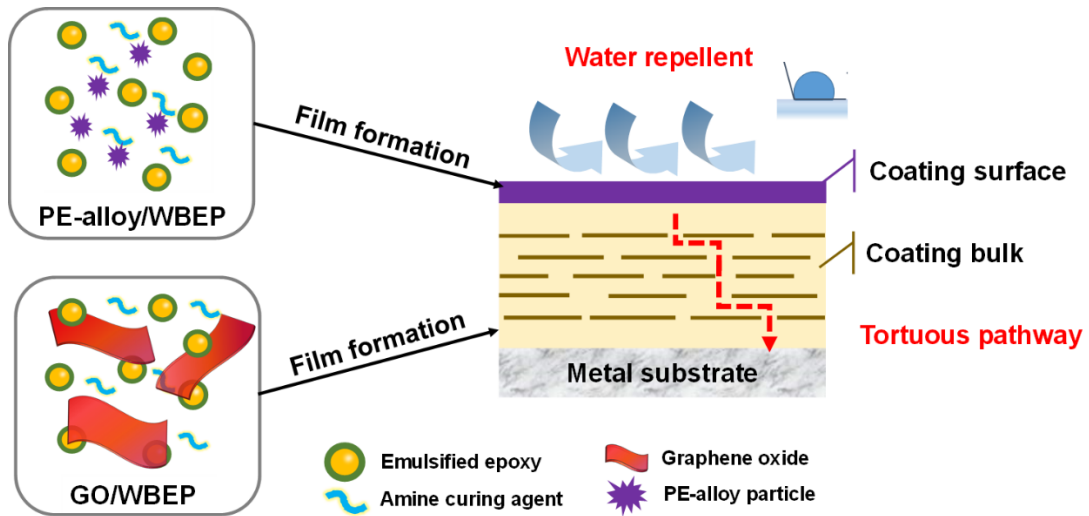
Figure 4.1 Schematic representation of the fabrication of WBEP-based bilayer coating system.

4.2 Experimental

4.2.1 Materials

Reagents for graphene oxide synthesis were purchased from Sigma-Aldrich and used without purification unless otherwise specified, including graphite flakes (cat.#332461, ~150 μm), potassium permanganate (99% pure), phosphoric acid (85% H_3PO_4 in water), sulfuric acid (95–98% H_2SO_4), hydrogen peroxide (30 wt% H_2O_2 in water), hydrochloric acid (30–35% HCl in water), and in-house deionized (DI) water

(MilliQ, 18 MΩ). In-house waterborne epoxy (WBEP) was prepared from diglycidyl ether of bisphenol A (DGEBA, Epon 828) epoxy resin purchased from Shell (USA). Anquamine 419 (Aq-419) waterborne curing agent was generously provided by Air Products and Chemicals, Inc. (USA) free of charge. Polyethylene alloy additive was provided generously by Shamrock Technologies (USA) free of charge.

Aluminum 2024 (A36) coupon (75mm×15mm×0.5mm) and cold rolled low carbon steel (QD36) coupon (75mm×15mm×1mm) was purchased from Q-LAB Corporation (USA) and used as received. Coupons were thoroughly rinsed with acetone, cleaned with paper tower to remove any oil contaminants, and fully dried under nitrogen gas flow before any coating applications. The waterborne epoxy used was synthesized in-house and curing agent (Aquamine-419) was kindly donated by Airproduct Inc.

4.2.2 Synthesis of The Waterborne Epoxy and GO

Waterbased epoxy dispersion was prepared *via* phase-inversion technique at ambient under agitation of ~ 1500 rpm and water feeding rate of ~ 4.5 mL/min. The resulting dispersion had 56% solid and equivalent epoxy weight (EEW) of 389 g/equiv. GO was synthesized according to a previously reported protocol.[55]

4.3 Preparation of Single-layer and Bilayer Coatings

Curing agent mixture with 30% solid content was prepared by adding equal amount of DI water to pristine Aquamine-419 and thoroughly mixing on a Flacktek SpeedMixer. The epoxy to amine-H molar ratio chosen for this study is 1.2 to minimize unreacted amine functionalities in the system. The schematic representation of the fabrication of WBEP-based bilayer coating system is shown in Figure 4.1. Single-layer coating of waterborne epoxy-amine resin (WBEP) was prepared by mixing 2.4 g of

waterborne epoxy, 2.92 g of amine solution, and 2 g of DI water on the speed mixer

followed with drawdown application on A36 (Q-panels). The bilayer coating consisted of

a bottom layer of GO/WBEP composites with 1.8wt.% of GO loading, and a top layer of

PE-alloy/WBEP composites with 5wt.% of PE-alloy content. The bottom layer was

applied on A36 substrate by drawdown bar and the top layer was applied with a roller

bar. The single-layer coating was cured in forced air oven at 40, 60 and 80 ℃ for 12, 24,

and 2 h. For bilayer coating, the first layer was cured at 40 ℃ for 12 h before second

layer was applied, and then was cured at 40, 60 and 80 ℃. The average coating thickness

measured on single-layer waterborne epoxy-amine coating was 22 ± 1.5 μm, while the

total thickness of bilayer coating was 18 ± 2.5 μm.

4.3.1 Preparation of WBEP, GO/WBEP, and PE-alloy/WBEP Free-standing Films

Oxygen permeability and cross-sectional TEM images were obtained on free-

standing films of neat waterborne epoxy-amine (WBEP) and GO/WBEP composites with

varying GO loading (0.2, 0.5, 0.9 and 1.8 wt.%). GO was first dispersed in DI water via

ultrasonication before adding waterborne epoxy. The mixture was thoroughly blended

twice on a Flacktek SpeedMixer for 10 min at 1500 rpm. Then amine cure agent was

added and fully blended twice for 5 min at 1800 rpm. Samples were cured in mold at

elevated temperature in forced air oven at 40, 60 and 80 ℃ for 12, 24, and 2 h in

succession.

Free-standing film with PE-alloy were prepared similarly by mixing the

components in a vail using SpeedMixer for 10 min at 1500 rpm. Samples were cured on

aluminum foils under the same temperature profile.

4.3.2 Characterization

FTIR spectra of GO were acquired using a Nicolet 6700 FTIR spectrometer in attenuated total reflectance (ATR) mode. Raman spectra were collected with a Thermo Scientific DXR Raman microscope with 633 nm excitation laser. UV absorption spectra were collected by a Lambda 35 ultraviolet–visible (UV–vis) spectrometer (PerkinElmer, Inc.) with a 326 nm UV lamp.

The dimensions of GO platelet were determined via AFM in tapping-mode with a SiC probe (1/T300 TM, Bruker). Samples for AFM analysis were prepared by drop-casting films from diluted (~0.0001 wt %) aqueous GO suspensions. The dispersion morphology was studied by a JEOL 2100 transmission electron microscopy (TEM) in high-vacuum mode operated at 200 kV.

Water contact angle (WCA) were acquired on thin film surface deposited on cold rolled steel (CRS) substrate using a Ramé-hart 200-00 Std.-Tilting B. goniometer with 4 μL water droplets. The measurements were carried out at ambient and the shape of droplet was recorded by digital camera and analyzed using the software. Water vapor sorption was measured by using a Q5000 SA (TA Instruments) at 35 ℃ and 95% relative humidity (RH). Samples were equilibrated at 75 ℃ and 0% RH for 2 h before testing.

The glass transition temperature (T_g) was measured via dynamic mechanical analysis (Q800 DMA, TA Instruments) in multi-frequency-strain mode at 1 Hz and 2 °C min^{-1} ramping rate and differential scanning calorimetry (Q2000 DSC, TA Instruments) in nitrogen at a 10 °C min^{-1} heating rate and a 5 °C min^{-1} cooling rate.

O_2 permeability was measured at 25 ℃, 0% relative humidity (RH) and 1 atm partial oxygen pressure difference using OX-TRAN 2/21 ML (MOCON). A continuous-flow method of ASTM D3985-81 was employed with nitrogen as a carrier gas to measure

oxygen flux through a free-standing film attached to an aluminum mask with an exposure area of 5 cm^2. Ultra-thin (~ 100 nm) sections of LNCs film samples embedded in epoxy resin for TEM studies were obtained using a microtome at RT and collected with a copper grid.

4.3.3 Electrochemical Impedance Spectroscopy (EIS)

Electrochemical impedance spectroscopy (EIS) was conducted on 2024 aluminum substrates with different coating systems in 3.5 wt% NaCl solution immersion. The measurement was done by Princeton Verstate 4 using a three-electrode cell consisting of Ag/AgCl reference electrode, platinum counter electrode, and coated panel as working electrode with 1 cm^2 exposure area. Open circuit potential (OCP) was performed each time before collecting electrochemical impedance spectra. The scan rate was 1 mV s^{-1} from 10^{-2} Hz to 10^5 Hz at ± 20 mV OCP. The exposing area for specimen as working electrode was 1 cm^2.

Coating delamination study were conducted on low carbon steel (QD 36 panels) coated with a single-layer neat WBEP coating, a single-layer PE-alloyl (5%)/WBEP coating and a bilayer coating of the same components as described above.

4.4 Results and Discussion

4.4.1 Characterization

The vibrational bands at ~3400 cm^{-1}, ~1750−1650 cm^{-1}, and ~1250−950 cm^{-1} in the FTIR spectrum (Figure 4.2a) of GO indicates the presence of hydroxyl (−OH), carboxyl (−COOH)/carbonyl (C=O), and epoxy (C–O–C) functional groups.[55] The strong IR bands at ~2915 cm^{-1}, 2848 cm^{-1} and ~1470 cm^{-1} in the spectrum of (Figure 4.2a) PE-alloy are attributed to C–H stretching vibration of –CH$_2$–, –CH$_3$ groups.[56] The IR

spectrum (Figure 4.2a) of neat WBEP indicates the existence of –OH, C–H, C=C, C–O–C, and C–N moieties.[57] The addition of GO (1.8 wt%) or PE-alloy (5 wt%) shows minor impact on IR spectra of the composite films under such low concentrations.
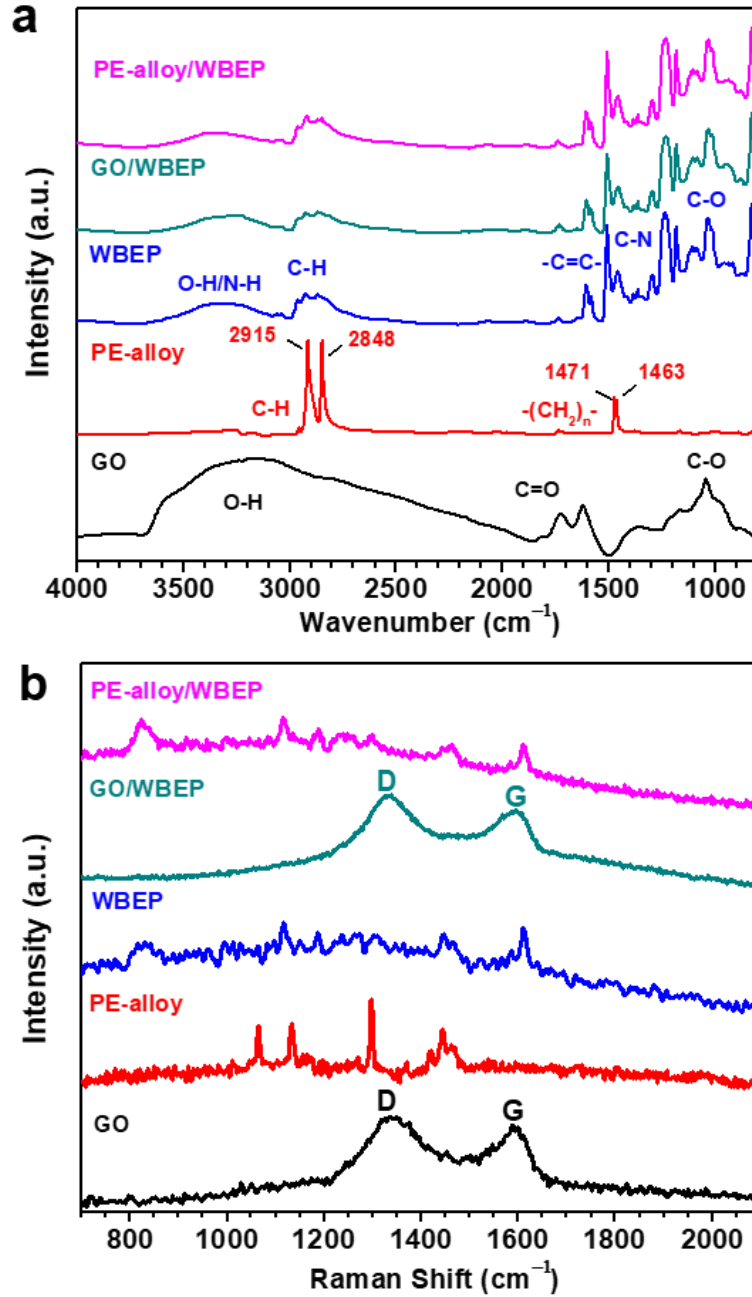

Figure 4.2 FTIR (a) and Raman (b) spectra of GO, PE-alloy, WBEP, GO/WBEP and PE-alloy/WBEP (composite) sample films.

The presence of D (~1350 cm^{-1}) and G (~1580−1600 cm^{-1}) bands in Raman spectra is a typical indication of sp^2 carbon composition in carbon materials.[58-59] Raman spectra (Figure 4.2b) of GO and GO/WBEP showed strong D and G bands: the former results from the first order scattering of the E$_{2g}$ phonon of in-plane vibrations of sp^2 bonded carbon atoms; and the later ascribes to a defect-induced A$_{1g}$ breathing mode of sp^2 rings. The weak band at ~1600 cm^{-1} in Raman spectra (Figure 4.2b) of neat WBEP and PE-alloy/WBEP composite is due to aromatic structure in resin.[60]
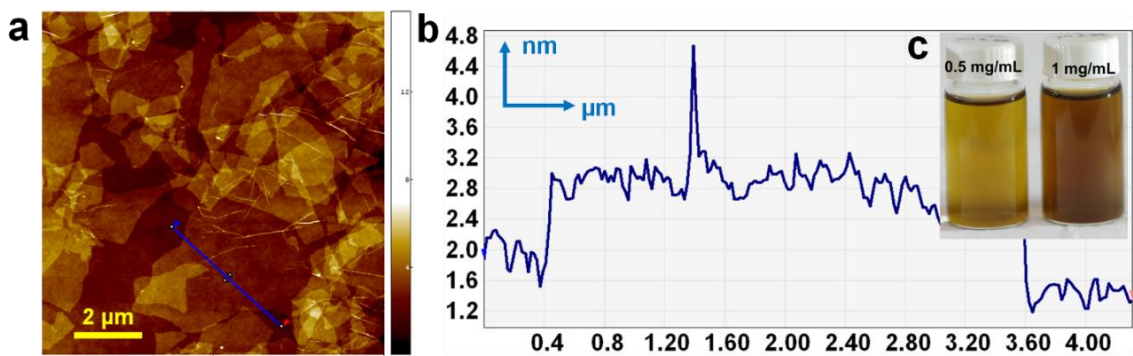
Figure 4.3 AFM height image (a) and profile (b), and aqueous suspension (c) of GO platelet.

4.4.2 Oxygen Barrier Property of GO/WBEP Composites

The AFM height images and profiles (Figure 4.3a and b) of GO indicates irregular shape for GO platelets with lamellar thickness of 1~2 nm. Digital image of GO aqueous suspensions with concentrations of 0.5 and 1 mg/mL are shown in Figure 4.3c, indicating good processing compatibility in waterborne systems. Free-standing films of GO/WBEP composites were prepared with increasing GO loading from 0.2 wt% to 1.8 wt%. Transparency of the resulting films was determined by UV-vis spectroscopy (Figure 4.4a) with the corresponding digital image of these films shown in Figure 4.4b. As expected, the opacity of composite films increased with increasing GO loading.
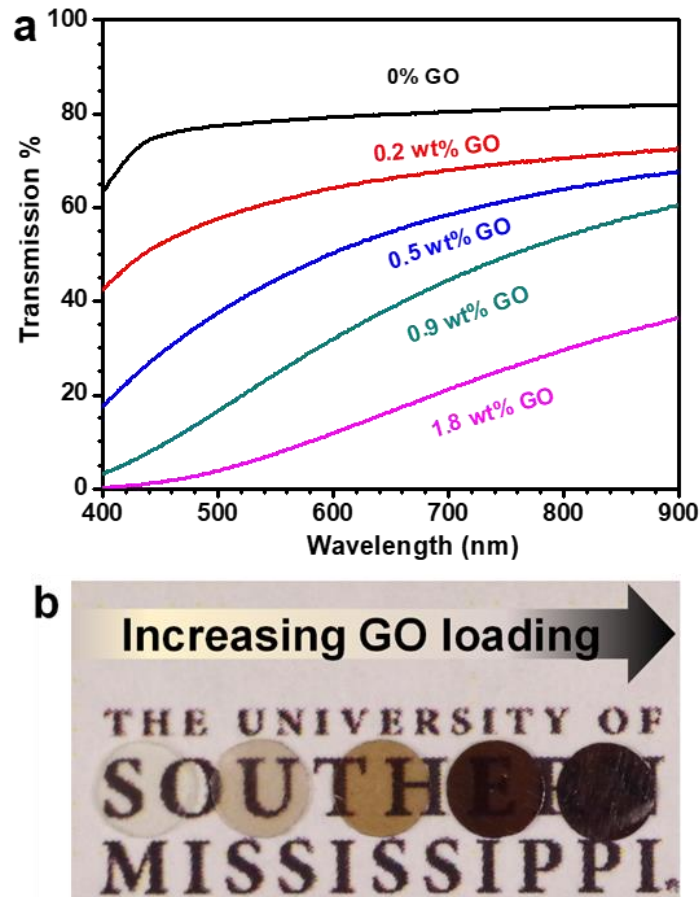
Figure 4.4 UV-vis spectra transparency (a) and digital image of GO/WBEP composites with 0.2, 0.5, 0.9 and 1.8 wt.% of GO loading.

TEM was employed to directly study the dispersing morphology of GO lamellae in the GO/WBEP composites by using ultra-thin sections obtained by microtoming. GO reveales sufficient contrast against resin matrix to be imaged without staining.[55] Cross-sectional TEM images (Figure 4.5) of GO/WBEP composites at low and high magnifications imply relatively uniform dispersion of GO at all concentrations. Random distribution of GO platelet can be observed at low GO loading (0.2%), while increasing alignment started to form with increasing GO loadings (0.5-1.8 wt%). Steric interactions between GO platelet were believed to induce aligned morphology, which are typically observed when the lateral dimension of nanoparticle is sufficiently large.

110
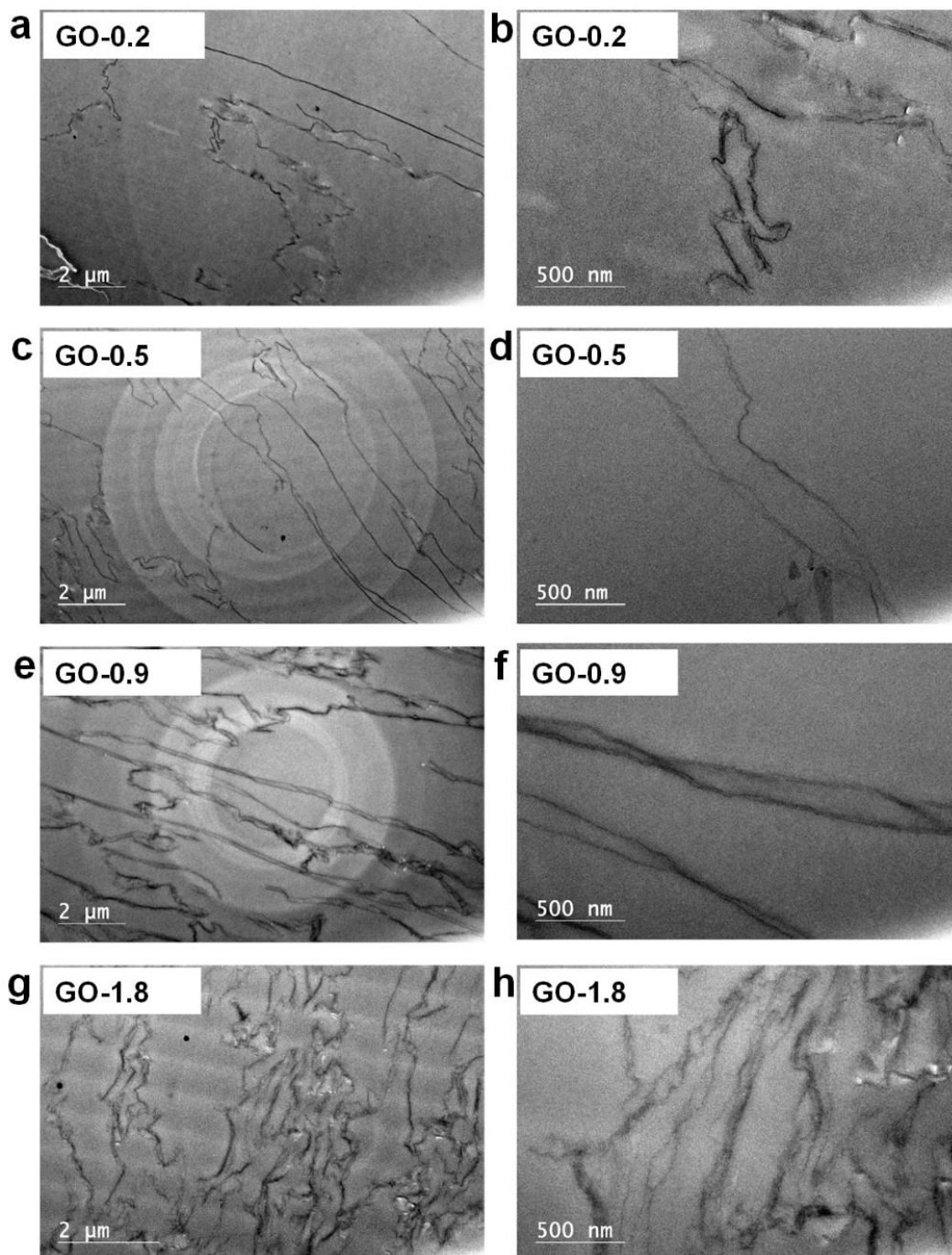
Figure 4.5 Cross-sectional TEM images of GO/WBEP films with 0.2-1.8 wt.% GO loading under low (a, c, e, g) and high (b, d, f, h) magnifications.

As an inert molecule, permeation of O_2 in polymeric materials is governed only by the intrinsic properties of polymer matrix, such as crosslinking, crystallinity, glass

transition temperature (T_g), and so on.[20] The average physical state (i.e. glassy *vs.*

rubbery) of a polymer, which is determined by the difference between the ambient

temperature and T_g, shows a dominating impact on the permeation process.[26] Therefore,

the measured T_g (~65–71 °C by DSC) of polymer matrix (epoxy-amine resin) was

significantly above the average testing temperatures, that film(s) and coating(s) were

considered to be in their glassy states. O_2 barrier property was determined by measuring

steady-state oxygen flux through the polymeric/composite film normalized by film

thickness.[61] As shown in Figure 4.6, O_2 permeability decreased by ~80% with 1.8 wt% of

GO loaded in polymer matrix. Permeability decrease in nanoplatelet based composite

systems is primarily due to tortuous effect, which reduces gas diffusivity by creating

elongated pathway through the composite for penetrating molecules. Besides, the

concentration, aspect ratio, orientation, and dispersion state of nanoplatelets in the matrix

will all show impact on the diffusion barrier efficiency.
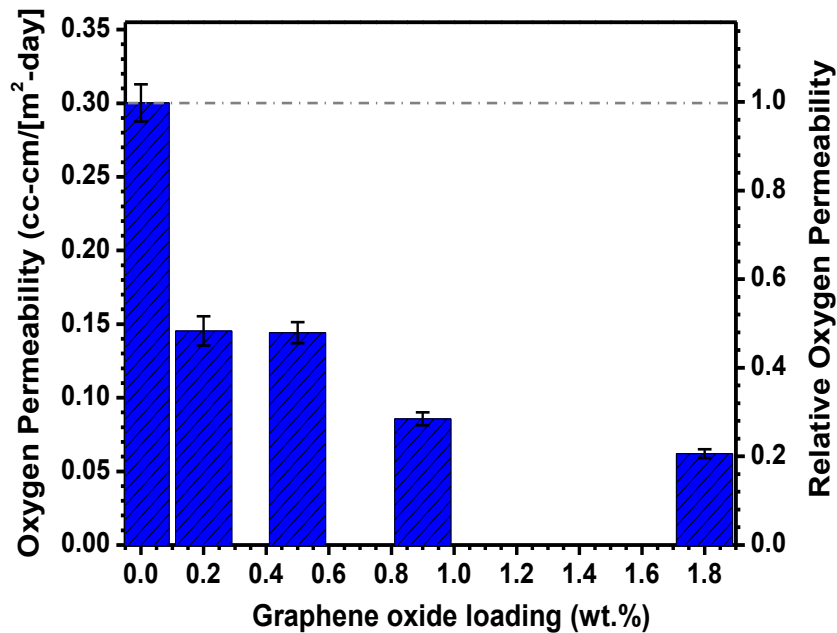
Figure 4.6 O_2 permeability of GO/WBEP composite films with 1.8 wt.% GO loading.

4.4.3 Surface Wettability of PE-alloy/WBEP Composites
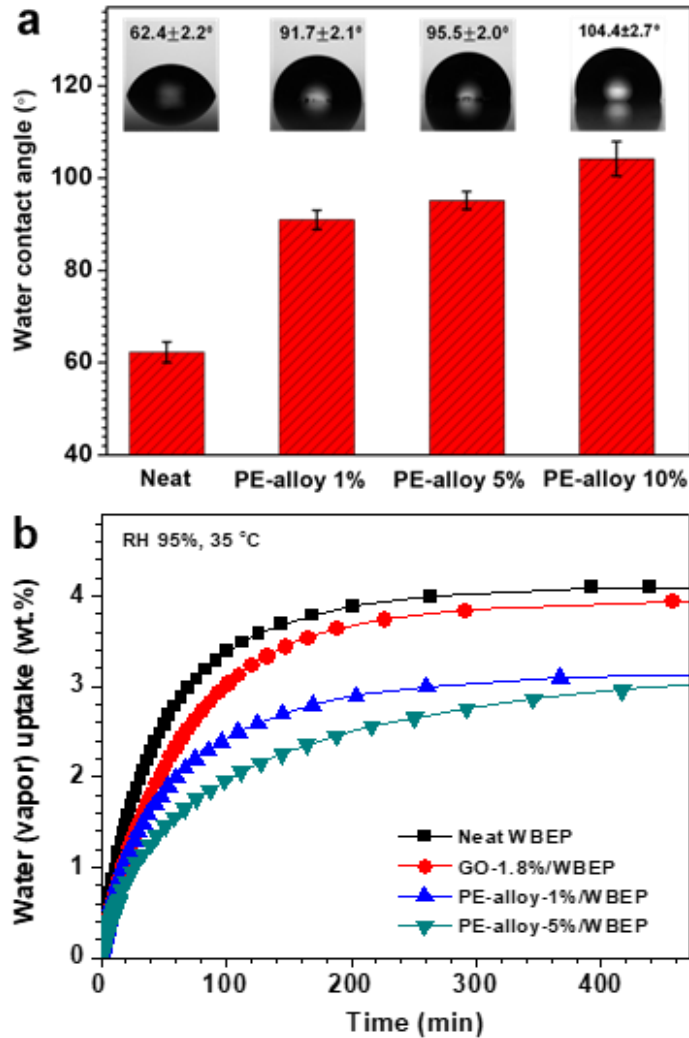
Figure 4.7 (a) Water contact angle of PE-alloy/WBEP composite surface and (b) vapor sorption of free-standing composite films with PE-alloy or GO.

Water contact angle (WCA) measurement, one of the most established methods for studying surface wettability of materials, was performed on coated aluminum substrate with results displayed in Figure 4.7a.[62] Neat WBEP surface showed CA of 62.4 ± 2.2º, which indicated a hydrophilic surface for epoxy resin. PE-alloy/WBEP composite coatings exhibited significantly increased CA, which was 91.7 ± 2.1º with 1 wt% of PE-alloy loading in the matrix. When loading level of PE-alloy further increased to 10 wt%,

a CA of 104.4 ± 2.7° can be achieved with water droplet repellent property increased as well. This was mainly due to the hydrophobic nature of the synthetic wax additive (PE-alloy) that is lack of polar functional groups.

Water vapor sorption of neat WBEP, GO/WBEP, and PE-alloy/WBEP composite measured on free-standing films was shown in Figure 4.7b.[63] Addition of GO (~1.8 wt%) indicated minor impact on water uptake, while PE-alloy/WBEP composites absorbed ~25% less moisture in comparison with neat polymer. However, increasing PE-alloy loading from 1% to 5% showed minor reduction of water uptake.

4.4.4 Study of Coating Impedance by EIS

Bode magnitude, phase, and Nyquist plots obtained from salt solution immersion test of different time intervals were shown in Figure 4.8. The initial total impedance at low-frequency (0.01 Hz) for single- and bilayer coatings was ~0.9×10^{10} and ~1.1×10^{10} (ohm cm^2), respectively, indicating high resistance towards the electrolyte solution.[13] During the first 24 h of immersion, total impedance dropped quickly for both coatings, which was down to ~2×10^9 and ~8×10^9 (ohm cm^2) for single- and bilayer coatings, respectively. The decrease of impedance was then slowed down until day-45 for single-layer coating, when a more drastic change (~2×10^8 ohm cm^2) occurred. On the contrary, the total impedance of bilayer coating during this same period until day-64 decreased steadily to ~2×10^9 (ohm cm^2), which was ten times above the impedance of single-layer coating. The total impedance of both coatings exhibited minor changes at high frequency range (10^2–10^5 Hz) with a phase angle close to 85° within the whole immersion period.[64]
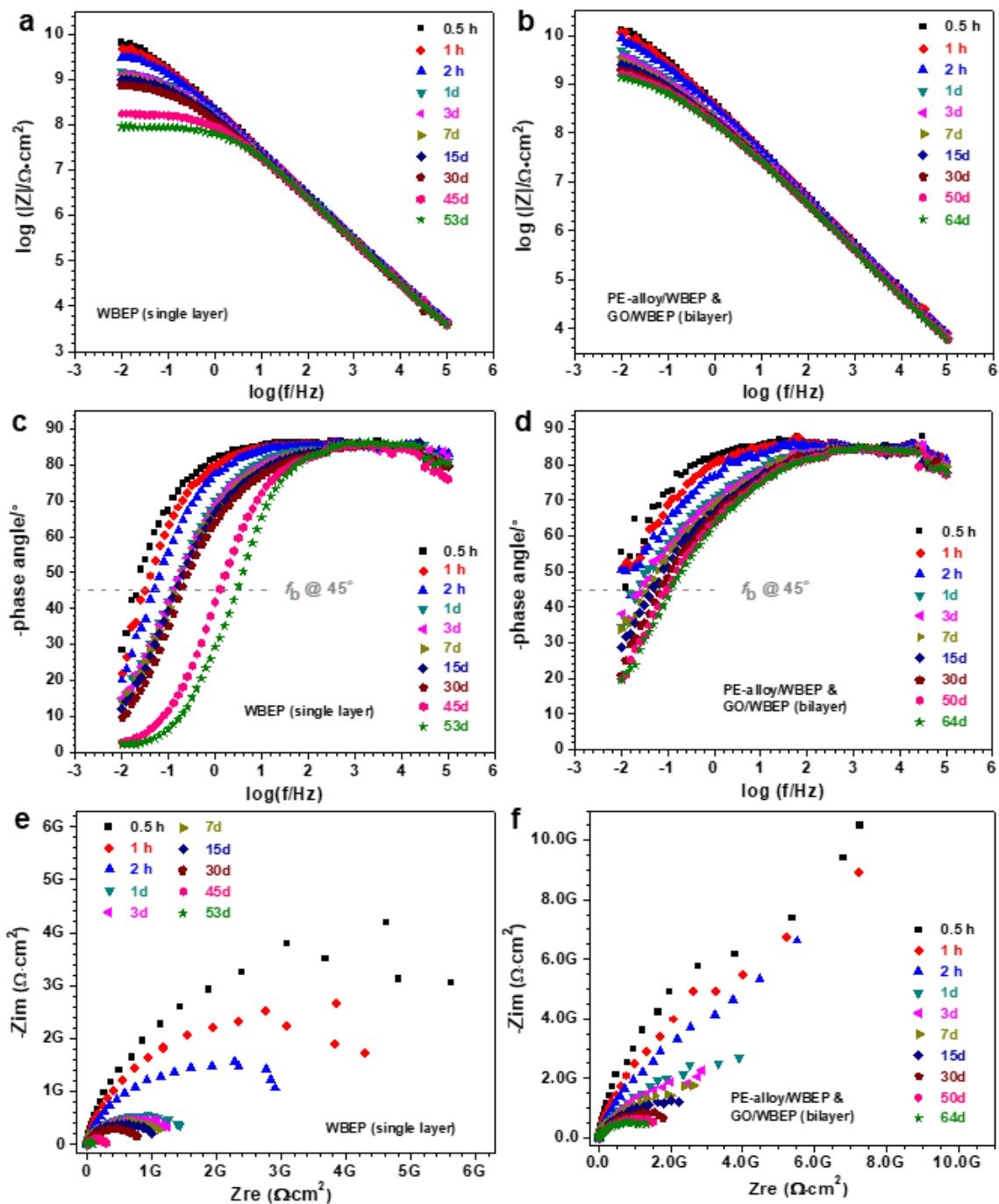
Figure 4.8 (a, b) Bode magnitude, (c, d) phase and (e, f) Nyquist plots of single-layer WBEP and bilayer PE-5%/WBEP (top) with GO-1.8%/WBEP (primer) composite coatings.

Microscopic delamination of organic coatings at the coating/metal interface can reflect their barrier properties towards water and electrolyte solution, and is important to study the underwater resistance of anticorrosive coatings. The delamination area can be calculated by the breakpoint frequency (f_b at a 45° phase angle) obtained from Bode phase plots.[13] Thus, the electrochemical performance of metal/coating systems can be studied from breakpoint frequency in the EIS spectra.

Figure 4.9 Breakpoint frequency (f_b) of single-layer WBEP and bilayer PE-5%/WBEP (top) with GO-1.8%/WBEP (primer) composite coatings at different time intervals.

Breakpoint frequency (f_b) is correlated with the relative increase of electrochemical active surface area (Equation 1), which is attributed to increased delaminated area with increased immersion time.[13] In addition, the surface coating porosity, the reaction of

metal/coating interface, and other relevant electrochemical information can be obtained by analyzing f_b that is varied with immersion time.

$$f_b = K \left(\frac{A_t}{A_0} \right) \tag{1}$$

In this expression, $K = (1/2)\rho\varepsilon\varepsilon_0$, A_t is delaminated area, A_0 is the total area of the sample, ρ is resistivity of coating, ε is dielectric constant of water in coating, and ε_0 is the vacuum permittivity. The value of ρ declines and the value of ε increases correspondingly when electrolytes penetrates the coating with water, resulting in a compensated effect that keeps K almost unchanged. Hence, the delaminated area of the coating system is regarded as approximately proportional to breakpoint frequency.

In general, the higher the f_b, the more delaminated area at the metal interface. f_b is functional with high frequency data, and thus it did not need to take too much time to gain the low frequency data. Hence, breakpoint frequency can be regarded as a simple and rapid method to evaluate the electrochemical performance of the metal/coating system. As shown in Figure 4.9, f_b of both coatings shifted to higher frequencies with increased immersion time, indicating the deterioration of barrier property of coatings. However, f_b of the bilayer coating started lower and increased much slower in comparison with f_b of the single-layer coating, indicating better water/electrolyte solution and underwater corrosion resistance.[13]
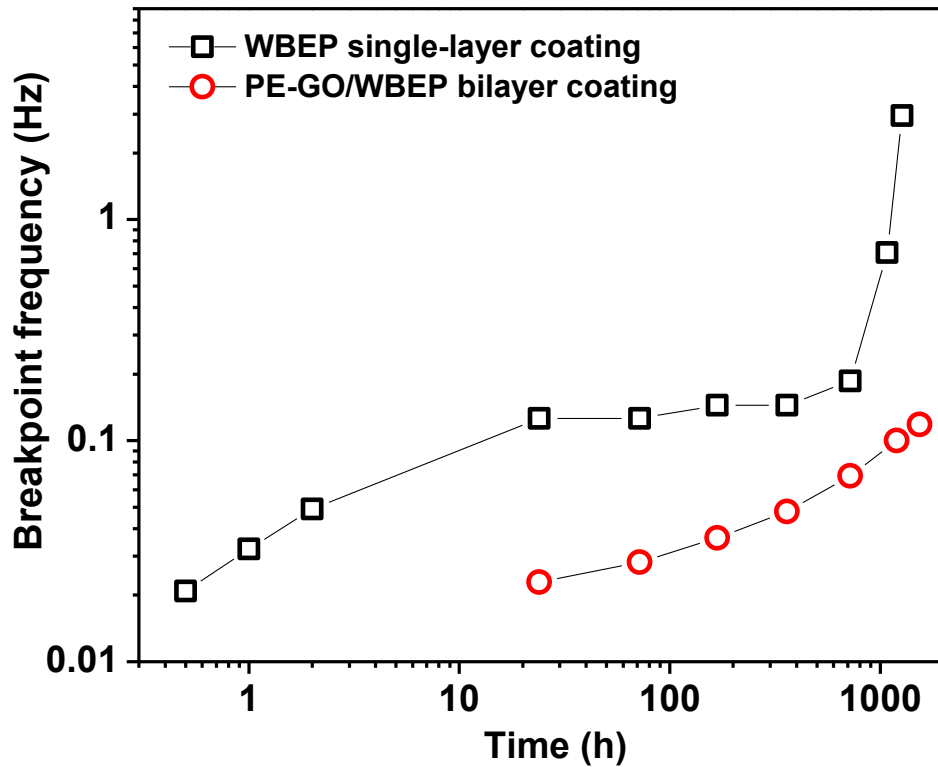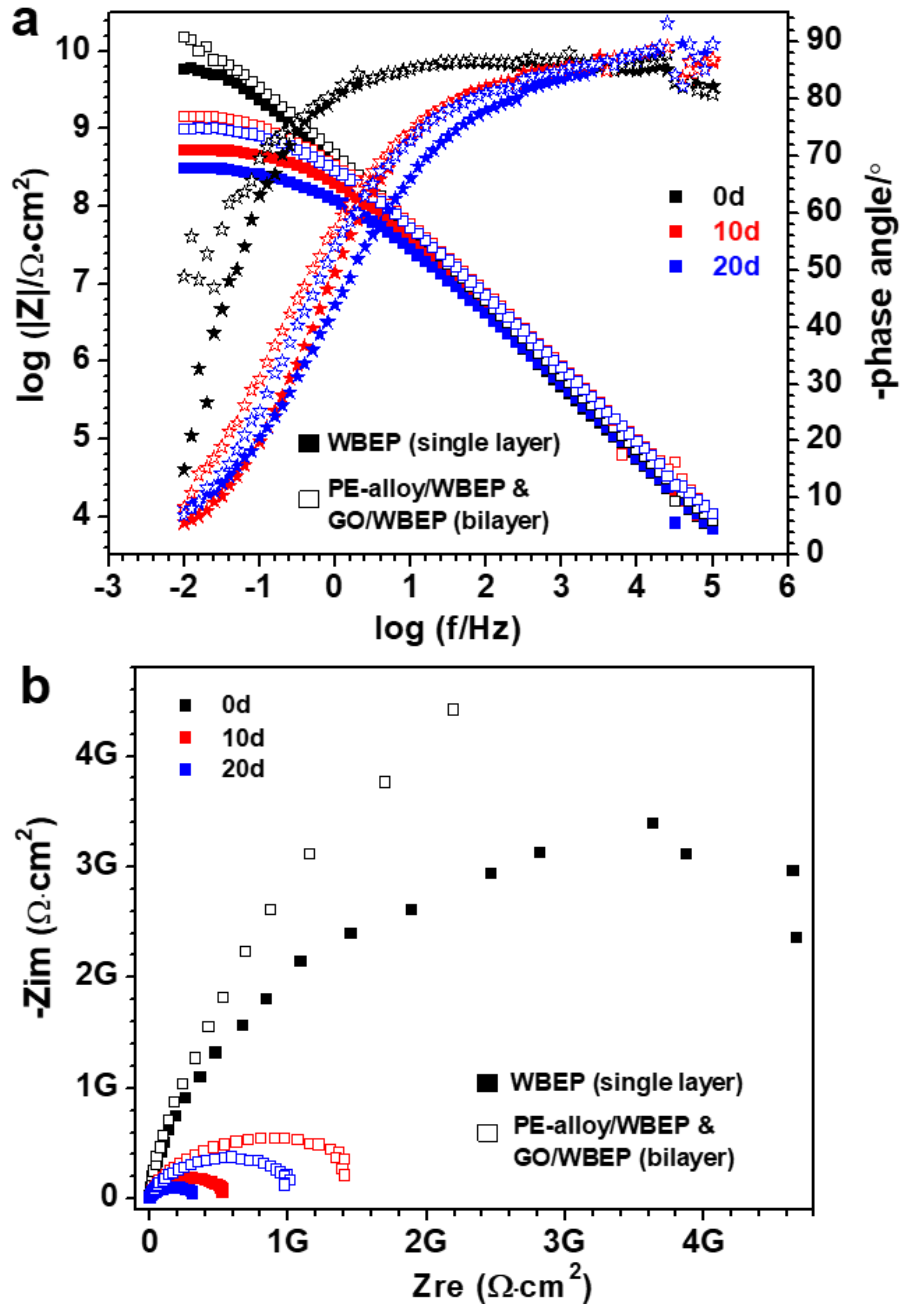
Figure 4.10 Bode magnitude (■) and phase (★) plots (a), and Nyquist plots (b) of single-layer (■) WBEP and bilayer (□) PE-5%/WBEP (top) with GO-1.8%/WBEP (primer) composite coatings after different time interval of exposure.

Nyquist plots indicated that high resistance and low capacitance for both coatings at the beginning of the immersion, and the total impedance gradually decreased with increasing immersion time. As the immersion time elapsed, barrier property of organic

118

coatings decreased with extending penetrations of water and electrolytes by three ways: water sorption, transportation in the coating, and water ingress at the coating/metal interface.[3] The bilayer coating contains a hydrophobic component that could reduce water sorption on the surface as shown by the increased water contact angle (Figure 4.7a). Because a coating with greater hydrophobicity usually exhibits higher underwater resistance due to the potential decrease of wettability coupled with the penetration of aggressive electrolyte, leading to improved corrosion resistance under prolonged immersion time.

Outdoor environments can be classified into three major categories according to corrosive aggressiveness, which are immersion, atmospheric, and splash zone with some subgroups.[65] The splash zone exposure is extremely aggressive in comparison with the other two due to a combination of high O_2 content in the air with continuous salt splashing from sea, which can be simulated in a salt fog humidity chamber in lab.[4] Therefore, coating impedance deterioration under such exposure condition was also investigated at different exposure time interval in addition to conventional immersion test. Figure 4.10a displayed the Bode magnitude and phase plots of single- and bilayer coatings, represented with a close- and open-square symbol, respectively. It was observed that both coatings exhibited faster decrease of the total impedance value at low-frequency (0.01 Hz) during salt spray exposure than immersion condition. One reason is that the physical state of water (liquid and gaseous) showed an impact on permeation property, as the average molecular velocity of vapor is much higher than that of liquid state water.[20] Additionally, capillary effect that inhibits the permeation liquid water is not capable of restricting the transmission of water vapor, thereby resulting in faster water ingress in

organic coatings.[20] The breakpoint frequencies for single- and bilayer coatings after day-20 exposure were 0.778 and 0.485, respectively. Nyquist plots of single- and bilayer coatings in Figure 4.10b indicated higher impedance value for the later at each of the time intervals during salt spray exposure, indicating the better water/electrolyte solution resistance of the bilayer coatings.

4.4.5 Coating Delamination Study on Steel Substrate with Scribe Defect

Steel is the most important industrial metal that is subjected to heavy corrosion when exposed to humid air. For the corrosion of steel (iron) under normal conditions (as shown in Figure 4.11): O_2 from the air is reduced in cathodic reaction with the formation of hydroxide anions (OH^-); while metal is dissolved by giving out electrons to become a ferrous cation (Fe^{2+}) in anodic reaction. Besides, intermediate products such as peroxides, superoxides and radicals are also generated during the cathodic reduction process, but anodic reaction is almost universal.[17, 66-67] Fe^{2+} accumulated at the anodic sites will then react with the OH^- from solution to form iron hydroxide, which will be quickly oxidized into ferrous oxides, a green hydrated magnetite with this formulation: $FeO \cdot Fe_2O_3 \cdot H_2O$ (Eq. 6).[66] The unstable hydrated magnetite will then decompose into the relatively stable black magnetite $FeO \cdot Fe_2O_3$ (Eq. 7).[5] Furthermore, with excess oxygen in the system, the black magnetite will subsequently be oxidized into dark-red hydrated hematite $Fe_2O_3 \cdot H_2O$, which is more stable, also known as rust.[66] The overall reaction for the rust formation can be rewritten into Eq. (2).

$$12Fe(s) + 9O_2(g) + 6H_2O(l) \rightarrow 6Fe_2O_3 \cdot H_2O(s) \tag{2}$$
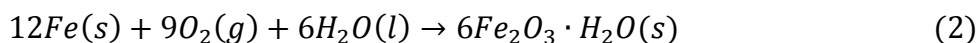
Corrosion of Coated Steel with a Scribe Defect
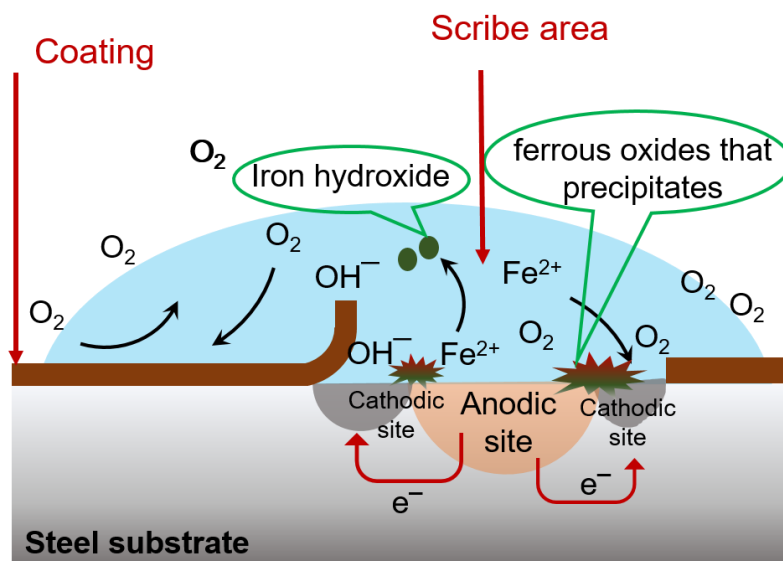
Figure 4.11 Corrosion of steel (iron) in the presence of O_2, H_2O and electrolytes.

An external defect, such as a scribe by razor blade, can occur on anticorrosive coating, which could have a significant impact on corrosion resistant performance due to exposure of metal/coating interfaces. Compared with intact coating, corrosion can proceed much quicker to cause failure due to coating delamination, which is induced by water ingress at the defect site. When coated steel samples were exposed to salt water (3.5% NaCl immersion condition), corrosion initiates quickly from the exposed region with coating delamination expanding radiantly from the scribe, as shown in Figure 4.11. The three columns in Figure 4.12a display the corrosion morphologies of steel coated with single-layer WBEP, PE-alloy-5%/WBEP composite, and bilayer composite coatings, respectively. The single-layer coating with PE-alloy incorporated exhibited reduced corrosion, however, it failed to maintain adhesion and delaminated completely form the substrate. On the contrary, bilayer coating that was away from the scribe was able to maintain its adhesion better than the other two coating systems.

The results from salt spray exposure test (following the ASTM B1 17 specified condition) of the same coating series on steel are shown in Figure 4.12b. The salt spray exposure test result shows similar trend as that of immersion test, except for single-layer coating with 5% PE-alloy incorporated surprisingly performed worse with faster corrosion propagating and coating delamination even than the neat sample. On the other hand, bilayer coating that contained the layer of GO/WBEP (1.8% GO) composite exhibited a better ability to maintain coating adhesion, by which the regime with a certain distance from the scribe can still be protected from environmental contamination. One reason for coating delamination by corrosion reaction is due to the formation of OH^- and increasing of local pH at the cathodic sites, where bonding interactions between a coating binder and metal substrate are disturbed. Glover and coworkers reported a strong correlation between reduced delamination rate and the rate of oxygen permeation on graphene pigmented anticorrosive coatings.[68] Previous study on steel corrosion by Wroblowa suggested that the formation of stable peroxyl ions during oxygen reduction process can be highly aggressive or even destructive to organic materials. These active intermediate species can attack the interface and covalent bonds in a polymer binder to potentially induce coating delamination.[17] Therefore, with a prominent reduction on measured O_2 permeability, bilayer coating with GO addition outperformed the other two systems under both conditions. Besides, the difference on performance became more prominent under splash exposure condition, where higher concentration of oxygen was involved in comparison with the immersion environment.

a

3day   3day   3day

7day   7day   7day

Coating completely delaminated

7day   7day   7day

Single-layer WBEP on QD36 steel   Single-layer PE/WBEP on QD36 steel   Bilayer PE/WBEP GO/WBEP (primer) on QD36 steel

b

72h   72h   72h

120h   120h   120h

Single-layer WBEP on QD36 steel   Single-layer PE/WBEP on QD36 steel   Bilayer PE/WBEP GO/WBEP (primer) on QD36 steel
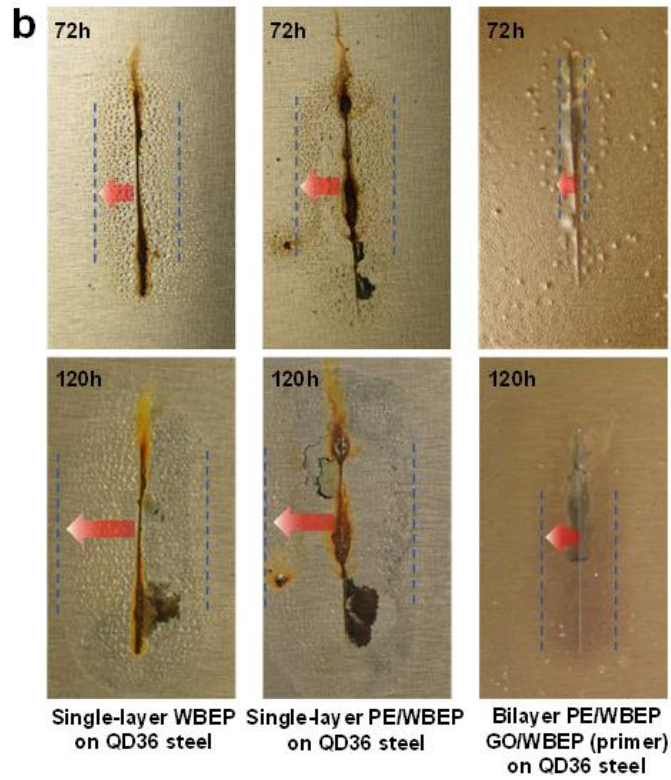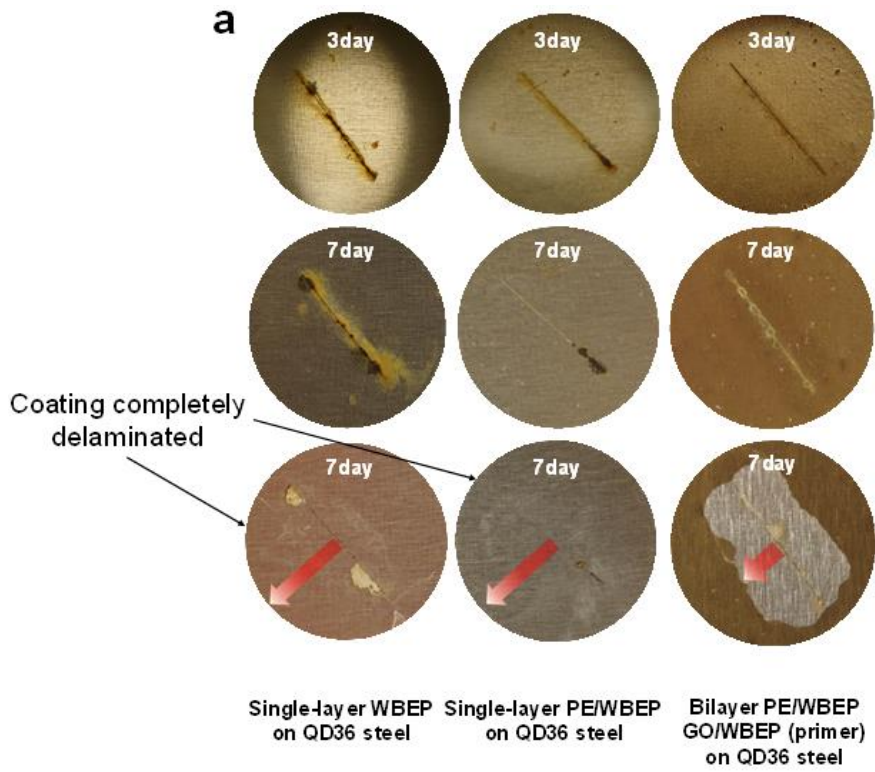
Figure 4.12 Digital photo images of salt spray exposure test on coated steel.

4.5 Conclusion

In summary, single-layer coating of waterborne epoxy-amine resin and its bilayer composite coating with hydrophobic PE-alloy and lamellar graphene oxide functional fillers were thoroughly investigated for their anticorrosion performance under different environmental conditions. Anticorrosive coating system with hydrophobic surface and enhanced oxygen barrier property was obtained and characterized by increased water contact angle and decreased oxygen gas permeability. Electrochemical impedance spectroscopy study indicated increased coating impedance of the bilayer coating under both immersion and simulated splash environmental conditions. Water ingress at the metal/coating interface could be a major cause of coating delamination, however, our study indicated that oxygen content also plays a key role during this process, although the actual mechanism was still not fully understood. The future work will be on elucidating the mechanism and modeling of coating delamination coupled with corrosion propagation at a molecular level, which will provide fundamental guidance for the design of novel anticorrosive coatings.

4.6 Reference

1.   Li, X.; Zhang, D.; Liu, Z.; Li, Z.; Du, C.; Dong, C., Materials science: Share corrosion data. *Nature* **2015,** *527* (7579), 441-2.
2.   Koch, G. H.; Research, U. S. F. H. A. O. o. I.; Development; Laboratories, C. T.; Center, T.-F. H. R.; International, N., *Corrosion cost and preventive strategies in the United States*. Turner-Fairbank Highway Research Center: 2002.
3.   Dickie, R. A.; Floyd, F. L., Polymeric Materials for Corrosion Control: An Overview. In *Polymeric Materials for Corrosion Control*, American Chemical Society: 1986; Vol. 322, pp 1-16.
4.   Landolt, D., *Corrosion and Surface Chemistry of Metals*. EFPL Press: 2007.
5.   Sørensen, P. A.; Kiil, S.; Dam-Johansen, K.; Weinell, C. E., Anticorrosive coatings: a review. *Journal of Coatings Technology and Research* **2009,** *6* (2), 135-176.

6.   van Westing, E. P. M.; Ferrari, G. M.; Geenen, F. M.; de Wit, J. H. W., In situ determination of the loss of adhesion of barrier epoxy coatings using electrochemical impedance spectroscopy. *Progress in Organic Coatings* **1993,** *23* (1), 89-103.

7.   Funke, W., Thin-layer technology in organic coatings. *Progress in Organic Coatings* **1996,** *28* (1), 3-7.

8.   Rammelt, U.; Reinhard, G., Characterization of active pigments in damage of organic coatings on steel by means of electrochemical impedance spectroscopy. *Progress in Organic Coatings* **1994,** *24* (1), 309-322.

9.   Bonora, P. L.; Deflorian, F.; Fedrizzi, L., Electrochemical impedance spectroscopy as a tool for investigating underpaint corrosion. *Electrochimica Acta* **1996,** *41* (7), 1073-1082.

10.   Sekine, I., Recent evaluation of corrosion protective paint films by electrochemical methods. *Progress in Organic Coatings* **1997,** *31* (1), 73-80.

11.   Wang, S. X.; Lin, W. W.; Ceng, S. A.; Zhang, J. Q., Corrosion Inhibition of Reinforcing Steel by Using Acrylic Latex 11Communicated by D.M. Roy. *Cement and Concrete Research* **1998,** *28* (5), 649-653.

12.   Sekine, I.; Yuasa, M.; Hirose, N.; Tanaki, T., Degradation evaluation of corrosion protective coatings by electrochemical, physicochemical and physical measurements. *Progress in Organic Coatings* **2002,** *45* (1), 1-13.

13.   Liu, X.; Xiong, J.; Lv, Y.; Zuo, Y., Study on corrosion electrochemical behavior of several different coating systems by EIS. *Progress in Organic Coatings* **2009,** *64* (4), 497-503.

14.   Zhou, C.; Lu, X.; Xin, Z.; Liu, J.; Zhang, Y., Hydrophobic benzoxazine-cured epoxy coatings for corrosion protection. *Progress in Organic Coatings* **2013,** *76* (9), 1178-1183.

15.   Zanni-Deffarges, M. P.; Shanahan, M. E. R., Diffusion of water into an epoxy adhesive: comparison between bulk behaviour and adhesive joints. *International Journal of Adhesion and Adhesives* **1995,** *15* (3), 137-142.

16.   Zhou, J.; Lucas, J. P., Hygrothermal effects of epoxy resin. Part I: the nature of water in epoxy. *Polymer* **1999,** *40* (20), 5505-5512.

17.   Wroblowa, H. S., Intermediate products of atmospheric oxygen reduction and the integrity of metal—organic coating interface. *Journal of Electroanalytical Chemistry* **1992,** *339* (1), 31-40.

18.   Scantlebury, D., The dynamic nature of underfilm corrosion. *Corrosion Science* **1993,** *35* (5), 1363-1366.

19.   Gurumurthy, C. K.; Kramer, E. J.; Hui, C.-Y., Water-assisted sub-critical crack growth along an interface between polyimide passivation and epoxy underfill. *International Journal of Fracture* **2001,** *109* (1), 1-28.

20.   Sangaj, N. S.; Malshe, V. C., Permeability of polymers in protective organic coatings. *Progress in Organic Coatings* **2004,** *50* (1), 28-39.

21.   Liu, B.; Fang, Z.-g.; Wang, H.-b.; Wang, T., Effect of cross linking degree and adhesion force on the anti-corrosion performance of epoxy coatings under simulated deep sea environment. *Progress in Organic Coatings* **2013,** *76* (12), 1814-1818.

22.   Posner, R.; Wapner, K.; Amthor, S.; Roschmann, K. J.; Grundmeier, G., Electrochemical investigation of the coating/substrate interface stability for styrene/acrylate copolymer films applied on iron. *Corrosion Science* **2010,** *52* (1), 37-44.

23.   Bierwagen, G. P., Reflections on corrosion control by organic coatings. *Progress in Organic Coatings* **1996,** *28* (1), 43-48.

24.   Brooman, E. W., Modifying organic coatings to provide corrosion resistance: Part II—Inorganic additives and inhibitors. *Metal Finishing* **2002,** *100* (5), 42-53.

25.   Perera, D. Y., Effect of pigmentation on organic coating characteristics. *Progress in Organic Coatings* **2004,** *50* (4), 247-262.

26.   Curtzwiler, G. W.; Williams, E. B.; Maples, A. L.; Wand, S. W.; Rawlins, J. W., Measurable and Influential Parameters That Influence Corrosion Performance Differences between Multiwall Carbon Nanotube Coating Material Combinations and Model Parent Material Combinations Derived from Epoxy-Amine Matrix Materials. *ACS Applied Materials & Interfaces* **2017,** *9* (7), 6356-6368.

27.   Ejenstam, L.; Swerin, A.; Pan, J.; Claesson, P. M., Corrosion protection by hydrophobic silica particle-polydimethylsiloxane composite coatings. *Corrosion Science* **2015,** *99*, 89-97.

28.   Nine, M. J.; Cole, M. A.; Tran, D. N. H.; Losic, D., Graphene: a multipurpose material for protective coatings. *Journal of Materials Chemistry A* **2015,** *3* (24), 12580-12602.

29.   Kang, D.; Kwon, J. Y.; Cho, H.; Sim, J.-H.; Hwang, H. S.; Kim, C. S.; Kim, Y. J.; Ruoff, R. S.; Shin, H. S., Oxidation Resistance of Iron and Copper Foils Coated with Reduced Graphene Oxide Multilayers. *ACS Nano* **2012,** *6* (9), 7763-7769.

30.   Prasai, D.; Tuberquia, J. C.; Harl, R. R.; Jennings, G. K.; Bolotin, K. I., Graphene: Corrosion-Inhibiting Coating. *ACS Nano* **2012,** *6* (2), 1102-1108.

31.   Novoselov, K. S.; Falko, V. I.; Colombo, L.; Gellert, P. R.; Schwab, M. G.; Kim, K., A roadmap for graphene. *Nature* **2012,** *490* (7419), 192-200.

32.   Compton, O. C.; Kim, S.; Pierre, C.; Torkelson, J. M.; Nguyen, S. T., Crumpled Graphene Nanosheets as Highly Effective Barrier Property Enhancers. *Advanced Materials* **2010,** *22* (42), 4759-4763.

33.   Bunch, J. S.; Verbridge, S. S.; Alden, J. S.; van der Zande, A. M.; Parpia, J. M.; Craighead, H. G.; McEuen, P. L., Impermeable Atomic Membranes from Graphene Sheets. *Nano Letters* **2008,** *8* (8), 2458-2462.

34.   Sun, W.; Wang, L.; Wu, T.; Wang, M.; Yang, Z.; Pan, Y.; Liu, G., Inhibiting the Corrosion-Promotion Activity of Graphene. *Chemistry of Materials* **2015,** *27* (7), 2367-2373.

35.   Mao, H. Y.; Laurent, S.; Chen, W.; Akhavan, O.; Imani, M.; Ashkarran, A. A.; Mahmoudi, M., Graphene: Promises, Facts, Opportunities, and Challenges in Nanomedicine. *Chemical Reviews* **2013,** *113* (5), 3407-3424.

36.   Paredes, J. I.; Villar-Rodil, S.; Martínez-Alonso, A.; Tascón, J. M. D., Graphene Oxide Dispersions in Organic Solvents. *Langmuir* **2008,** *24* (19), 10560-10564.

37.   Dreyer, D. R.; Park, S.; Bielawski, C. W.; Ruoff, R. S., The chemistry of graphene oxide. *Chemical Society Reviews* **2010,** *39* (1), 228-240.

38.   Krishnamoorthy, K.; Jeyasubramanian, K.; Premanathan, M.; Subbiah, G.; Shin, H. S.; Kim, S. J., Graphene oxide nanopaint. *Carbon* **2014,** *72*, 328-337.

39.   Su, Y.; Kravets, V. G.; Wong, S. L.; Waters, J.; Geim, A. K.; Nair, R. R., Impermeable barrier films and protective coatings based on reduced graphene oxide. *Nature Communication* **2014,** *5*, 4843.

40.   Richard Prabakar, S. J.; Hwang, Y.-H.; Bae, E. G.; Lee, D. K.; Pyo, M., Graphene oxide as a corrosion inhibitor for the aluminum current collector in lithium ion batteries. *Carbon* **2013,** *52*, 128-136.

41.   Ramezanzadeh, B.; Ahmadi, A.; Mahdavian, M., Enhancement of the corrosion protection performance and cathodic delamination resistance of epoxy coating through treatment of steel substrate by a novel nanometric sol-gel based silane composite film filled with functionalized graphene oxide nanosheets. *Corrosion Science* **2016,** *109*, 182-205.

42.   Yu, Z.; Lv, L.; Ma, Y.; Di, H.; He, Y., Covalent modification of graphene oxide by metronidazole for reinforced anti-corrosion properties of epoxy coatings. *RSC Advances* **2016,** *6* (22), 18217-18226.

43.   Qi, K.; Sun, Y.; Duan, H.; Guo, X., A corrosion-protective coating based on a solution-processable polymer-grafted graphene oxide nanocomposite. *Corrosion Science* **2015,** *98*, 500-506.

44.   Boinovich, L. B.; Gnedenkov, S. V.; Alpysbaeva, D. A.; Egorkin, V. S.; Emelyanenko, A. M.; Sinebryukhov, S. L.; Zaretskaya, A. K., Corrosion resistance of composite coatings on low-carbon steel containing hydrophobic and superhydrophobic layers in combination with oxide sublayers. *Corrosion Science* **2012,** *55*, 238-245.

45.   Zhou, C.; Lu, X.; Xin, Z.; Liu, J., Corrosion resistance of novel silane-functional polybenzoxazine coating on steel. *Corrosion Science* **2013,** *70*, 145-151.

46.   Zhang, D.; Wang, L.; Qian, H.; Li, X., Superhydrophobic surfaces for corrosion protection: a review of recent progresses and future directions. *Journal of Coatings Technology and Research* **2016,** *13* (1), 11-29.

47.   Yang, Z.; Wang, L.; Sun, W.; Li, S.; Zhu, T.; Liu, W.; Liu, G., Superhydrophobic epoxy coating modified by fluorographene used for anti-corrosion and self-cleaning. *Appl Surf Sci* **2017,** *401*, 146-155.

48.   Schoff, C. K., Organic coatings: the paradoxical materials. *Progress in Organic Coatings* **2005,** *52* (1), 21-27.

49.   Liu, M.; Mao, X.; Zhu, H.; Lin, A.; Wang, D., Water and corrosion resistance of epoxy–acrylic–amine waterborne coatings: Effects of resin molecular weight, polar group and hydrophobic segment. *Corrosion Science* **2013,** *75*, 106-113.

50.   Gao, J.; Lv, H.; Zhang, X.; Zhao, H., Synthesis and properties of waterborne epoxy acrylate nanocomposite coating modified by MAP-POSS. *Progress in Organic Coatings* **2013,** *76* (10), 1477-1483.

51.   Zhou, C.; Lu, X.; Xin, Z.; Liu, J.; Zhang, Y., Polybenzoxazine/SiO2 nanocomposite coatings for corrosion protection of mild steel. *Corrosion Science* **2014,** *80*, 269-275.

52.   Rammelt, U.; Reinhard, G., Application of electrochemical impedance spectroscopy (EIS) for characterizing the corrosion-protective performance of organic coatings on metals. *Progress in Organic Coatings* **1992,** *21* (2), 205-226.

53.   van Westing, E. P. M.; Ferrari, G. M.; De Wit, J. H. W., The determination of coating performance using electrochemical impedance spectroscopy. *Electrochimica Acta* **1994,** *39* (7), 899-910.

54.   Zhang, D.; Qian, H.; Wang, L.; Li, X., Comparison of barrier properties for a superhydrophobic epoxy coating under different simulated corrosion environments. *Corrosion Science* **2016,** *103*, 230-241.

55.   Guan, Y.; Meyers, K. P.; Mendon, S. K.; Hao, G.; Douglas, J. R.; Trigwell, S.; Nazarenko, S. I.; Patton, D. L.; Rawlins, J. W., Ecofriendly Fabrication of Modified Graphene Oxide Latex Nanocomposites with High Oxygen Barrier Performance. *ACS Applied Materials & Interfaces* **2016,** *8* (48), 33210-33220.

56.   Gulmine, J. V.; Janissek, P. R.; Heise, H. M.; Akcelrud, L., Polyethylene characterization by FTIR. *Polymer Testing* **2002,** *21* (5), 557-563.

57.   Pourhashem, S.; Vaezi, M. R.; Rashidi, A.; Bagherzadeh, M. R., Exploring corrosion protection properties of solvent based epoxy-graphene oxide nanocomposite coatings on mild steel. *Corrosion Science* **2017,** *115*, 78-92.

58.   Cançado, L. G.; Jorio, A.; Ferreira, E. H. M.; Stavale, F.; Achete, C. A.; Capaz, R. B.; Moutinho, M. V. O.; Lombardo, A.; Kulmala, T. S.; Ferrari, A. C., Quantifying Defects in Graphene via Raman Spectroscopy at Different Excitation Energies. *Nano Letters* **2011,** *11* (8), 3190-3196.

59.   Ferrari, A. C.; Robertson, J., Interpretation of Raman spectra of disordered and amorphous carbon. *Physical Review B* **2000,** *61* (20), 14095-14107.

60.   Nyquist, R. A., *Interpreting Infrared, Raman, and Nuclear Magnetic Resonance Spectra*. Academic Press: 2001.

61.   Cui, Y.; Kundalwal, S. I.; Kumar, S., Gas barrier performance of graphene/polymer nanocomposites. *Carbon* **2016,** *98*, 313-333.

62.   Farris, S.; Introzzi, L.; Biagioni, P.; Holz, T.; Schiraldi, A.; Piergiovanni, L., Wetting of Biopolymer Coatings: Contact Angle Kinetics and Image Analysis Investigation. *Langmuir* **2011,** *27* (12), 7563-7574.

63.   Liu, Y.; Soer, W.-J.; Scheerder, J.; Satgurunathan, G.; Keddie, J. L., Water Vapor Sorption and Diffusion in Secondary Dispersion Barrier Coatings: A Critical Comparison with Emulsion Polymers. *ACS Applied Materials & Interfaces* **2015,** *7* (22), 12147-12157.

64.   Zheng, H.; Shao, Y.; Wang, Y.; Meng, G.; Liu, B., Reinforcing the corrosion protection property of epoxy coating by using graphene oxide–poly(urea–formaldehyde) composites. *Corrosion Science* **2017,** *123*, 267-277.

65.   ISO 12944.

66.   Watson, T. M.; Coleman, A. J.; Williams, G.; McMurray, H. N., The effect of oxygen partial pressure on the filiform corrosion of organic coated iron. *Corrosion Science* **2014,** *89*, 46-58.

67.   Wroblowa, H. S.; Qaderi, S. B., Mechanism and kinetics of oxygen reduction on steel. *Journal of Electroanalytical Chemistry and Interfacial Electrochemistry* **1990,** *279* (1), 231-242.

68.   Glover, C. F.; Richards, C.; Baker, J.; Williams, G.; McMurray, H. N., In-coating graphene nano-platelets for environmentally-friendly corrosion protection of iron. *Corrosion Science* **2017,** *114*, 169-172.

CHAPTER V – CONCLUSIONS AND FUTURE WORK

The incorporation of well-dispersed functional nanomaterials in polymeric materials for barrier enhancement has proved to be highly efficient and hold great potential for applications in surface protective coatings. In this work, carbon-based 2D nanomaterial GO was highlighted for its excellent oxygen barrier property in organic anticorrosive coatings. Besides, surface modification protocols of GO were also investigated to extend its utilizations in various polymer matrices by manipulating surface wettability and solvent dispersibility. Moreover, a waterborne coating system with optimized corrosion resistance capability was obtained by preparing a hydrophobic surface in addition to an enhanced oxygen barrier effect, which can endow anticorrosive coatings with increased impedance and reduced delamination under various aggressive environmental conditions.

The first part of this work demonstrated the fabrication of ecofriendly PNCs via aqueous blending of modified GO nanoplatelet with conventional latex copolymers. In this study, partial modification of GO was performed to reduce the moisture sensitivity of the resultant LNCs. LNCs containing mGO absorbed 67% less moisture than LNCs with similar levels of unmodified GO due to fewer hydrophilic moieties on mGO by esterification. Oxygen permeability of LNC with 0.7 vol.% mGO loading exhibited excellent O_2 barrier property (an 84% reduction in comparison with the neat polymer) due to intrinsic impermeability of mGO nanoplatelets with large aspect ratios, sufficient dispersibiltiy and exfoliation in polymer matrix, and alignment of platelets during the film formation process in latex system. Cross-sectional TEM images of LNC films and reduced diffusivity coefficient calculated by data fitting further confirmed that increased

barrier property is due to tortuous pathway effect. However, the unexpected decrease of O$_2$ solubility parameter were also observed, which normally depends only on filler concentration. A possible reason is that the formation of domains in which polymer is trapped by the very large nanoplatelet assemblies and cannot participate in the dynamic permeation process. Therefore, in future work, a direct measurement of gas solubility and determination of free volume of polymer matrix using positron annihilation lifetime spectroscopy will bring a better understanding of the mechanism of this phenomenon.

The second part of this work described a simple and scalable method for producing GO derivatives with flexible solvent condition, high reaction efficiency, and controlled surface property. Specifically, hydrophobically functionalized GO, using small-molecule (hexanoyl chloride) and oligomeric (amine-terminated polyisobutylene, PIB) modifiers, was synthesized and thoroughly characterized spectroscopically and microscopically. Low-density aerogel precursors (LDGOAero) was designed to exhibit increased reactivity in many organic solvents with lower polarity, which normally can not be used to disperse GO materials without the help of extended ultrasonication. Therefore, the hydrophobically modification of GO indicates high efficiency with good stability, and surface property of the resulting GO derivatives were demonstrated by water contact angle and water vapor sorption measurements. Moreover, an ultra-thin coating fabricated on steel substrate with PIB-*g*-GO suspension in cyclohexane exhibited 50 times slower corrosion rate in comparison with unmodified GO thin film coating under salt solution immersion. Future work for this part will include a thorough investigation of polymer-*g*-GO nanocomposites prepared from grafting polymers of different molecular weight and chain structure with varying grafting density. Additionally, corrosion resistance

properties of these nanocomposites thin films will be studied for their applications as novel protective coatings.

In the third study, bilayer anticorrosive coating was prepared from a waterborne coating system by using functional additives/fillers: polyethylene wax (PE-alloy) and GO nanoplatelet. Addition of PE-alloy in the top thin layer successfully improve water repellent property of epoxy-amine resin based waterborne coating and increased corrosion resistance under both aqueous immersion and simulated splash zone conditions, which were demonstrated by increased water contact angle and coating impedance (EIS). On the other hand, incorporation of GO effectively reduces O_2 permeability of coating by $\sim$ 80% with 1.8 wt% of GO loading. Moreover, our study indicated that reduced O_2 content also relates to the coating delamination process, which plays a crucial role on the corrosion resistance ability of defect coating. Future work of this study will be focused on the mechanism of coating delamination with regard to the corrosion reactions, where interfacial bonding of coatings with the substrate are disturbed due to corrosion propagating. Quantitative measurement and computational simulation of interfacial bonding energies will be incorporated to provide a deeper understanding of the procedure, which will be useful for the design of better anticorrosive coatings.
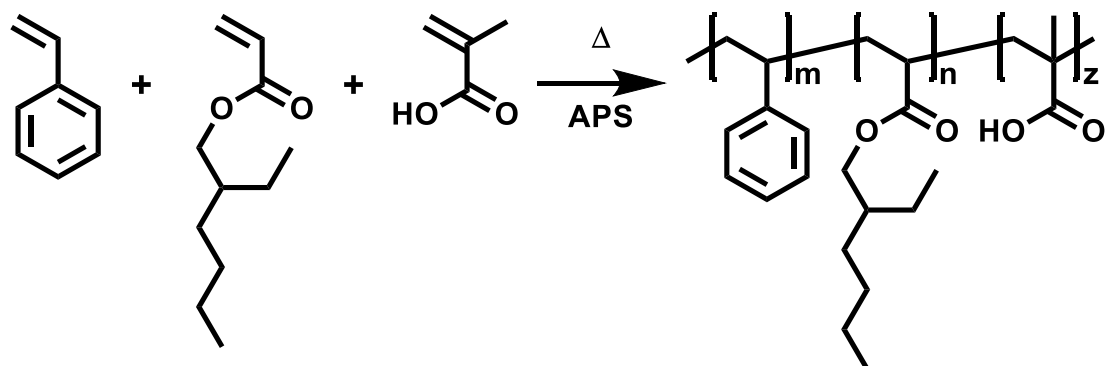
Figure A.1 Synthetic route of the styrene-acrylic latex resin using ammonium persulfate
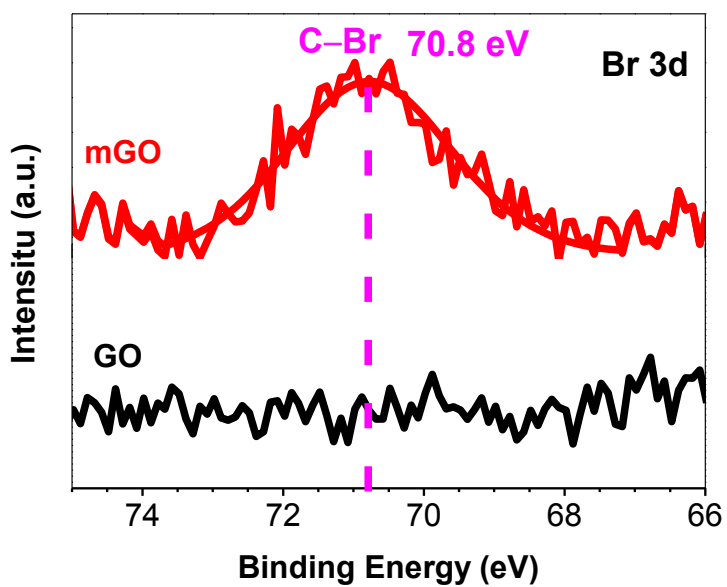
(APS) as the initiator.

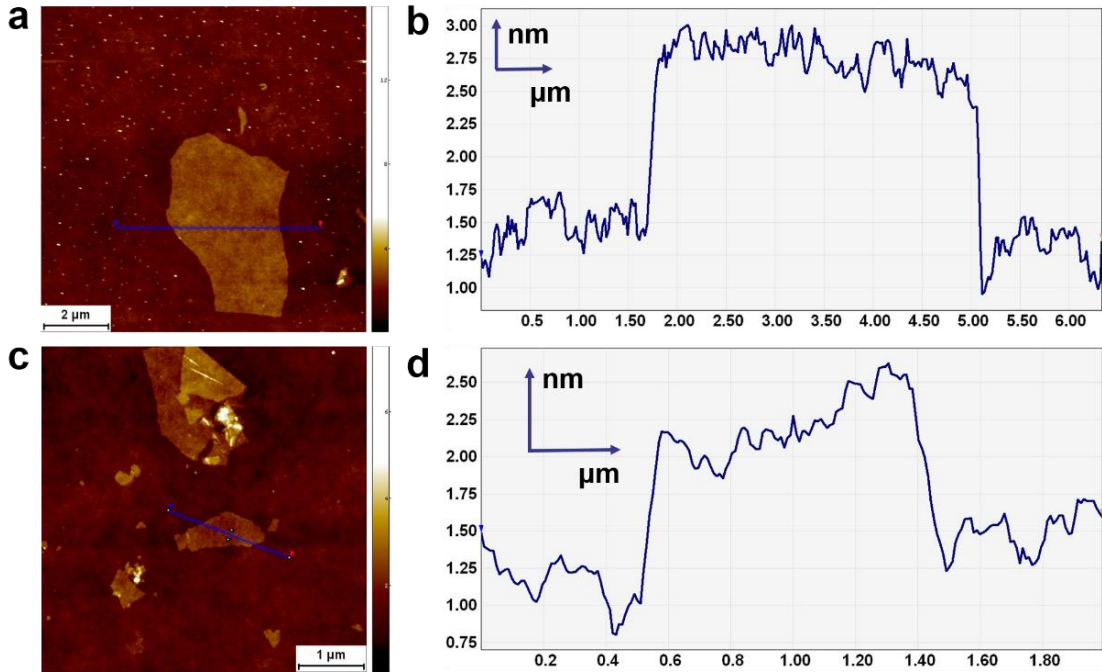Figure A.2 Br 3d XPS spectra of GO and mGO.

Figure A.3 (a) AFM height image and (b) profile of GO. (c) AFM height image and (d) profile of mGO lamellae.
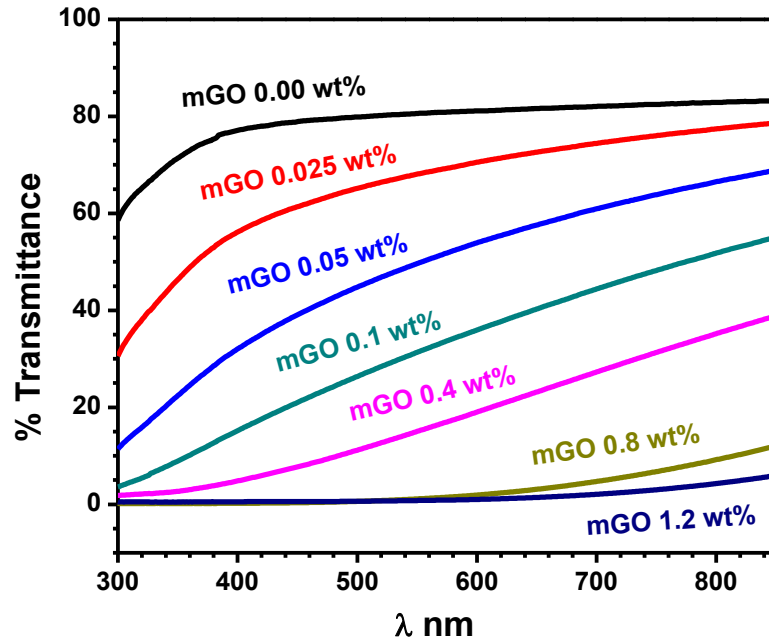

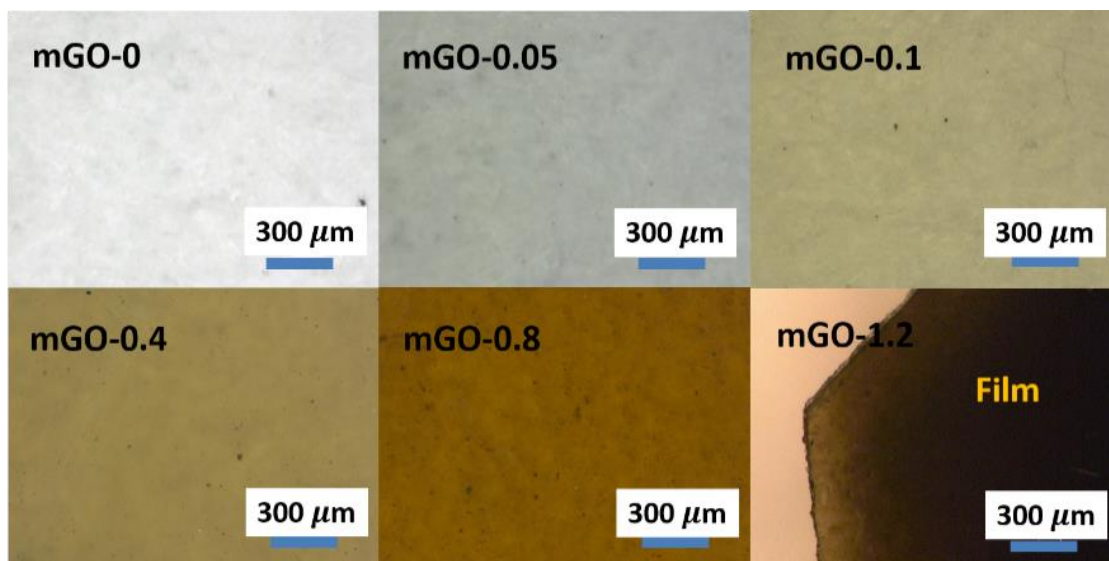Figure A.4 UV-vis spectra of LNC films with different mGO loadings.

Figure A.5 Optical microscope images of LNC films with different mGO loadings.
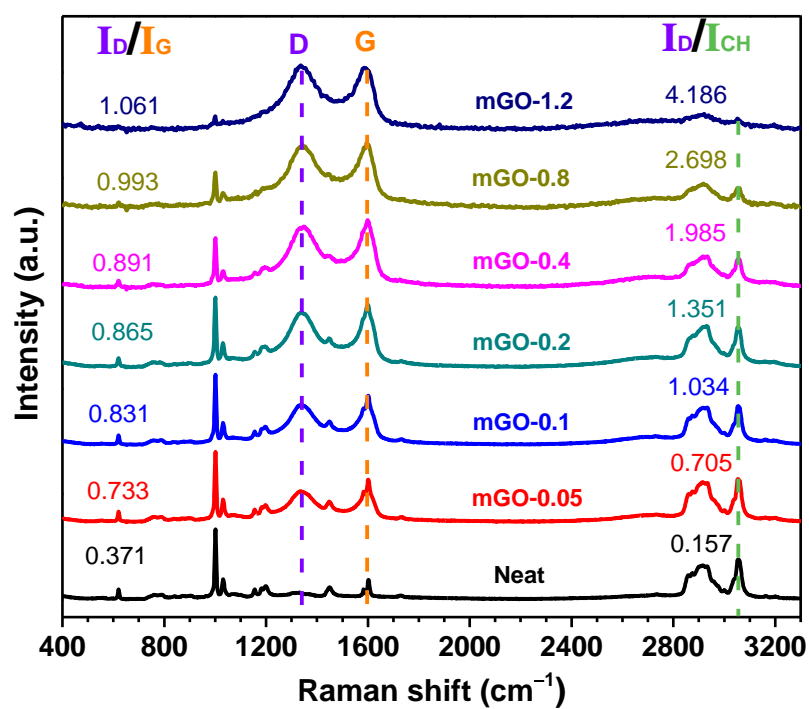

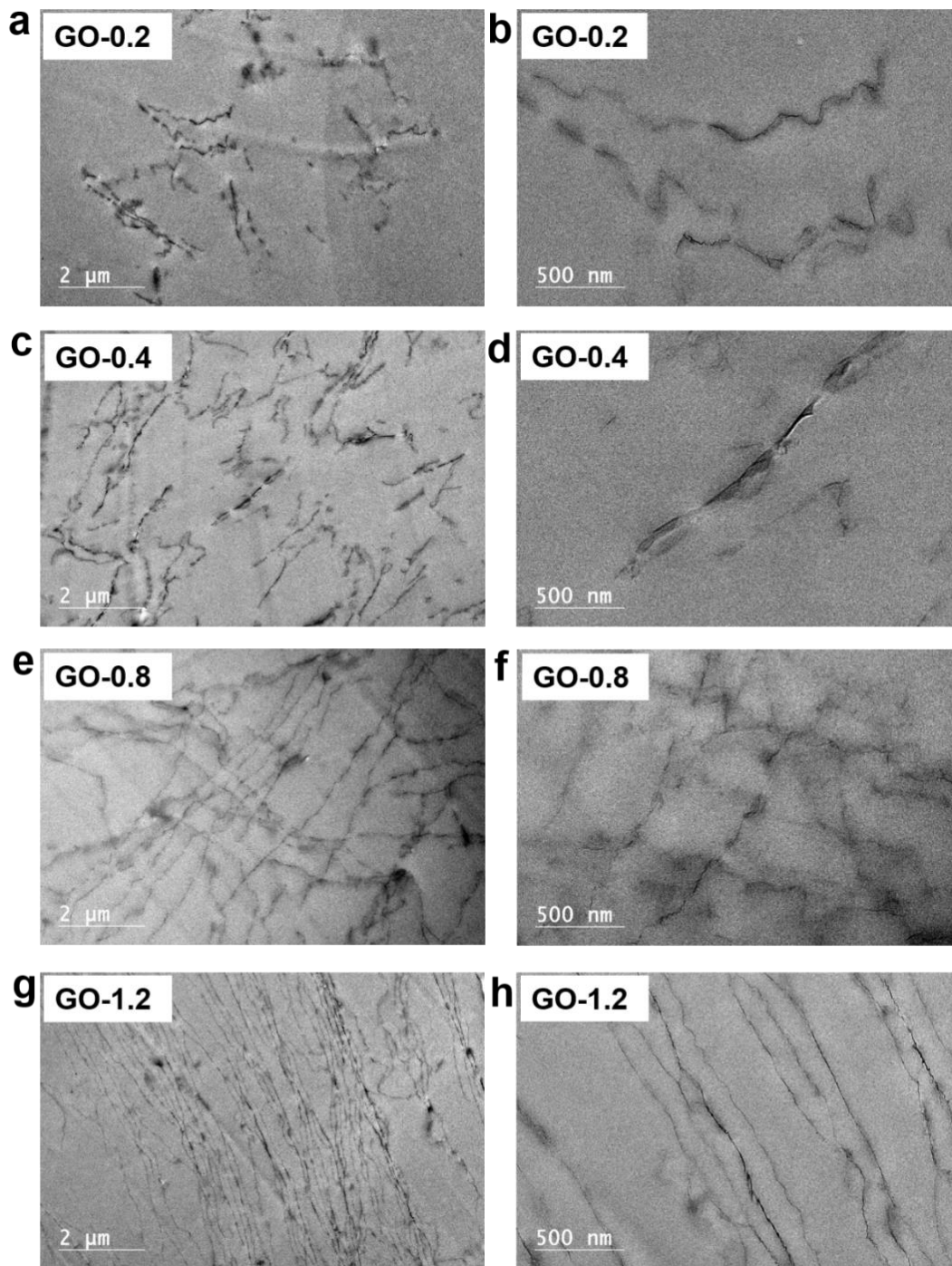Figure A.6 Raman spectra of LNC films with different mGO loadings.

Figure A.7 Cross-sectional TEM images of GO/LNC films with different GO loadings under low and high magnifications: (a,b) 0.2 wt.%, (c,d) 0.4 wt.%, (e.f) 0.8 wt.%, and (g,h) 1.2 wt.%.
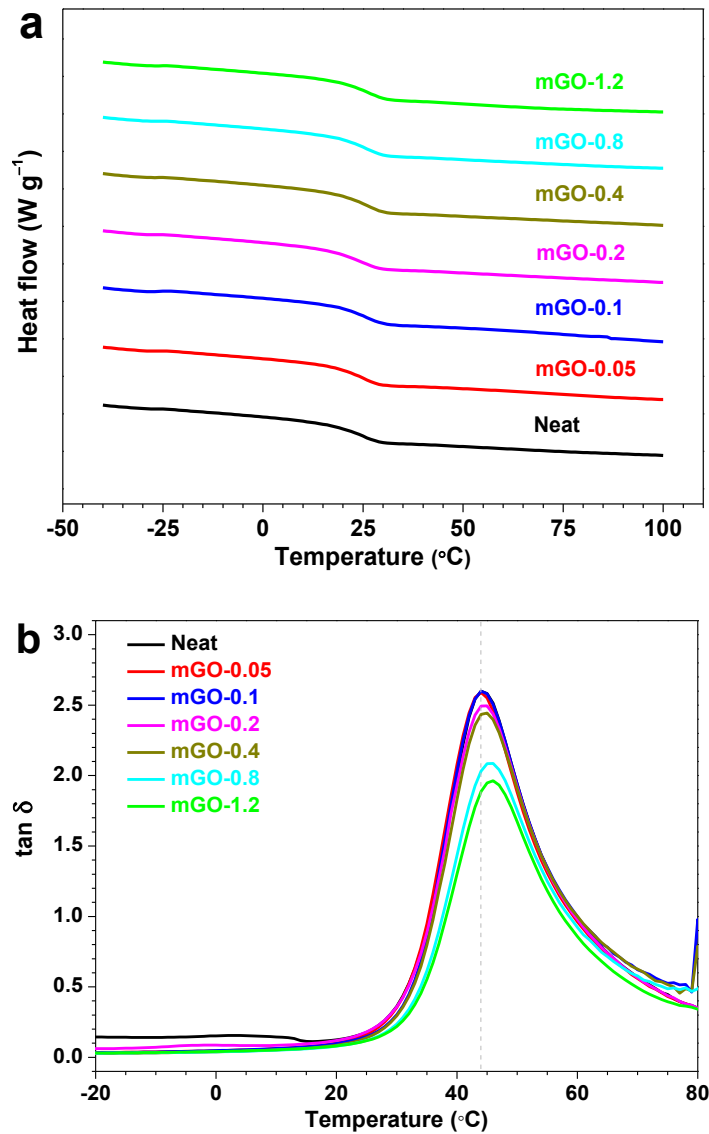
Figure A.8 Thermal mechanical testing of LNC films with different mGO loadings: (a) DSC curve and (b) DMA tan δ curve.

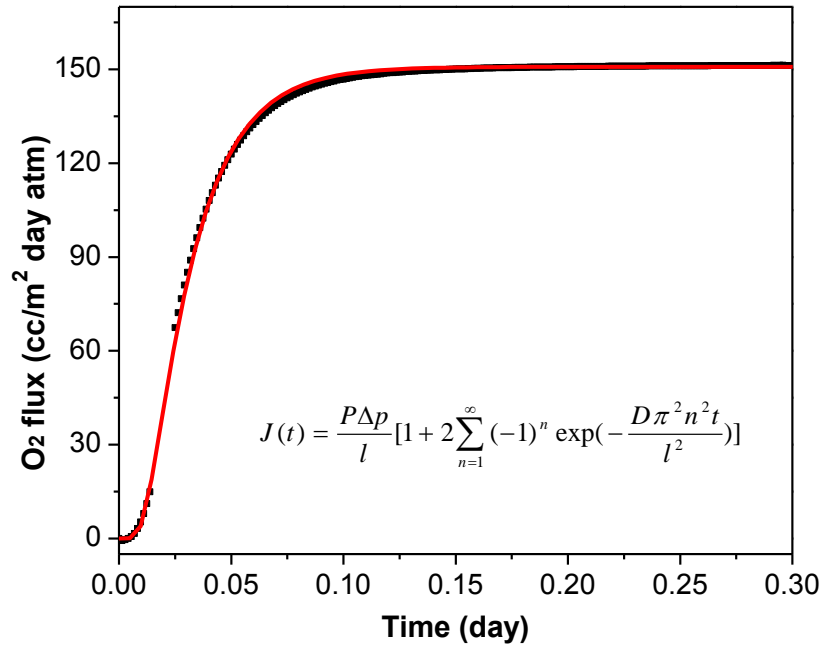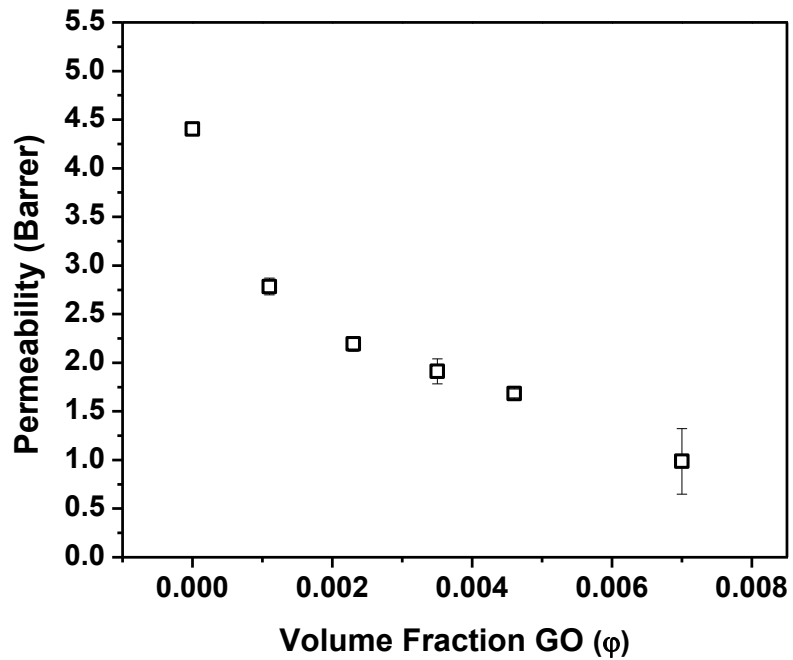Figure A.9 Representative plot of an experimental fit to Fick's second law of oxygen flux data.

$$J(t) = \frac{P\Delta p}{l}[1 + 2\sum_{n=1}^{\infty}(-1)^n \exp(-\frac{D\pi^2 n^2 t}{l^2})]$$

Figure A.10 O_2 permeability plot for LNC films with different GO loadings.

Table A.1 Latex nanocomposites formulations.

| Series | Styrene-acrylic latex (100 g) | | | BYK®-428 | GO | mGO | Solids |
	St	EHA	MAA	(wt.%)	(wt.%)	(wt.%)	(wt.%)
Neat (diluted)	59.5	39.5	1	–	–	–	25
GO-0.2–0.6	59.5	39.5	1	0.01	0.2–0.6	–	25
GO-0.8	59.5	39.5	1	0.02	0.8	–	17
GO-1.2	59.5	39.5	1	0.02	1.2	–	17
mGO-0.025–0.6	59.5	39.5	1	0.01	–	0.025–0.6	25
mGO-0.8	59.5	39.5	1	0.02	–	0.8	17
mGO-1.2	59.5	39.5	1	0.02	–	1.2	17

Table A.2 Calculated proportion of four C-containing components according to fitted

peaks of C1s XPS spectrum of graphene oxide (GO).

Peak (eV)	Assignment	Proportion
C=C (284.7)	sp^2 carbon	69.8%
C–O (286.5)	Hydroxyl, Epoxy	8.5%
C=O (287.1)	Carbonyl	20.3%
O=C–O (289.0)	Carboxyl, Ester	1.4%

Table A.3 Calculated proportion of four C-containing components according to fitted

peaks of C1s XPS spectrum of modified graphene oxide (mGO).

Peak (eV)	Assignment	Proportion
C=C (284.6)	sp^2 carbon	59.3%
C–O/C–Br (286.5)	Hydroxyl, Epoxy, Carbon–Bromine	9.2%
C=O (287.1)	Carbonyl	25.4%
O=C–O (288.7)	Carboxyl, Ester	6.1%

Table A.4 Calculated proportion of three O-containing components according to fitted peaks of O1s XPS spectrum of graphene oxide (GO).

Peak (eV)	Assignment	Proportion
C–O (533.7)	Hydroxyl, Epoxy	28.1%
C=O (532.6)	Carbonyl	61.4%
O=C–O (531.0)	Carboxyl, Ester	10.5%

Table A.5 Calculated proportion of three O-containing components according to fitted peaks of O1s XPS spectrum of modified graphene oxide (mGO).

Peak (eV)	Assignment	Proportion
C–O (533.2)	Hydroxyl, Epoxy	14.2%
C=O (532.4)	Carbonyl	71.4%
O=C–O (531.3)	Carboxyl, Ester	14.4%

Table A.6 Thermal properties of LNC films with different mGO loadings.

Sample	T_g (DSC) (°C)	T_g (E′) (°C)	T_g (tan δ) (°C)
Neat	24.7	31.8	43.9
mGO-0.05	25.0	31.8	43.9
mGO-0.1	25.4	31.8	44.1
mGO-0.2	24.8	31.8	44.4
mGO-0.4	25.9	32.6	44.9
mGO-0.8	26.1	33.7	45.4
mGO-1.2	26.6	34.1	45.9

Table A.7 Oxygen gas permeability of LNC films with different GO loadings.

Sample (wt.%)	Volume Fraction GO (φ)	Permeability (P) [Barrer]	Relative Permeability (P_c/P_n)
Neat-0	0.0000	4.40 ± 0.06	1.00
GO-0.2	0.0011	2.78 ± 0.09	0.63
GO-0.4	0.0023	2.19 ± 0.07	0.50
GO-0.6	0.0035	1.91 ± 0.13	0.43
GO-0.8	0.0046	1.68 ± 0.05	0.38
GO-1.2	0.0070	0.99 ± 0.34	0.22

APPENDIX B –Facile Functionalization of Graphene Oxide via Low Density Aerogel Precursor

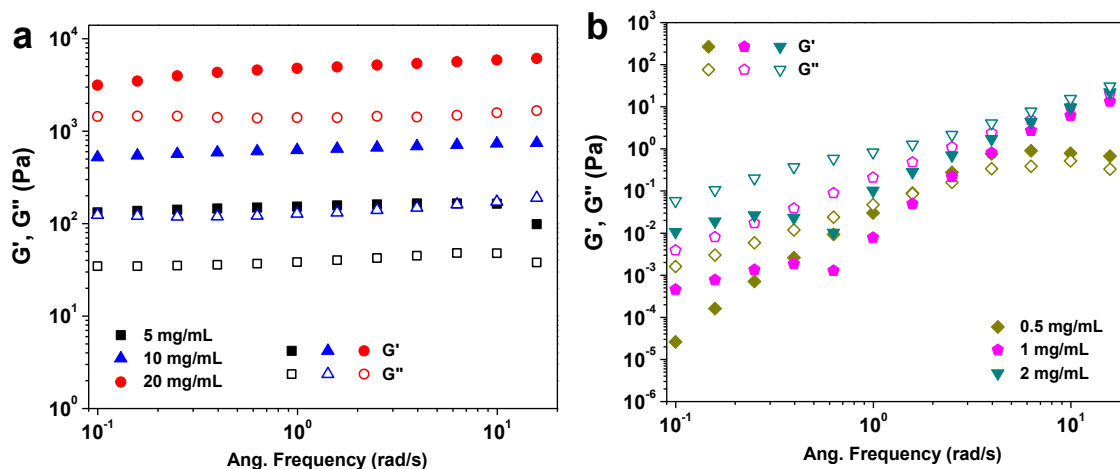and Fabrication of Polymer-*g*-GO Nanocomposite Corrosion Protection Coatings

Figure B.1 (a) Shear storage modulus (G', solid dots) and (b) shear loss modulus (G'',

open dots) of GO aqueous suspensions of varying concentrations (mg/mL).

Figure B.2 Digital images of GO aqueous suspensions of varying concentrations (from

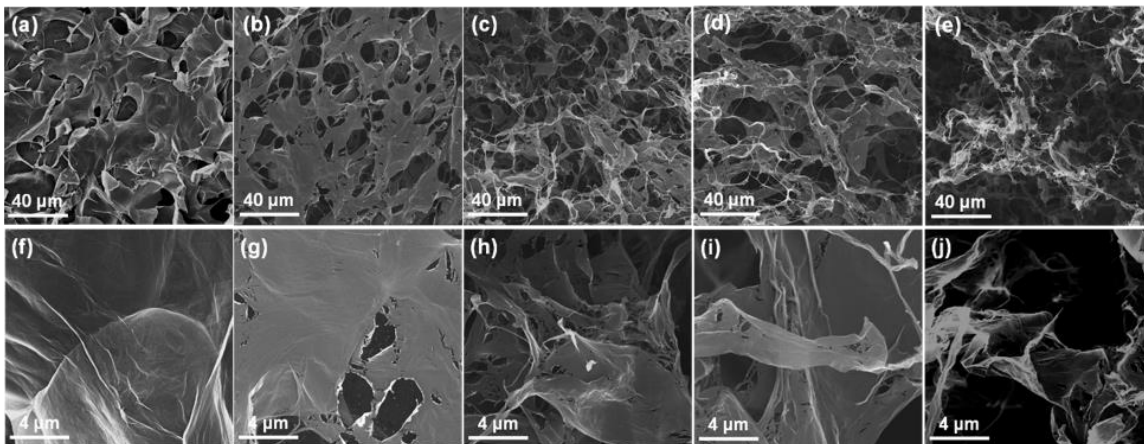left to right: 10, 5, 2.5, 1, and 0.3 mg/mL) and the resulting GO aerogels.

Figure B.3 SEM images of GO aerogels obtained from different concentrations of GO aqueous suspensions (from left to right: 10, 5, 2, 1, and 0.3 mg/mL).
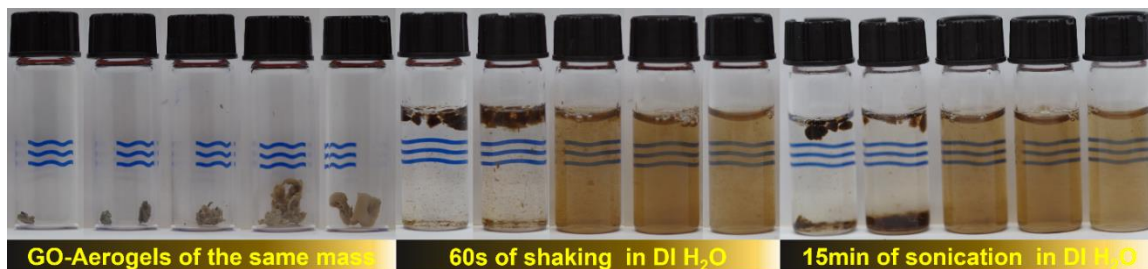

Figure B.4 Digital images of GO aerogels obtained from different concentrations of GO aqueous suspensions (from left to right: 10, 5, 2, 1, and 0.3 mg/mL) and their dispersibility in DI water.
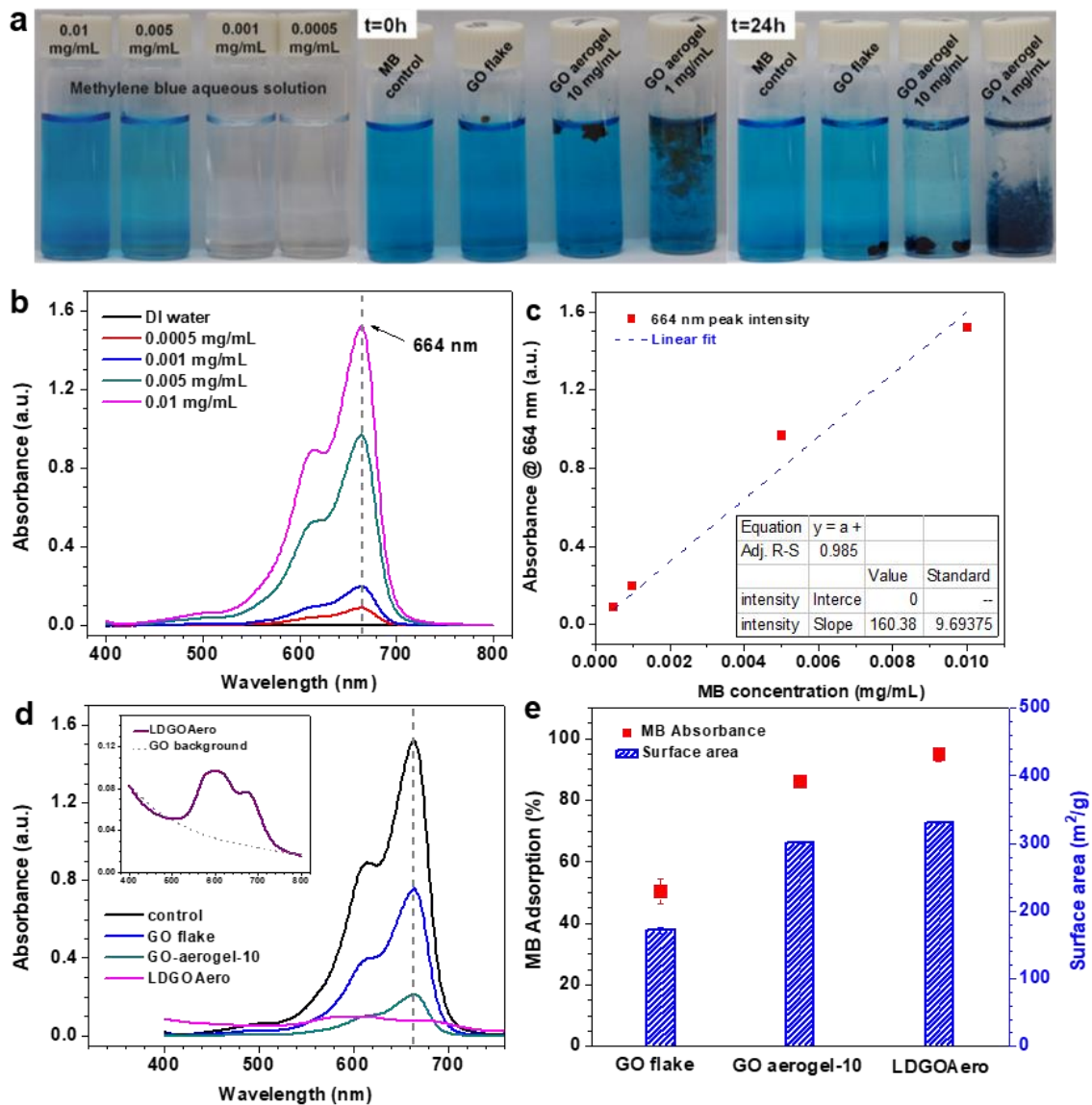
Figure B.5 (a) Digital images of methylene blue (MB) aqueous solution and surface
adsorption test at by GO flakes and GO aerogels obtained from 1 and 10 mg/mL GO
aqueous suspensions, respectively, (b, c) UV-vis spectra and linear fitting of MB
absorbance @ 664 nm, (d) UV-vis spectra of the supernant after 24h and (e) surface area
measured for GO flakes and GO aerogels obtained from 1 and 10 mg/mL GO aqueous
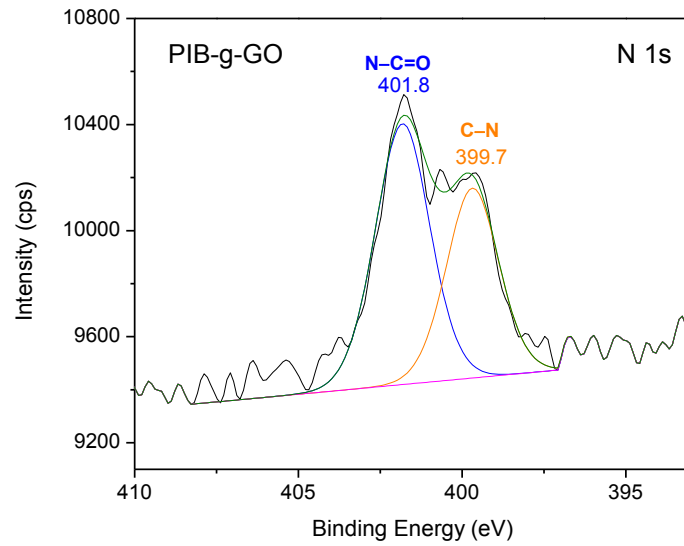suspensions, respectively.

Figure B.6 XPS spectra of N 1s high-resolution scans of PIB-*g*-GO.
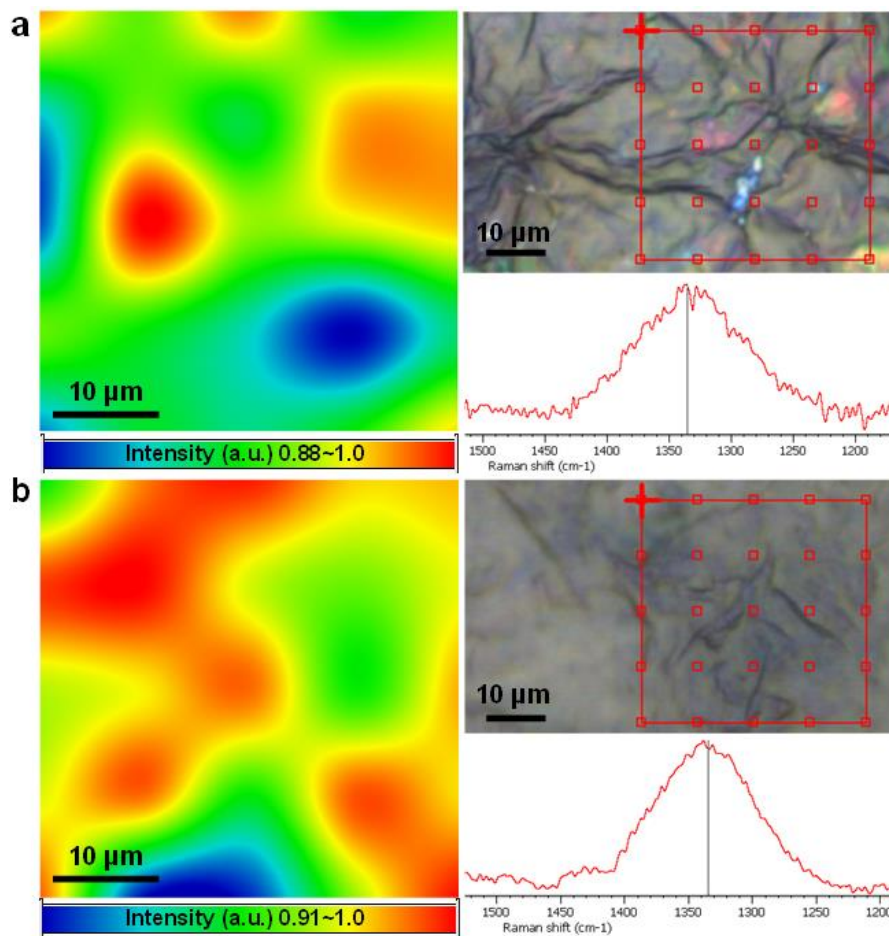

Figure B.7 Raman image mapping of D band on (a) GO and (b) PIB-*g*-GO film samples.
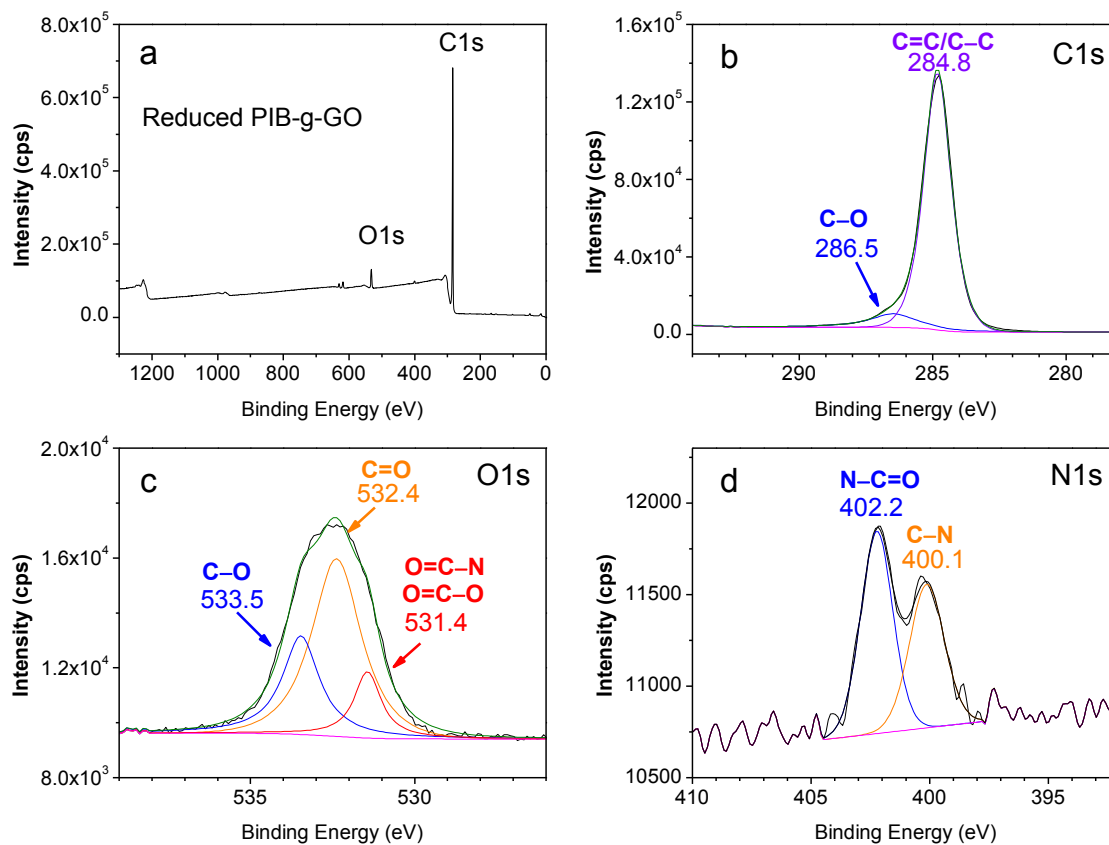
Figure B.8 XPS spectra of (a) the survey scan, (b) C 1s, (c) O 1s and (d) N 1s high-resolution scans of chemically reduced PIB-*g*-GO.

Figure B.9 AFM image and profile of (a,b) GO, (c,d) mGO (r = 3.85), (e,f) mGO (r = 9.63) and (g,h) PIB-*g*-GO deposited from dilute suspensions.
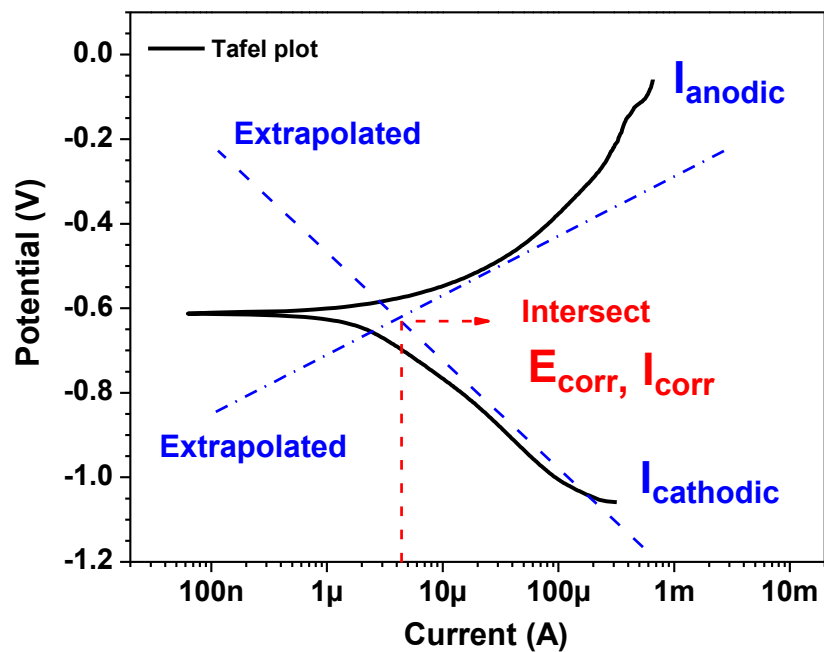
Figure B.10 Representative Tafel analysis to obtain corrosion current density and corrosion kinetic parameters by extrapolating the Tafel plot.
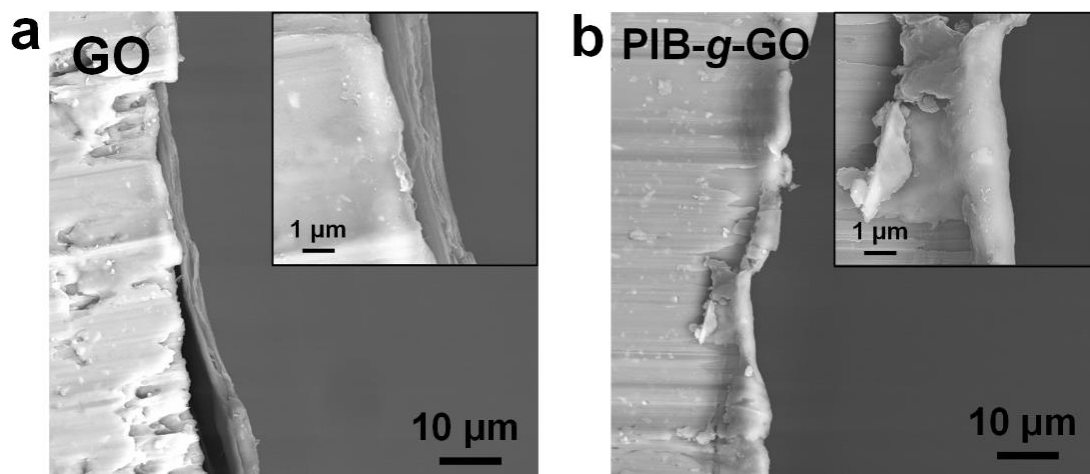
Figure B.11 Cross-sectional SEM images of (a) GO and (b) PIB-g-GO films coated on the substrates.
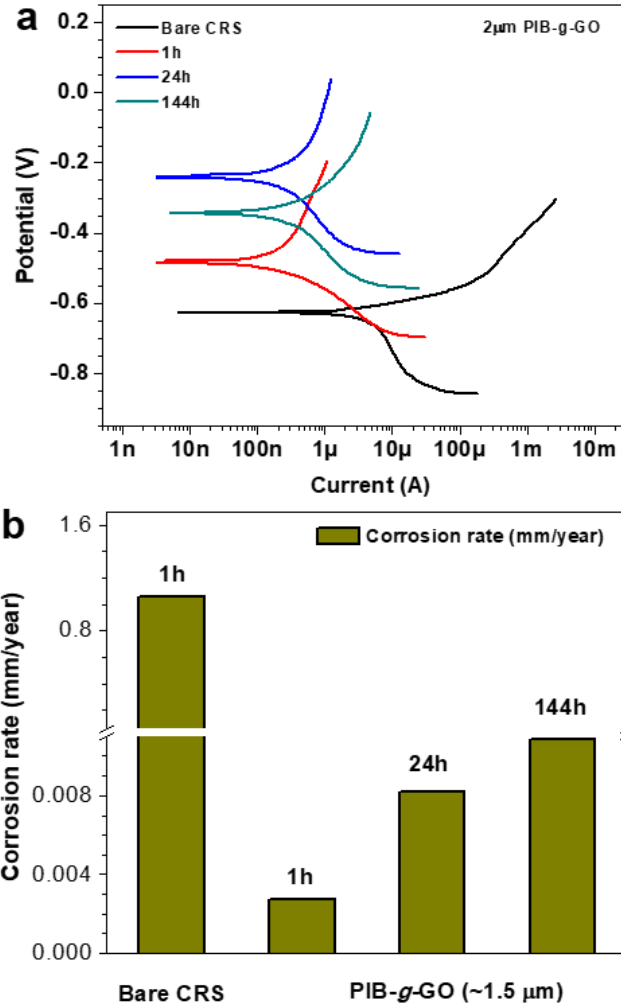
Figure B.12 (a) Tafel plots and (b) corrosion rate of PIB-*g*-GO (~1.5 µm) coating immersed in 3.5% NaCl solution for 144 h.

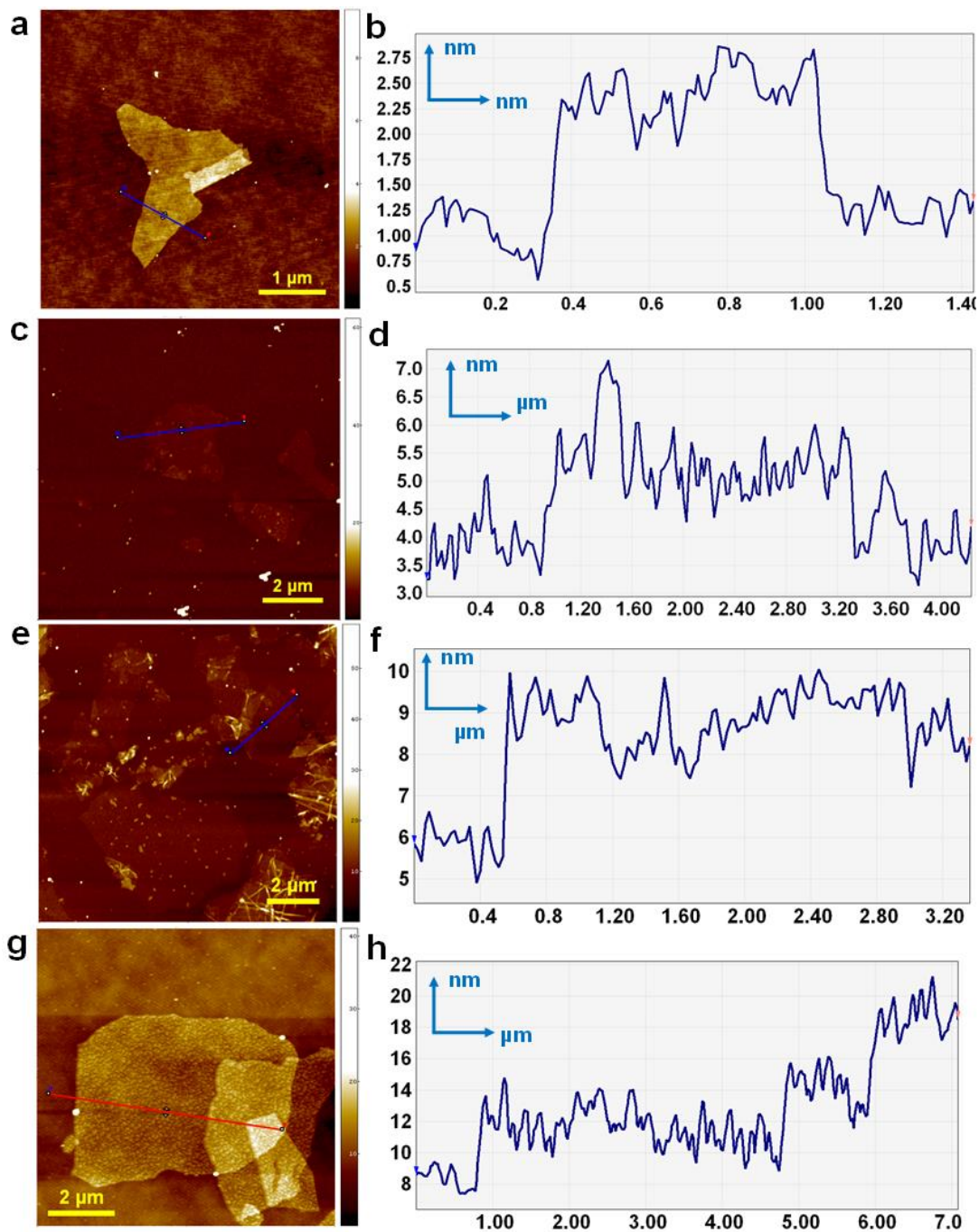Table B.1 Chemical composition and specifications (wt.%) of cold rolled steel (CRS).

CRS panel specifications: Cold Rolled Steel, Low Carbon, SAE 1008/1010					
Thickness	Finish	Roughness	ASTM	Temper	Hardness
0.5mm	smooth	< 20 micro-inch	A1008 D609-Type 3	¼ hard	B50-B65
Element	Manganese	Carbon	Phosphorus	Sulfur	Iron
Wt.%	< 0.60	< 0.15	< 0.030	< 0.035	> 99.185

Table B.2 Calculated proportion of four C-containing components according to fitted peaks of C1s XPS spectrum of the starting GO (LDGOAero).

Peak (eV)	Assignment	Proportion
C=C/C–C (284.8)	sp^2/sp^3 carbon	53.43%
C–O (286.8)	Hydroxyl, Epoxy	11.95%
C=O (287.2)	Carbonyl	24.38%
O=C–O (288.6)	Carboxyl	10.24%

Table B.3 Calculated proportion of four C-containing components according to fitted peaks of C1s XPS spectrum of hexanoyl chloride functionalized GO (mGO with r = 3.85).

Peak (eV)	Assignment	Proportion
C=C/C–C (285.0)	sp^2/sp^3 carbon	49.93%
C–O (286.8)	Hydroxyl, Epoxy	10.46%
C=O (287.3)	Carbonyl	28.78%
O=C–O (288.6)	Carboxyl, Ester	10.83%

Table B.4 Calculated proportion of four C-containing components according to fitted peaks of C1s XPS spectrum of hexanoyl chloride functionalized GO (mGO with r = 9.65)

Peak (eV)	Assignment	Proportion
C=C/C–C (284.9)	sp^2/sp^3 carbon	56.20%
C–O (286.8)	Hydroxyl, Epoxy	7.99%
C=O (287.3)	Carbonyl	25.03%
O=C–O (288.8)	Carboxyl, Ester	10.78%

Table B.5 Calculated proportion of four C-containing components according to fitted peaks of C1s XPS spectrum of PIB-*g*-GO.

Peak (eV)	Assignment	Proportion
C=C/C–C (284.5)	sp^2/sp3 carbon	87.85%
C–O (286.8)	Hydroxyl, Epoxy	12.15%

Table B.6 Calculated proportion of three O-containing components according to fitted peaks of O1s XPS spectrum of the starting GO (LDGOAero).

Peak (eV)	Assignment	Proportion
C–O (533.2)	Hydroxyl, Epoxy	33.88%
C=O (532.6)	Carbonyl	56.33%
O=C–O (531.5)	Carboxyl	9.79%

Table B.7 Calculated proportion of three O-containing components according to fitted peaks of O1s XPS spectrum of hexanoyl chloride functionalized GO (mGO with r = 3.85).

Peak (eV)	Assignment	Proportion
C–O (533.3)	Hydroxyl, Epoxy	23.14%
C=O (532.8)	Carbonyl	63.40%
O=C–O (532.0)	Carboxyl, Ester	13.46%

Table B.8 Calculated proportion of three O-containing components according to fitted peaks of O1s XPS spectrum of hexanoyl chloride functionalized GO (mGO with r = 9.65).

Peak (eV)	Assignment	Proportion
C–O (533.6)	Hydroxyl, Epoxy	14.72%
C=O (532.9)	Carbonyl	62.21%
O=C–O (532.1)	Carboxyl, Ester	23.07%

Table B.9 Calculated proportion of three O-containing components according to fitted peaks of O1s XPS spectrum of PIB-*g*-GO.

Peak (eV)	Assignment	Proportion
C–O (533.7)	Hydroxyl, Epoxy	11.73%
C=O (532.7)	Carbonyl	58.17%
O=C–O/O=C–N (531.4)	Carboxyl, Amide	30.10%

Table B.10 Calculated proportion of three O-containing components according to fitted peaks of N1s XPS spectrum of PIB-*g*-GO.

Peak (eV)	Assignment	Proportion
N–C=O (401.8)	Amide	58.87%
C–N (399.7)	Amine	41.13%

Table B.11 Calculated proportion of four C-containing components according to fitted peaks of C1s XPS spectrum of reduced PIB-*g*-GO.

Peak (eV)	Assignment	Proportion
C=C/C–C (284.8)	sp^2/sp^3 carbon	89.08%
C–O (286.5)	Hydroxyl, Epoxy	10.92%

Table B.12 Calculated proportion of three O-containing components according to fitted peaks of O1s XPS spectrum of reduced PIB-*g*-GO.

Peak (eV)	Assignment	Proportion
C–O (533.5)	Hydroxyl, Epoxy	14.78%
C=O (532.4)	Carbonyl	55.39%
O=C–O/O=C–N (531.4)	Carboxyl, Amide	29.83%

Table B.13 Calculated proportion of three O-containing components according to fitted peaks of N1s XPS spectrum of reduced PIB-*g*-GO.

Peak (eV)	Assignment	Proportion
N–C=O (402.2)	Amide	56.44%
C–N (400.1)	Amine	43.56%

Table B.14 Carbon to oxygen ratio (C/O) calculated from XPS spectra of survey scans

for GO (LDGOAero), hexanoyl chloride functionalized GO (mGO, r = 3.85 and 9.65),

PIB-*g*-GO and reduced PIB-*g*-GO.

Sample	C (at.%)	O (at.%)	C/O atomic ratio
GO (LDGOAero)	61.48	38.52	1.60
mGO (r = 3.85)	64.59	35.41	1.82
mGO (r = 9.65)	68.19	31.81	2.14
PIB-*g*-GO	94.02	5.98	15.7
r-PIB-*g*-GO	97.53	2.47	39.5

Table B.15 Solvent polarity and properties (Reference 69)

Solvent	Formula	Boiling point (ºC)	Relativity polarity
Water	H_2O	100.0	1.000
Methanol	CH_4O	64.6	0.762
Ethanol	C_2H_6O	78.5	0.654
Dimethylsulfoxide (DMSO)	C_2H_6OS	189	0.444
Dimethylformamide (DMF)	C_3H_7NO	153	0.386
Acetone	C_3H_6O	56.2	0.355
Chloroform	$CHCl_3$	61.2	0.259
Tetrahydrofuran (THF)	C_4H_8O	66	0.207
Toluene	C_7H_8	110.6	0.099
n-Hexane	C_6H_{14}	69	0.009
Cyclohexane	C_6H_{12}	80.7	0.006

Note: values cited from https://sites.google.com/site/miller00828/in/solvent-polarity-table;